SHRINKAGE AND ADHESIVE STRESSES IN FIBRE-REINFORCED COMPOSITES

by

N. K. ASAMOAH, M.Sc. (Eng.), D.I.C.

Thesis submitted for the Degree of Ph.D. in the Faculty of Engineering of the University of London.

MECHANICAL ENGINEERING DEPARTMENT,
IMPERIAL COLLEGE

November 1969

To

Charles Edwin Asante

A B S T R A C T

An explanation is presented of the shrinkage process in unidirectional fibre composites which leads to thermal self-straining and successful predictions on the nature of the stresses are made.

A finite element method is used to investigate the shrinkage and ahesive stresses in uniaxial fibre composites for various fibre spacings. It is shown that the magnitude of the shrinkage stresses depends on the Young's Modulus of the matrix and the thermal coefficients of expansion of both matrix and fibre. The transverse stresses are compressive for most fibre spacings increasing with decreasing fibre spacing, except for very close spacings when tensile stresses develop from within the central region of the matrix.

Plane and axisymmetric finite element idealisations simulating the conditions in the axial direction of fibres, and as used by other investigators to study the response of composites to external forces, were found to be inadequate and unsuccessful for the simulation of thermal shrinkage in real composites.

A photothermoelastic technique has been developed to study the restrained shrinkage in the composites for both continuous and discontinuous fibres using a hot-setting epoxy resin as matrix and aluminium rods as fibres. The results for the caseof the continuous fibres agree well with the numerical results. A triaxial state of compression is found to exist in the discontinuity and initial high shear stresses

at the tip of the fibre ends were sufficient to initiate cracks when the fibre spacing was close.

The effect of the initial stresses in composites is to increase the composite strength in compression and in tension for continuous and discontinuous fibre composites respectively. It should be possible to control the manufacture of composites for high performance applications by optimising the spacing of the fibres so as to avoid initial tensile stresses which would precipitate cracks.

ACKNOWLEDGEMENTS

The course of investigation reported herein was initially suggested to me by Dr. W. G. Wood. I wish to express my sincere thanks for his keen supervision, encouragement and discussion during the various phases of the research.

My thanks also go to the technical staff of the Mechanical Engineering Department and other departments of the College for their help in the acquisition and preparation of materials. In particular, I express my appreciation to Mr. A. Dowden (Students' Workshop) for his interest and advice and to Mr. S. P. May (ex-student) for his devoted assistance in the preparation of the photoelastic models during the summer of 1968.

It has been a great asset to work among friendly colleagues of various backgrounds: J. P. Bindon (South Africa), P. E. J. Fish (Rhodesia), D. J. Hayes (U.K.), M. O. Khan (Pakistan) and N. C. Remedios (Kenya).

Lastly, I feel much indebted to the University of Science and Technology, Kumasi, Ghana, who sponsored me in the United Kingdom.

N.K.A.

C O N T E N T S

		Page
	NOTATION	9
	INTRODUCTION	11
1.	Fibre Reinforcement	12
2.	Materials For Composites	14
3.	Production Methods for Composites	15
4.	Literature Survey	16
5.	Shrinkage Stress Studies	20
	CHAPTER 1: MECHANICS OF SHRINKAGE	22
1.1	Introduction	22
1.2	The Interference Model	23
1.3	Effect of Constraint in Axial Direction	26
	CHAPTER 2: THE FINITE ELEMENT METHOD	27
2.1	Introduction	27
2.2	Displacement Functions	28
2.3	Derivation of the Element Characteristics	29
2.4	General Remarks	32
2.5	Computational Procedure	32
2.6	Application to Present Work	33
2.7	Boundary Conditions	35
2.8	Accuracy	36
	CHAPTER 3: FINITE ELEMENT ANALYSIS OF CONTINUOUS FIBRES	39
3.1	Introduction	39
3.2	Composite Materials	39
3.3	Composite Systems Investigated	41
3.4	Computed Results	45

Page

CHAPTER 4: SHRINKAGE STRESSES AROUND A DISCONTINUOUS FIBRE 52

4.1 Introduction 52

4.2 Discontinuous Fibre Composite Models 52

4.3 Model for Thermal Shrinkage Analysis 54

4.4 Results 55

4.5 Relationship of Results to Real Composite 57

CHAPTER 5: PHOTO-VISCOELASTIC BEHAVIOUR OF BIREFRINGENT MATERIALS 59

5.1 The Basic Principles of Photoelasticity 59

5.2 Photoelastic Methods 61

5.3 Photothermoelasticity 62

5.4 Viscoelastic Behaviour of High Polymers 63

5.5 Time-Temperature Superposition Principle 68

5.6 Temperature-Stress-Optical Relationship 68

CHAPTER 6: EXPERIMENTAL WORK 71

6.1 The Photothermoelastic Technique 71

6.2 Shrinkage and Adhesive Studies 73

6.3 Calibration Tests 84

6.4 Creep Tests 88

CHAPTER 7: ANALYSIS OF EXPERIMENTAL DATA 89

7.1 Introduction 89

7.2 Planes of Symmetry 90

7.3 Extension of Lame-Maxwell Equations in Three-Dimensions 91

7.4 Shear Difference Method 92

		Page
7.5	Analysis of Photoelastic Data	94
7.6	Accuracy	101
7.7	Results	101
7.8	Comparison with Plane Model	103
DISCUSSION		104
1.	Experimental Techniques	104
2.	Results	109
3.	Effect of Externally Applied Load	115
4.	General	117
CONCLUSIONS		120
REFERENCES		123
FIGURES		130
APPENDIX I		192
APPENDIX II		194
APPENDIX III		199
FINITE ELEMENT PROGRAM		201

COMMONLY USED NOTATION*

m	subscript for matrix; packing factor
f	subscript for fibre
α	coefficient of thermal expansion
v	Poisson's ratio
E	Young's Modulus
V	volume fraction
o	direct stress
τ	shear stress
ϵ, e	strain

*Other symbols are defined in text.

INTRODUCTION

The quest for new structural materials to meet the demands of the present and developing trend of technology has stimulated a lot of interest and research in composite materials over the past decade. Although the use of composite materials is an old art (e.g. straw in bricks, reinforced concrete), the need to understand the mechanics of their reinforcing action is comparatively a very new but growing pre-occupation of structural and materials scientists and engineers. Progress and interest in this field of activity have been spurred on by the advent of manufactured fibres having unusually high levels of strength and stiffness.

A great deal of attention has been given to the problem of the stress distribution of fibre-reinforced composite materials under various loading conditions and fibre geometry. However, most practical composite materials are formed at elevated temperatures; in addition, during use, they may be subjected to temperature variations such as in aerospace applications. The use of reinforced concrete in structures exposed to thermal gradients such as nuclear reactor shields, high temperature ducts, etc. are other examples. The differences in thermal expansions of the component materials may give rise to internal stresses whose magnitudes can be extremely large and often detrimental.

Consider, for example, a composite in which boron fibres are formed into a nickel alloy matrix at 500°C. If we assume for simplicity that the thermal self-straining is wholly elastic when the composite is cooled to atmospheric temperature we find that stresses of the order of the strength of the strongest nickel alloys are produced. Little attention has been given to this problem in the past even though its presence has long been recognised; only the simplest picture of thermal stress distribution has been available. It is clear, however, that an accurate picture of thermal self straining is necessary before reasons for fibre, matrix or interface failure can be understood more fully.

The purpose of the present work is to explain the mechanics of thermal self-straining in composite materials employing continuous unidirectional fibres and to provide finite element and photoelastic analyses for a wide range of fibre spacing. Since many of the high strength fibres are likely to be available only as short discontinuous filaments, or whiskers, the thermal self-straining effects in the fibre discontinuities havealso been investigated.

1. FIBRE REINFORCEMENT

The mechanics of fibre reinforcement is well understood and has been treated at length in various experimental and analytical ways elsewhere (1) (2) (3) (4). An enormous literature covers both micro and macro-analytical methods.

The general view of fibre-reinforcement is that an otherwise brittle but very strong phase is embedded in a weaker and ductile phase or matrix which acts as a load transmitter between the fibres. In order for the matrix to transfer load effectively, it must have a sufficiently high adhesive and interfacial shear strength either through a chemical or mechanical adhesion or a combination of the two. In addition the matrix fulfils the function of (i) bonding the fibres together and protecting their surfaces from damage which could lead to loss of strength and (ii) separating the fibres to prevent crack propagation across the composite entirely in the brittle phase. The strength of the composite depends upon the environment in which it is to be used and factors like temperature, humidity, the presence of corrosive elements are of great importance.

Both the matrix cohesive shear strength and the interfacial shear strength must be adequate to the designed service conditions of the composite. An elevated temperature application will generally reduce the interfacial shear strength to a greater extent or at a faster rate than the matrix cohesive shear strength. It is therefore necessary to investigate the effect of temperature on the matrix and its interface to obtain fundamental information which would lead to improved load transfer characteristics thereby resulting in efficient and optimum use of composite materials.

2. MATERIALS FOR COMPOSITES

High strength fibres are available in one of the following forms:

(i) Glass fibres,

(ii) Ceramic fibres,

(iii) Polymeric fibres

(iv) Metal wires, and

(v) Whiskers

Whiskers possess the highest strengths approaching the theoretical strength of the crystal (5). These include graphite whiskers, sapphire whiskers (Al_2O_3) and the carbides and borides of most hard metals. An account of these materials may be found in references (6) (7) (8); Coleman (9) has reviewed the methods of their preparation. Due to the present form of their preparation, they are available mainly in the form of short fibres; their cost of production is very high. Metal wires which have been used for reinforcement include stainless steel wires, tungsten wires and platinum wires usually manufactured by conventional drawing or extrusion methods. Glass fibres and polymeric fibres are cheap and easy to produce in the form of continuous filaments. All these materials, especially the oxides, carbides and silicates, maintain their high strength properties at elevated temperatures and it is in these high temperature fields of application that their potential lies. The matrix may either be a metal, e.g. copper, aluminium, silver, or resin although in a few instances a ceramic matrix may be employed.

3. PRODUCTION METHODS FOR COMPOSITES

The fabrication of fibres into a matrix presents many problems. Prominent among these are the problems of surface wetting to achieve a consistent and effective bond and the tendency of fibres to alloy with the matrix in the case of metallic fibres - the oxide fibres being by comparison chemically inert. In addition, the processing temperature must not be so high as to lead to structural changes in the fibre and an associated reduction in strength. Petrasek and Weeton (10 observed these effects in their study of copper alloy composites reinforced with tungsten wire.

Different methods are available for the preparation of composite materials. These include powder-metallurgical methods, liquid infiltration methods, hot-pressing and hot-rolling processes. Details of these operations may be found in references (5) and (6). In all these operations, control of the operating pressure and temperature is necessary to ensure fibre/matrix coherence and integrity and maximum composite strength. For example, using stainless steel wires in an aluminium matrix, Cratchley (11) carried out soaking experiments to determine an appropriate pressing temperature. Again, Cratchley and Baker (12) have studied the effect of temperature and pressure on silica/aluminium composites by hot pressing fibres which had been previously coated with the matrix at different pressures and temperatures in a mould. At all pressing temperatures the curve of pressure versus fraction of theoretical composite strength achieved, showed a maximum, the peak value of which was dependent upon temperature.

4. LITERATURE SURVEY

The anisotropy of the single crystals of most materials and the differences between the bulk physical properties of the components of compound solids readily cause internal self-compensated stress systems to develop round such centres as crystals or components of the compound structure. The problem of thermal shock resulting in cracks or failure is well known to the ceramicist; quench hardening of steels is also an old craft. All these processes involve the use of materials which are both structurally and crystallographically inhomogeneous and anisotropic.

(i) Analytical Work

The first published serious analytical consideration of the problem of thermal self-straining in compound materials appears to be by László in 1942 (13). He called the resulting stresses "tessellated stresses". Using different "tessellated" units in the form of a lamellar slab, compound cylindrical and spheroidal units, and elasticity theory, he calculated the stresses in these various units resulting from (i) a uniform temperature drop, (ii) a phase transformation at constant temperature resulting in a volumetric change Δ and (iii) entrainment of spherical gas cavities. He then attempted the explanation of the hardening of steels based on the results of the calculations considering the hardened material as cylinders of α-martensite needles embedded in a matrix of austenite. The effect of "tessellated stresses" on other phenomenon related

to steel and cast irons such as yielding, graphitation, fatigue, magnetisation etc. were also examined.

Florence and Goodier (14) first recognised that localised thermal stresses appear when an otherwise uniform flow of heat is disturbed by cavities or inclusions with different thermal and elastic properties from those of the surrounding matrix. Dundurs and Zienkiewicz (15) investigated the stresses in the vicinity of a long cylindrical elastic rod embedded in an elastic material subjected to a uniform temperature gradient in a direction transverse to the axis of the bar. Their solution is based on an Airy stress function which was obtained by the superposition of a "zero-stress" solution on a second solution introduced in order to cancel the multivalued and discontinuous displacements arising from the first solution. The same problem has also been solved in a direct way by Tauchert (16) using a displacement function derived by Sternberg and McDowell (17).

The first serious consideration of thermal shrinkage stress[5] in fibre reinforced composites of any consequence was by Outwater (12). In deriving a mathematical relationship for the tensile modulus of elasticity of unidirectionally reinforced plastics, he took into account shrinkage stresses as providing the necessary frictional restraint at the interface to maintain the composite strength after delamination.

(ii) Experimental Work

Early experimental work on thermal shrinkage stresses in composites involved the use of strain gauges to measure the

pressure on the surface of a spheroidal glass bulb immersed in a curing resin (19). As the curing and cooling proceeded the strain gauge readings were recorded and from a previous calibration of the gauge for temperature the pressure due purely to the resin shrinkage effect, was evaluated. Haslett and McGarry (20) and Daniel (21) all used photoelastic methods to study the shrinkage stress in small diameter E-glass fibres surrounded by a resin matrix. Using multiple fibres they found that the axial stresses (along the length of the fibres) diminish rapidly as the spacing between fibres decreases. Also using various assumptions and simplifications Haslett and McGarry attempted an analytical solution for the shrinkage stresses. They found that the sense of the resin stress tensile or compressive, depended upon the spacing of the fibres, but this conclusion depended on the assumptions made.

Daniel and Durelli (22) have studied the photoelastic fringes resulting from the shrinkage of resin around both single and multiple disc inclusions in a plate. They found that the number of fringes decreased appreciably (up to 60%) with time after cooling to room temperature due to stress relaxation in the viscoelastic resin. In all these experiments it was found that the level of the fringes and hence of stress increased with increasing curing temperature; the stress distribution was independent of the curing cycle and size of the inclusion but depended on the geometrical arrangement of the inclusions. In another work (23), Daniel and Durelli attempted both to explain and simulate the shrinkage process by inserting

slightly oversized glass discs into holes in a sheet of urethane rubber. The stress distribution resulting from such an interference model was obtained.

More recently, Marloff and Daniel (24) have used three-dimensional stress-freezing techniques to determine the stress distributions in the matrix of unidirectionally fibre reinforced composite model subjected to both shrinkage and normal transverse loading. Koufopoulos and Theocaris (25) have also used photoelastic methods to study the effect of the elastic moduli of both matrix and inclusion on the stress distribution. By the use of unplasticized epoxy as inclusion and plasticized epoxy as matrix it was found that for a single disc in an infinte matrix, the magnitude of the stresses at the interface during the period of cooling depended only on (i) the constant elastic modulus of the inclusion and (ii) the instantaneous value of the matrix elastic modulus; it was independent of the amount of shrinkage of the matrix. However, for a square array of closely packed discs the stress distribution was found to depend on both the elastic moduli and the amount of shrinkage.

In all the above experimental studies temperature cycles were involved and consequently the elastic properties of the viscoelastic birefringent material did not remain constant. The methods of analysis of experimentally observed fringe patterns associated with such transient and steady state thermal stress fields is termed PHOTOTHERMOELASTICITY. In studies relating to composite materials, the fringe patterns

result from the restraint to shrinkage offered by the inclusions. It is imperative in such work to investigate the variations of the physical properties such as the modulus of elasticity, E, the coefficient of thermal expansion α and the material fringe value f over the appropriate temperature range.

(iii) Numerical Methods

Up to the present time all numerical work on fibre-reinforc materials has been concentrated on the elastic and elastic/plastic response of composites to externally imposed forces. The applicability of numerical methods to stress analysis of this kind depends largely on the fact that complex solid composite systems can be idealised e.g. to conform to either plane stress (or plane strain) or axisymmetric models. This is a major simplification but the results are useful towards the understanding and interpretation of composite behaviour and lead to better design and production techniques.

Numerical methods include (i) point-matching techniques (26 (85), (ii) finite difference methods (28) and (iii) finite element methods (29) (30) (4). In their various forms these methods have been successfully applied to the study of stresses in fibre-reinforced composites.

5. SHRINKAGE STRESS STUDIES

In the present work, the finite element method is used to study the shrinkage and adhesive stresses in various composite systems. The stresses in the transverse plane of

hexagonally arranged unidirectional fibre composites are investigated. The validity of simulating thermal shrinkage around fibre discontinuities using plane and axisymmetric models is also examined. A photothermoelastic method has been developed and is used to analyse both continuous and discontinuous fibre composites. In the first chapter, a more comprehensive and realistic view of the shrinkage mechanism leading to a prediction of the nature of the shrinkage stresses to be expected, is expounded. This explanation of the shrinkage mechanism should supercede the interference model view presented by Durelli and Daniel (23).

Chapters 2-4 deal with the finite element analyses starting with the presentation of the basic theory behind the method in Chapter 2. In Chapter 5-7 the experimental techniques and results are presented. The photo-viscoelastic properties of birefringent materials are reviewed in Chapter 5 and it is hoped that this will lead to a better understanding and appreciation of the various steps involved in the photothermoelastic technique which follows in Chapter 6.

Finally in the last section, a discussion of the experimental technique both on its own merits and in the light of related work by other investigators, is conducted. The relevance of the findings both experimental and numerical to prectical composites is also discussed.

A paper based on part of the work reported herein has been accepted for publication in the Journal of Strain Analysis.

CHAPTER 1

MECHANICS OF SHRINKAGE

1.1 INTRODUCTION

The shrinkage stresses for a single plane disc or continuous fibre embedded in a matrix, assuming elastic considerations, can be easily derived using the well-known Lamé type equations. Assuming perfect bonding, the radial and tangential stresses developed at the interface of a single plane disc* are given by:

$$\sigma_{r,\theta} = \frac{\Delta T(\alpha_m - \alpha_f)E_m}{(1+\nu_m)+(1-\nu_f)E_f/E_m} \qquad (1.1)$$

where α is the linear thermal expansion coefficient, ν the Poisson's ratio, E Young's modulus and ΔT the temperature change; the subscripts m and f refer to matrix and fibre respectively.

A much more complex state of stress arises in multiple fibre composites and the spacing of the fibres is important in determining the nature of the stresses. Fibre reinforced materials tend to an arrangement in which any fibre is surrounded by six other fibres equally spaced about it - namely a hexagonal arrangement, as in figure 1.1. In addition, the coefficient of thermal expansion of the matrix material is generally larger than that of the fibre. Haslett and McGarry (20) have presented

---

*For the case of a continuous fibre at points removed from its ends, plane strain conditions may be assumed. Equation (i) still holds for the stresses but the constants have to be modified thus:

$$\alpha = \alpha(1+\nu)$$
$$E = E/1-\nu^2$$
$$\nu = \frac{\nu}{1-\nu}$$

a simple extension of the single fibre analysis to widely spaced multiple fibres and this predicts compressive radial stresses at the interface when the composite is cooled. However, Outwater (18) has pointed out that when the fibres are packed tightly so that they lie in continuous line contact with each other, the tricorn of matrix material enclosed by any three fibres, figure 1.2, will tend to shrink away from the fibres on cooling and produce tensile stresses at the interface.

It is evident that the possibility of debonding, and beyond this, whether any surface traction between fibre and matrix will be available after debonding, is intimately connected with the sign and magnitude of the shrinkage stresses at the interface. Experimental studies by Broutman and McGarry (31) support this. They found that the bond strength of fibre reinforced plastics tested in compression depended upon the temperature at which the composite had been cured.

Daniel and Durelli (23) attempted to simulate the shrinkage problem by inserting oversize glass discs into a hexagonal array of holes in a sheet of urethane rubber. They subsequently analysed the stress system produced by the interference photoelastically. The two stress systems, namely the one resulting from thermal shrinkage and that produced by the interference, are not however, strictly analogous because the compatibility conditions of the true shrinkage system are violated by the interference model. This difference is discussed in the next section of this chapter.

1.2 THE INTERFERENCE MODEL

Consider a solid block of material with parallel holes in

a hexagonal array, figure 1. If the block is cooled a contraction will take place such that holes of size D become size d and this will be irrespective of the spacing of the holes. Let us examine the effect of inserting rods of diameter d, ($d_1 > d$) in the holes for various spacings.

a) Large Spacing

If the holes are spaced well apart, the effect is largely one of each rod being surrounded by a tube of matrix, independently of all the others. The effect of the tricorn in figure 2c will be very slight and there will be little shear along the interface in this case because each unit is almost purely axi-symmetric. Thus Haslett and McGarry's (20) model of axi-symmetric unit suffices here and purely radial compressive stresses appear at the interface.

b) Small spacing

All practical fibre-reinforced materials employ closely spaced fibres and to obtain a clear picture of the mechanics of interaction, we shall discuss first the limiting case where the fibres almost touch.

(i) Case of fibres almost touching

Here, the insertion of the rods would cause unequal stretching of each tricorn unit, figure 2a, the material at the corners of the tricorn being stretched most and gaps would appear between the fibres and the matrix. This cannot occur in the real shrinkage system because interfacial adhesion is presumed fully established before cooling takes place and this is maintained throughout the shrinkage process. The adhesion thus provides radial restraint on the matrix as long as the

bond remains intact. In addition, adhesion implies a compatibility condition in the circumferential direction around each fibre and shear stresses are established to control the unequal stretching of the tricorn which augment the tensions at the points of the tricorns, figure 2b. The Daniel-Durelli model is therefore inadequate for representing both radial and circumferential stresses due to shrinkage.

(ii) Case of fibres spacing slightly greater than (i)

Consider now the case where the holes are close enough to influence one another as the rods are inserted but are spaced a little further apart than before, figure 2c. Figure 2d shows a simplified stress system in the matrix element which may be useful in the following discussion.

The forces T will increase as the fibre spacing is increased and as a larger area of matrix material becomes involved and there will be a condition when T will be large enough relative to the inside tricorn stress σ_0, to establish contact all along the rod-to-matrix interface. A slightly smaller spacing than this would, in the interference model produce a gap at the points C which face the spaces between adjacent fibres. Consequently, the radial stress distribution in the real thermal shrinkage system might be expected to change from compression to tension in order to maintain compatibility as shown along the top edge of the matrix element in figure 2d. Wider spacings will lead to a decreasing effect from the tricorn, and when the fibres are well spaced apart, the single element axisymmetric model previously discussed becomes valid.

Daniel and Durelli(23) tested interference models with different hole spacings and did not report any gaps between the matrix and discs. We may conclude that the critical spacing below which the interface stresses becomes in part tensile, is less than the smallest spacing which they studied. Packing densities which give spacings of this order are common in practice and even in composites where the fibre volume fraction is smaller than this irregular spacing due to the method of manufacture may result in groups of fibres in very close proximity.

1.3 EFFECT OF CONSTRAINT IN AXIAL DIRECTION

The effects of shrinkage in the axial direction on the transverse stress distribution must also be examined. In the actual shrinkage system since $\alpha_m > \alpha_f$ there will be an axial tension in the matrix and an axial compression in the fibres. Thus we must examine here the effect of an axial pull on our original block with holes. In this case there will be a lateral contraction so that all the holes will shrink in size; in addition, all the fibres will expand laterally. The effects of both of these will be to increase the radial compression at the interface.

The predictions on the stress distribution within the matrix made here, have been tested using both experimental and numerical methods, for most real fibre reinforced composites. The methods employed and the results obtained from them will be the main subject of the ensuing chapters.

CHAPTER 2

THE FINITE ELEMENT METHOD

2.1 INTRODUCTION

The development of the finite element method of structural and continuum analysis was originally pioneered in the aircraft industry. It stemmed from the need to provide a method that would give sufficiently accurate structural data to be adequate for subsequent dynamic and aeroelastic analyses of complex aircraft structures. The experimental stress analyses of complex models is both expensive and time consuming; added to this, obsolescence and changes in design are not uncommon in the aircraft industry. These considerations, together with the advent and continuing development of digital computers, led engineers to develop analytical methods for the solution of complex structures.

Essentially, in formulating the finite element method, standard structural analysis procedures are generalised; the stresses and displacements in two- and three-dimensional structures are also calculated by the same procedures.

Any structural system may be considered as consisting of separate components interconnected at a number of nodal points - e.g. for a jointed frame structure, the joints may be conveniently taken as nodes. However, for an elastic continuum, there exists an infinite number of such nodes. In the finite element method, a continuum may be approximated by an assemblage of suitably chosen geometrical elements (e.g. triangles, quadrilaterals, tetrahedra etc.) interconnected at a discrete number of points lying on their boundaries.

The determination of the displacements of these nodal points when the structure is subsequently deformed, is the central core of the method. Since the elements are assumed to be interconnected only at a limited number of nodal points, the relevant elastic characteristics of an element are represented by the relationship between the forces applied to the nodal points and the resulting displacements expressed as the FLEXIBILITY OR STIFFNESS of the element.

It must be pointed out that whilst some approximation is involed in the discretisation of the structure, its subsequent mathematical analysis is exact. Equilibrium and compatibility conditions must be satisfied in each element. The analysis can be approached either by the force or the displacement method as in conventional structural analysis. However, it has been found that in general, the displacement method provides simpler formulation and computer programming work for complex structures (32). In the present work, this approach has been followed.

2.2 DISPLACEMENT FUNCTIONS

In deriving the stress-strain relationship of an element, first, a displacement function has to be chosen to define uniquely the state of strain within an element in terms of its nodal displacements, and such as to ensure compatibility of deformation of adjacent elements. For triangular plane stress elements linearly varying displacements in two orthogonal directions would produce compatible deformation patterns. In this case straight lines in the body will remain so after deformation and contact between boundaries will be maintained.

This displacement function also implies constantcy of strains within an element and therefore in regions where the strains vary rapidly, smaller size elements would be required to give more accurate results.

2.3 DERIVATION OF THE ELEMENT CHARACTERISTICS

The characteristics of a "finite element" may be derived by rigorous methods of structural analysis as by the use of energy principles. Zienkiewicz (33) has presented a direct physical approach and this is followed here.

(i) General Structural Relationships

If the forces acting at the nodes of an element e within a structure, is represented by a matrix $\{F\}^e$, and the corresponding nodal displacements by $\{\delta\}^e$, then if the element is Hookean in behaviour,

$$\{F\}^e = [k]^e \{\delta\}^e + \{F\}_p^e + \{F\}_0^e \qquad (2.1$$

$\{F\}_p^e$ represents the nodal forces required to balance any distributed loads acting on the element, e.g. body forces; $\{F\}_0^e$ the nodal forces required to balance any initial strains, e.g. caused by temperature change, initial lack of fit etc., without any rigid body movement. The first term represents forces resulting from the nodal displacements and the matrix $[k]^e$ in the stiffness matrix.

Similarly, the stresses $\{\sigma\}^e$ at any point in the element may be expressed by the relationship:

$$\{\sigma\}^e = [S]^e \{\delta\}^e + \{\sigma\}_p^e + \{\sigma\}_0^e \quad \ldots\ldots\ldots \quad (2.2$$

where the matrix $[S]^e$ is the element stress matrix. $[\sigma]_p^e$ and $[\sigma]_0^e$ are the stresses resulting from distributed loads and initial strains respectively.

(ii) Displacement Relationships

Figure 2.1a is a triangular mesh drawn in a Cartesian Coordinate system and i, j, m are the nodes of a typical element e. The displacements at any point in the element may be expressed generally as:

$$\{f(x,y)\} = [N]\{\delta\}^e = [N_i, N_j, N_m \ldots] \begin{Bmatrix} d_i \\ d_j \\ d_m \\ \vdots \\ \vdots \end{Bmatrix} \quad \ldots\ldots\ldots \quad (2.3$$

The elements of N are in general functions of position chosen so as to obtain appropriate nodal displacements.

(iii) Strains

The strains $\{\epsilon\}^e$ at any point can be expressed in terms of the nodal displacements as:

$$\{\epsilon\}^e = [B]\{\delta\}^e \quad (2.4$$

where [B] is derived from the displacement functions and also expressed in terms of the coordinate of the nodal points.

(iv) Stresses

Denoting any initial strains by temperature changes, shrinkage etc. by $\{\epsilon_0\}^e$ and assuming elastic behaviour, the stresses within an element can be written as:

$$\{\sigma\}^e = [D](\{\epsilon\}^e - \{\epsilon_0\}^e) \quad \ldots\ldots\ldots\ldots \quad (2.5)$$

where [D] is the elasticity matrix containing the relevant material properties.

(v) Nodal Forces

The nodal forces, $\{F\}^e$, must be made statically equivalent to the actual boundary stresses and distributed loads. To do this, the principle of virtual work may be resorted to. If virtual displacements are imposed on the nodes, the external and internal work done by the various forces and stresses must be equal. When this is done a final expression of the form:

$$\{F\}^e = (\int [B]^T[D][B]dv)\{\delta\}^e - \int [B]^T[D]\{\epsilon_o\}\,dv - \int [N]^T\{p\}dv \ldots\ldots (2.6)$$

is arrived at, after integrating over the volume of element.

Comparing the form of equation 2.6 with that of equation 2.1, the stiffness matrix is readily recognised as:

$$[k]^e = \int [B]^T[D][B]dv^* \quad \ldots\ldots\ldots \quad (2.7$$

the nodal forces due to distributed loads are:

$$\{F\}_p^e = -\int [N]^T\{P\}dv \quad \ldots\ldots\ldots\ldots \quad (2.7$$

and those due to initial strains are:

$$\{F\}_0^e = -\int [B]^T[D]\{\epsilon_0\}\,dv \quad \ldots\ldots\ldots\ldots \quad (2.7c$$

---

* See Appendix I

2.4 GENERAL REMARKS

(i) In the above direct derivation of the characteristics of the finite element, distributed stresses on the element boundaries were replaced by equivalent static loads at the nodes. The validitiy of this may however be established by a more rigourous procedure by minimising the total potential energy of the system, e.g. see Appendix I; the finite element procedure is therefore identical with the Ritz method (34).

(ii) Since the equivalent forces are concentrated at the nodes, equilibrium conditions are satisfied in the overall sense only. This would give rise to local stress concentrations and equilibrium within each element and on its boundary would be violated.

(iii) It has been shown that for fully compatible displacement functions, the strain energy of the idealised structure is always below that of the exact solution (35). Thus the results of the analysis represent a lower bound solution.

2.5 COMPUTATIONAL PROCEDURE

(i) Evaluation of Stiffnesses

The first step in the analysis is to evaluate the stiffness properties [k] of the individual elements using the relationship equation 2.7a in a convenient coordinate system, e.g. as in figure 2.1a. The matrix [k] is square, the size of which depends on the number of degrees of freedom of the element. For example, in a plane stress problem of triangular elements, the total number of degrees of freedom of the element is six, (two

component displacements for each of three nodes), resulting in a 6 x 6 matrix. The individual element stiffness contributing to each nodal point are then superimposed to obtain the total assemblage nodal stiffness matrix [K].

(ii) Solution of Equilibrium Equations

The next step is the formulation and solution of the equilibrium equations. The equilibrium equations may be expressed in the form:

$$\{F\} = [K]\{\delta\} \qquad \ldots\ldots\ldots\ldots \qquad (2.8$$

The solution of the equations in the program used in this work is achieved by the Gauss-Seidel iteration procedure which is a systematic relaxation technique starting with any known or assumed values of nodal displacements. The basis of the method is given in Appendix (III).

(iii) Stresses and Strains

With the nodal point displacements evaluated, direct substitution into equations 2.4 and 2.5 gives the strains and stresses respectively.

2.6 APPLICATION TO PRESENT WORK

The present problem under investigation is the shrinkage and adhesive stresses in fibre reinforced composites. The fibres are assumed to be long and continuous making the assumption of plane strain conditions valid. They are also considered to be in the form of either an infinite hexagonal or triangular array within the matrix. Figure 1.1 shows the cross-section of such a composite with seven fibres.

A uniform temperature change (as far as fabrication stresses are concerned this is usually a drop) is imposed on the system and it is required to evaluate the resulting stresses due to the differential shrinkage assuming complete adhesion between interface. The material properties of the components of the composites are assumed to remain constant over the whole temperature range considered.

(i) Thermal loads

In general, if any elastic body is subjected to a change in temperature, strains are set up within it. For an isotropic homogeneous body these strains will also be isotropic. For the case of plane stress or plane strain there would be no shear strains and the initial strain matrix $\{\epsilon_0\}$ in a Cartesian Coordinate system is:

$$\{\epsilon_0\} = \begin{Bmatrix} \epsilon_{xo} \\ \epsilon_{yo} \\ \gamma_{xy} \end{Bmatrix} = \alpha \begin{Bmatrix} \Delta T \\ \Delta T \\ 0 \end{Bmatrix} \quad \ldots\ldots\ldots\ldots \quad (2.9a)$$

for the plane stress case where α is the coefficient of thermal expansion, ΔT the change in temperature, and γ_{xy} the shear strain.

It can be easily shown that for the case of plane strain, due to the presence of a third stress component σ_z perpendicular to the x-y plane, the initial strain matrix modifies to:

$$\{\epsilon_0\} = (1+\nu)\alpha \begin{Bmatrix} \Delta T \\ \Delta T \\ 0 \end{Bmatrix} \quad (2.9b)$$

where ν is the Poisson's ratio.

The thermal strains induced in a homogeneous isotropic body do not produce any stresses if the body is not subject to any constraints. However, for a composite body, the differences in the thermal expansion coefficients of the component materials, would tend to establish mutual constraints setting up a system of internally self-equilibrating forces.

In the finite element analysis, assuming all nodal points to be completely restrained, the equivalent nodal forces due to the temperature change in the elements, are calculated from equation 2.7c. In order to eliminate these forces the system is analysed for nodal point loads which are equal in magnitude but opposite in sign to these restraining forces. The final (self-strained) thermal stress distribution is the sum of stresses due to these thermal loads and the initial stresses in the externally restrained system, as given by equation 2.5

2.7 BOUNDARY CONDITIONS

The hexagonal arrangement of the fibres gives rise to a multifold symmetry. Any triangle such as OAB in figure (1.1) would therefore contain all the required information. It is therefore only necessary to isolate such a 'unit' for analysis by imposing the correct boundary conditions on it.

The boundary lines OA, AB and OB, being lines of symmetry, do not transmit any shear stresses. Also in the resulting deformation due to the thermal strains, the geometrical shape of the triangle OAB is preserved. Referring to figure 2.1b the boundary conditions are as follows:

a. Point 0 is fixed with respect to the whole system, i.e. no movement of the nodal point at 0 is permitted. Displacement of all other nodes are therefore obtained relative to this reference point 0.

b. The nodal points on OA are allowed to move only in the x-direction, i.e. no shearing is permitted across OA , the nodal point forces having only components normal to this boundary.

c. Along AB, the nodal points are free to move in both the x-directions and y-directions with the x-displacements being made equal to that at point A, and

d. On OB, the nodal points are free to slide along OB, and the nodal point forces must act perpendicular to this boundary.

The iteration procedure is effectively a relaxation procedure (34), the final correct displacements worked out will correspond to those that would impart a condition of minimum potential energy to the system.

2.8 ACCURACY

Inaccuracies in the finite element method, generally arise from:

(i) the discretisation of the continuum into a mesh of elements,

(ii) the representation of the loading conditions and boundary restrictions, and

(iii) the convergence of the iterative solution of the equilibrium equations.

As mentioned earlier due to the choice of linear displacement functions and hence constant strains in the elements, the size of the elements is governed by the strain gradients within the actual system under study. The storage capacity of the Imperial College IBM 7094 computer used in this analysis, limited the mesh size to about 400 elements. However, at the time of writing, new computing facilities are available using the much larger and faster CDC 6600 computer. This is capable of dealing with a mesh size of up to over 2000 elements.

On examination of the equations giving the thermal loads at the nodes, i.e. equation 2.7c and 2.9 it would appear at first sight that all nodal points are effectively loaded thus giving rise to several regions of local stress concentrations and affecting the general accuracy of the results. However, when summations are taken at each node over all the elements according to eqn. A·2(vi) the only loads remaining in the mesh, are those at the boundaries and at the interface nodes. Thus mesh refinement would be mandatory not only in the region of the

interface for the two reasons of high strain gradient and nodal forces, but also at the boundaries where elements are supposed to be free of shear stresses. With the limitation imposed by the size of the computer on the number of elements, this was difficult to achieve if enough small elements were concentrated in the regions of greatest gradient. The result was that the final solution gave shaar stresses in the boundary elements thoug of small orders compared with the direct stresses. Therefore, in plotting the stress distribution along the boundary lines, stresses in adjoining elements were averaged.

The rate of convergence of the iteration procedure was found to depend not so much on the mesh size as the regularity of the mesh, the type of boundary constraints and the order of operations along the boundaries. In general using an over-relaxation factor of 1.95 (see Appendix III) convergence was obtained after about 500-800 cycles depending on the particular mesh.

The computer programme employed in this investigation has been developed from one by Wilson (36). The various formulations involved are given in Appendix II and a Fortran Programme Listing is provided at the end of this thesis.

CHAPTER 3

FINITE ELEMENT ANALYSIS OF CONTINUOUS FIBRES

3.1 INTRODUCTION

Both analytical and experimental studies in the stress distributions in multifibre composites under external loads have been successfully conducted (28), (37), (38). The finite element method makes possible the study of stress distributions in composite materials under various loading conditions and for different fibre volume fractions (V_f). In addition to providing a numerical check on the validity of the postulates on the shrinkage mechanism made in chapter 1 the finite element method also affords a means of studying shrinkage stresses in various practical fibre-matrix combinations and to determine the effect of their elastic properties on the stress distribution. With the knowledge of these initial stresses, the effect of any externally applied stresses can be more fully appreciated.

3.2 COMPOSITE MATERIALS

The various composite systems studied fall into three main groups as follows:

(i) The first group is the commonest and perhaps best-known category of practical composite materials employing long glass fibres in a plastic matrix. Here, a relatively weak, brittle and low density matrix is strengthened by a much stronger fibre, usually glass; stronger fibres e.g. carbon fibres are also being used to achieve high strength to weight ratios for aero-engine components as recently announced by Rolls-Royce Ltd. (England).

(ii) The second group of composites use very strong fibres in the form of whiskers e.g. carbon, iron, sapphire whiskers which are potentially very strong - the strength in some cases approaching their theoretical crystal strength (39). These have high melting points with usable strengths at elevated temperatures in excess of those sustained by the available high temperature alloys. They are brittle and fracture without any plastic deformation and have small thermal expansion coefficients. The metal whiskers, e.g. iron, though initially strong, tend to lose strength due to the introduction of dislocations (6); the oxide whiskers, e.g. sapphire (Al_2O_3), in addition to being free from dislocations are less chemically reactive, the main problem being the difficulty in achieving effective bonding with the matrix. Sapphire/silver composites have provided useful experimental models for the study of whisker reinforced composites (41). The growth and properties of whiskers have been extensively reviewed by Coleman (9).

(iii) The third category of composites have metal wires (e.g. strainless steel wire, tungsten wire etc.) as fibres in a ductile metal matrix. However, metal wires lose strength very rapidly at elevated temperatures and are prone to alloying with the matrix thus causing further deterioration in strength. The relative ease of manufacture of the wires and incorporation into the matrix makes them attractive; tungsten-copper composite have been extensively used to obtain fundamental information on the mechanics of fibre-reinforcement (42), (43).

Most of these composites are formed by either hot pressing or direct infiltration methods both of which involve operations at temperatures above the ambient. It is therefore obvious that initial stresses resulting from thermal self-straining have to be properly appraised because their presence will directly influence the failure characteristics of the composite under external load.

3.3 COMPOSITE SYSTEMS INVESTIGATED

Various fibre volume fractions (V_f) were considered - from the limiting case where the fibres lie in continuous contact with each other (V_f = 0.907) to very wide fibre spacing, (V_f = 0.179). Table 3.1 gives the list of the various packing factors 'm'*, and the corresponding values of V_f**.

PACKING FACTOR (m)	FIBRE VOLUME FRACTION (V_f)
2	.907
2.08	.838
2.125	.804
2.5	.580
3	.404
4.5	.179

Table 3.1: Packing factors and fibre volume fractions

*'m' has been defined as:
$$\frac{\text{distance between adjacent fibre centres (a)}}{\text{fibre radius } (\rho)}$$

**$V_f = 2\pi/m^2\sqrt{3}$

Table 3.2 gives a list of materials from which the composite systems which will be discussed were selected, their designated symbols and elastic properties. Table 3.3 shows the composite systems studied and their derived properties.

The critical fibre volume fraction (V_c) in Table 3.3 is that volume which must be exceeded or equalled for fibre strengthening of the composite to be achieved and the expression for it has been derived elsewhere, e.g. reference (6). With this amount of reinforcement, the strength of the composite exceeds the ultimate tensile strength of the matrix. The expression applies to continuous fibres and assumes no alteration in the work-hardeing characteristics of the matrix due to the presence of the fibres at small values of V_f. It has also been derived assuming that all the fibres break in a given cross section. However, in all the material systems studied, only the Al/ARL system was below V_c for m = 4.5 which was the widest spacing studied.

MATERIAL*	SYMBOL	YOUNG'S MODULUS (E) x 10^6psi	EXPANSION COEFFICIENT (α)x$10^{-6}/^{o}C$	POISSON'S RATIO	ULTIMATE TENSILE STRENGTH u(lb/m^2)
Glass fibre	GL	10	8.5	.22	500,000
Boron fibre	B	55	6	.213	350,000
Sapphire Whisker	Al_2O_3	74	8	.2	2,200,000
Graphite Whisker	C	98	1.6	.16	9,800,000
Araldite	ARL	0.46	63	.35	10,000
Copper	Cu	18	17	.343	60,000
Steel	Fe	30	13	.29	575,000
Silver	As	11	19.1	.367	30,000
Tungsten	W	50	4.5	.28	420,000
Aluminium	Al	10	24	.33	42,000

Table 3.2: Materials and Properties

*The material properties have been obtained mainly from references (6), (44), (40), (7).

FIBRE (f) / MATRIX (m)**	$\frac{E_f}{E_m}$	$E_f - E_m$	$\alpha_m - \alpha_f$	V_c*
Al / ARL 1	20	9.5	19	.24
GL / ARL	20	9.5	44.5	.02
B / ARL	110	54.5	57	.03
GL / Al	1	0	15.5	.084
Fe / Al	3	20	11	.073
W / Cu	2.78	32	12.5	.143
C / Fe	3.27	68	11.4	.058
Al_2O_3 / Ag	6.7	63	11.1	.014

Table 3.3: Composite systems and derived properties

* V_c is the minimum volume of fibre necessary for strengthening to be achieved and it is given approximately by the expression $V_c = u_{(m)} / u_{(f)}$

** The suffix 'm' refers here to matrix and must not be confused with 'm' when used as packing factor.

3.4 COMPUTED RESULTS

Following the arguments in Chapter 1, a hexagonal packing arrangement of the fibres was adopted; they were also regarded as long and continuous in an infinte array. The computer programming procedure has been described in Chapter 2. Figure 3.1 shows a typical mesh used in the analysis; Table 3.4 shows the different mesh sizes for each packing factor m.

m	Number of Elements	Number of Boundary nodes
2	310	62
2.08	339	55
2.125	310	46
2.5	364	44
3	386	48
4.5	343	57

Table 3.4: Mesh sizes

Convergence of the solution was obtained in each case after about 500 cycles of iteration and the computing time on the IBM 7094 (at Imperial College) was around two minutes. On the CDC 6600 (at University College) the time was reduced to about thirty-five seconds using on all occasions an over-relaxation factor of 1.95. Plane strain conditions have been assumed in all cases.

3.5 RESULTS

The stress distributions within the matrix and along selected lines of symmetry have been plotted. Figure 3.2 shows these lines - namely ox, o'z, and the points A, B, and C which will be constantly referred to in the rest of the work. ox is the line of centres of adjacent fibres and o'z is inclined at 30° to ox; B and C lie on the interfaces along ox and o'z respectively and A is the isotropic point as will be seen from a later Chapter. θ - is the angular displacement along the interface measured from ox; all the computed results correspond to a uniform temperature drop of $50^{\circ}C$.

(i) Stress distribution along ox

Figures 3.3a-3e show the radial stress distribution on ox within the matrix, for various fibre volume fractions and composite systems. The following observations can be made from the graphs*.

a) For all the composite systems the radial stress distribution on ox is nearly uniform for densely-packed fibres and the stresses are all compressive. For the case of the closely packed fibres i.e. m = 2.08, these stresses slightly decrease from o to the interface and vice versa, for all other packing factors. For the widely spaced fibres, the radial stresses tend to follow a Lamé-type distribution as would be expected, see Figure 3.3e.

---

* On some of the graphs, not all the composite systems have been represented. This is purely to avoid over-crowding the graphs. However the general trend of the stresses is always evident.

b) The C/Fe system which has the largest values of Young's Modulus both for the matrix and fibre, produced the highest stresses at all points along ox for all fibre volume concentrations, whilst the Al/ARL, GL/ARL and B/ARL systems having the least value of Young's Modulus for their matrices, also showed the least level of stresses. It therefore seems that the level of the stresses mainly depends only on the properties of the matrix and not those of the fibres. Thus all the Araldite systems which have fibres with their Modulii an order of magnitude different (B(55), Al,GL(10)), all give the same order of stresses. The same form of distribution is exhibited by the GL/Al and Fe/Al systems having the common matrix aluminium. Also, the Al_2O_3/Ag system shows similar order of stresses to the Al-matrix system since Ag has almost the same values of modulus and thermal expansion coefficient as Al.

In the light of the above observations, the radial stresses at the interface 'B' were plotted against the matrix moduli for each packing factor as shown in Figure 3.4a. A linear relationship thus exists between the radial stresses and the Young's Modulii of the matrices. The curve for the case of m = 2 has been drawn using the contact stresses within the fibres. Figure 3.4b shows the variation of the interfacial radial stress at B with the reciprocal of the thermal expansion coefficient. Here, there is no linear relationship but the points all lie on a curve for each spacing, the stresses increasing with $1/\alpha_m$. In figure 3.4c, the variation of the

radial stress at B, with the derived parameters $(E_f - E_m)$, α_m/α_f and $(\alpha_m - \alpha_f)$ is shown plotted for different fibre spacings, for the composite systems all having Araldite as matrix. A linear relationship is exhibited in all cases. No sensible relationship was however found between the stresses and the ratio of the Young's Modulii (E_f/E_m).

The variation of the interfacial radial stress at B with m is shown in Figure 3.6a for the different composite systems. The shapes of the curves however apply to any point along ox. From these curves, stresses within the matrix for all the composite systems increase sharply from around m = 2 to their maximum values at a value of m between 2.2 and 2.25. Beyond this value, the stresses decrease, at first sharply up to m = 2.5; thereafter they gradually tend to the stress distribution for a single fibre configuration.

(ii) Stress distribution along o'z

The variation of radial stresses in o'z is shown in Figures 3.5a-5f. Here, the spacing of the fibres and the Young's Modulus of the matrix material, are significant in determining both the sense and magnitude of the stresses.

a) Closely-packed fibres

Figure 3.5a shows the curves for the different systems for the case of the fibres lying in continuous contact i.e. m = 2. All the stresses are tensile everywhere along o'z increasing from the interface to a maximum at the isotropic point A, at the centre of the tricorn. These stresses are very sensitive to slight changes in the spacing of the fibres.

As the spacing is slightly increased to m = 2.08, Figure 3.5b, the composite system with Araldite as matrix continue to show tensile stresses whilst in all the other systems the stresses have become compressive. The compressive stresses are maximum at the interface decreasing to a minimum at the isotropic point. Thus algebraically, the mode of variation of the radial stresses is the same for all fibre spacings. For m = 2.125, Figure 3.5c, the variation of the stresses for the Araldite systems is only partly tensile, beginning with tension at the centre of the tricorn and changing at about half way along o'z to compression. The value of m at which the stresses change from tensile to compressive can be obtained from Figure 3.6b which shows the variation of radial stresses at the centre of the tricorn A, for the different composite systems.

b) Widely-spaced fibres

For widely-spaced fibres and for all the composite systems the stress variation along o'z is similar to that on ox previously examined; the stresses are compressive and increase as the fibres become more closely packed, the peak compressive stress for each spacing occurring at the interface C. However, the distribution changes rapidly as the spacing is reduced below m = 2.5 for the soft ARL matrix composite systems.

(iii) Stress Distribution Along Interface - θ-direction

The variation of radial stresses along the fibre/matrix interface is shown in Figures 3.7a-7c. The radial stresses have been plotted against the angular distance θ along the interface.

Figures 3.7a-7b show the stress distributions along the interface for m = 2 and m = 2.08 respectively, showing part-compressive stresses even for m = 2. At first sight this would seem to conflict with our explanation of the shrinkage mechanism, that because of the difference between the coefficients of thermal expansion ($\alpha_m > \alpha_f$), the matrix material must be in tension when the fibres touch. Certainly the major part of the matrix material experiences radial tension in these circumstances, but in order for adjacent fibres to remain in equilibrium under the radial tensile, stresses from the matrix, the fibres must press on one another and if a thin strip of matrix material separates them at the closest points it must be in compression. The stress distribution is similar to that shown in Figure 1.2d. The thinner the strip of material separating the fibres, the more uniform the compression within it. In the limit when the fibres touch (m = 2) the radial stresses at $\theta = 0$ becomes the compressive stress in the fibre along the line of contact.

Figures 3.8a-8b show the general distribution of radial tensile and compressive stresses within the matrix for both stiff and soft matrix materials for closely spaced fibres. The tensile stresses originate from the centre of the tricorn and the compressive stresses within the vicinity of the contact points of the fibres are confined to only a small area as explain above. It is also clear that the softer matrix has a far greater tendency to develop tensile stresses whilst the stiffer matrix produces the type of compressive stresses as described above even when the fibres touch.

As the fibre spacing increases, the interfacial radial stresses everywhere become compressive for all the composite systems, and tend to be uniform. In Figure 3.7c the two extreme cases, namely C/Fe and AL/ARL are shown for packing factors equal to 2.125 and 4.5

The significance of these results in relation to composite materials will be discussed later.

CHAPTER 4

SHRINKAGE STRESSES AROUND A DISCONTINUOUS FIBRE

4.1 INTRODUCTION

In the last chapter, the shrinkage stresses in a solid composite having cylindrical continuous fibres were investigated. However, since many fibres are available in the form of short fibres, it is important also to study the shrinkage behaviour of discontinuous fibre composites.

Both the theoretical and experimental analyses of continuous fibre composites are relatively easy to achieve since they can be successfully idealised and made amenable to elastic analysis or simulated closely in experiments. Cox (1) has provided an analysis of a single fibre in an infinite matrix using a strength of materials approach; experimental work has also been carried out by Tyson and Davies (3) and Schuster and Scala (45), providing information on the shear tractions on the fibres.

4.2 DISCONTINUOUS FIBRE COMPOSITE MODELS

Iremonger and Wood (4), (38) and Owen et al (30) have all used both two-dimensional photoelastic and finite element models to study the stresses around fibre discontinuities of various sizes and for different fibre volume concentrations, in both the elastic and elastic-plastic regions. In all these cases, the effect of neighbouring fibres adjacent to the discontinuity was also examined. However, practical fibres invariably have circular cross-sections and are all completely surrounded by the matrix material; plane models used in the

above investigations and simulating the longitudinal section of the real composite inherently overlook this fact. It is obvious, therefore, that whilst such analyses may yield valuable information towards a better understanding of fibre-reinforcement the models adopted for the studies are only convenient approximations to the real composite. If we consider, for instance, the effect of compression in the axial direction of the fibres in the two cases of the plane model and the real composite, the response to the load would be different. For the composite, the 'holes' occupied by the fibres would tend to increase in diameter due to the Poisson's ratio effect to a greater extent than the diametral expansion of the fibres since $\nu_m > \nu_f$ generally, thus resulting in the establishment of transverse tension to maintain interfacial coherence. Various analytical expressions for the transverse radial stress developed at the interface, have been derived by Islinger et al (46) and Mooney and McGarry (47) for both single and multifibre composites. Ebert and Gadd (7) have extended the analysis into the plastic yielding using as the model a composite with a central soft core surrounded by a rigid cylindrical case.

In the case of the plane model, the reverse effect would take place since the matrix lying between adjacent fibres would expand laterally against the fibres which also expand to augment the compressive effects. Herein lies the major inadequacy of the plane model simulation. However, in real composites, most of the load (>80%) is borne by the fibres, the matrix serving merely as a binder and shear force transmitting medium. Under these conditions the Poisson's

ratio effect in the matrix may be negligible. It is therefore necessary that in the simulated plane models v_f and v_m should be approximately equal and the ratio E_f/E_m should be high to realise this. However, it has been shown that the effects due to v_f and v_m alone are negligible (29) in plane models.

4.3 MODEL FOR THERMAL SHRINKAGE ANALYSIS

The object was to study the shrinkage stresses around a discontinuity in a multifibre composite. From the foregoing, it was felt that a better idealisation of the composite ought to be considered. It was argued that in that part of the matrix lying directly between the ends of the fibres in a discontinuity, axisymmetric conditions would prevail to a good approximation. Figure 4.1 shows the longitudinal cross-section and plan view of such a model. It is composed of a central long cylindrical fibre with a central discontinuity and surrounded by the matrix material which is in turn surrounded by a ring of material assigned the elastic properties derived from the rule of mixtures for the composite. The outermost ring of material is the same as the matrix. The problem is therefore that of shrinkage stresses in concentric cylinders with a central discontinuous core. The analytical solution of such a problem (without the discontinuity) has been proposed by Gatewood (48) using Complex Variable analysis.

It is readily recognised that the shrinkage mechanics in the proposed axisymmetric model is different from those of real composites. In addition since most investigations have been

conducted on the plane model to advantage, it was felt that this (the plane model) should be adopted even if only to make a comparison of results possible. Note that the longitudinal section for the axisymmetric model in figure 4.1 serves also as the plane model. For the finite element analysis, due to symmetry, only one quarter of the plate (Figure 4.1) was considered. The point o was fixed and nodal points along ox and oy permitted to slide only along their respective axes, all other nodal points being allowed to move freely. The number of elements of the mesh employed was 966 (528 nodes), permitting all necessary mesh refinement in the appropriate regions. The University College computer CDC 6600 was used for the analysis. Computing time was just over one minute after 500 cycles of iterations, using as before, an over-relaxation factor of 1.95. Two composite systems were studied - namely C/Fe and AL/ARL, the two extreme cases in Chapter 3. Packing factors of m = 4.5 and 2.5 and discontinuities $\frac{\delta^*}{\rho} = 1$ and 2 were investigated for each system.

4.4 RESULTS

The stress distributions for both the C/Fe and Al/ARL systems were similar and the plots are mainly shown for the C/Fe system. The stress levels were of course different, the C/Fe system giving higher stresses.

$^*\frac{\delta}{\rho} = \frac{\text{length of gap } (\delta)}{\text{radius of fibre } (\rho)}$

(i) Axial Stresses

Figure 4.2a shows the axial stresses in the plane model, in the centre line of the longitudinal section starting from the centre of the discontinuity in the matrix, i.e. along o_y in Figure 4.1. These stresses are tensile in the matrix and rapidly decrease, changing to compressive in the fibre. Perfect continuity of stress from matrix to fibre is exhibited in all cases. The magnitude of the compressive stresses in the fibres increases to a maximum constant value a few gap-lengths along the fibre. The axial stress magnitudes are influenced more by the size of the discontinuity than by fibre proximity or spacing for the two fibre spacings investigated.

(ii) Radial Stresses on ox (Figure 4.1)

Starting from the interface at the outer fibre along ox' the stress distributions in the direction perpendicular to the axis of the fibre for both the C/Fe and Al/ARL systems have been plotted up to o', the centre of the discontinuity, Figure 4.2b. These stresses are all positive and increase along ox' from the interface. For the same discontinuity higher stresses are obtained with increasing fibre spacing but the stresses are nearly the same at the interface for the same spacing. fig.79

In Figure 4.2c, both the plane and axisymmetric stress distributions for m = 4.5 and $\delta = \frac{1}{4}$ for the Al/ARL systems have been shown for comparison, the axisymmetric case giving much lower stresses.

(iii) Shear Stresses

The interfacial shear stresses along the central discontinuous fibre starting from the tip of the discontinuity in direction oy (Figure 4.1), are shown plotted in Figure 4.2d. For both fibre spacings, the tip maximum shear stresses are the same for all discontinuities; however, the shorter the discontinuity and the closer the fibres the slightly longer the distance along the fibre over which shear stresses persist. They all fall to zero in just over one fibre width.

4.5 RELATIONSHIP OF RESULTS TO REAL COMPOSITES

The plane model adopted in the analysis excludes circumferential stresses which arise in real composites from the fact that the fibres are completely surrounded. Instead, the central fibre is bounded on either side completely by other fibres; the matrix is thus in effect surrounded by a fibre material which is the reverse of conditions in a real composite. In the shrinkage process, the shrinkage of the matrix material at the outer fibre interface would be greater than that of the fibre ($\alpha_m > \alpha_f$) and hence interfacial tension would be required to maintain adhesion. This is equally true of the axisymmetric model in which the inner cylindrical matrix (Figure 4.1) would tend to shrink inwards, away from the intermediate material. The effect of the differential contraction is therefore to establish tensions and not compression as explained in Chapter 1, for all fibre spacings. This is borne out by the results. The results therefore pertain more to the particular geometry of the models than to real composites.

A more realistic simulation of fibre discontinuity is by a three-dimensional discretisation of the finite element method. This would however require a large total number of elements to achieve a reasonable physical approximation. The feasibility of this is limited by the storage capacity and speed of the computer, and this was the main reason for not using this approach.

An experimental simulation of fibre discontinuity will be presented in the ensuing chapters using photoelastic methods.

CHAPTER 5

PHOTO-VISCOELASTIC BEHAVIOUR OF BIREFRINGENT MATERIALS

5.1 The Basic Principles of Photoelasticity

When a ray of light enters a transparent isotropic medium, it suffers a change in velocity. The ratio of the velocity in vacuo to that in the medium is the refractive index of the medium and it is independent of the direction of propagation and state of polarisation of the ray.

In anisotropic transparent media, such as strained or drawn high polymers the behaviour is more complicated. In general a single ray entering such a material is propagated as two separate orthogonally polarised components travelling with different velocities, each parallel to a direction of secondary principal stress in the plane of the wavefront. Both the velocities and the state of polarisation vary with the direction of propagation. This phenomenon is known as double refraction and the body is said to be birefringent. The principles of photoelasticity are based on this property of double refraction exhibited by most polymeric materials and glasses.

For polarised light of a given wavelength incident normally in a plate under plane stress conditions the velocities of the component rays v_1, v_2 are each proportional to the magnitude of the principal stresses σ_1, σ_2, lying in their planes of vibration, i.e.:

$$v_1 \propto \sigma_1, \text{ and } v_2 \propto \sigma_2 \quad .$$

Thus on emerging from the photoelastic medium the two components will have suffered a relative change of phase or RELATIVE RETARDATION, such that $\chi \alpha (v_1 - v_2)t$, where t is the length of the path of the ray through the medium. (This will be the thickness of the medium for normally incident light).

Since $(v_1 - v_2)$ is proportional to $(\sigma_1 - \sigma_2)$ we can say that

$$\chi = C(\sigma_1 - \sigma_2)t \quad \ldots\ldots\ldots \quad (5.1)$$

where C is a constant for a given material at a given temperature and is known as the STRESS-OPTIC COEFFICIENT.

On viewing the emergent ray through another polaroid material (usually called ANALYSER), with its transmission axis perpendicular to the initial plane of vibration (i.e. axis of the POLARISER) only the components of those two waves which are parallel to the ANALYSER transmission axis can be observed. When the value of X is such that the ray components for the analyser are out of phase by π radians, mutual extinction will occur, producing zero light intensity at every point in the medium having a similar value of principal stress difference $(\sigma_1 - \sigma_2)$. The loci of such points form fringe patterns called ISOCHROMATICS. A complete analysis, may be found in most texts on photoelasticity, e.g. reference (52)

Photoelasticity thus affords a direct means of obtaining the distribution of the principal stress differences in a stressed plate optically. There exists another parameter which can also be optically measured, the ISOCLINIC. This is the locus of all points in the plate at which the directions of principal stresses

are parallel to the axes of the polariser and analyser. From such loci, stress trajectories within the plate can be graphically plotted.

5.2 Photoelastic Methods

By making models of structures or components out of suitable birefringent materials and subjecting them to the required mode of loading, the resulting stress distribution can be conveniently obtained. In the main, photoelastic methods fall into two groups of analyses:

(i) two-dimensional analysis and

(ii) three-dimensional analysis.

The first method, by definition, is employed in the study of plane models (plane stress) elastically loaded for short periods to avoid creeping of the materials.

The second method is applicable to three-dimensional models made from polymeric materials and depends on the changes that occur in the molecular chains of the polymer at elevated temperatures. When loaded at a particular temperature known as the CRITICAL TEMPERATURE, the exact value of which depends on the composition of the particular polymer, the material deforms considerably almost instantaneously, with consequent sharp reduction in the value of its modulus. After unloading at that temperature, there is complete recovery without much delay. If

however, the loads are maintained whilst the specimen is cooled to room temperature, the deformation and optical effects produced at the critical temperature are retained on removal of the load. Hence the method is described as the FROZEN STRESS TECHNIQUE. To explain this behaviour of the birefringent material at the elevated temperature, a descriptive theory has been postulated in which the material is assumed to have two phases simultaneously having different properties, see e.g. ref. (50)

The ratio of relative retardation produced in the model to the load applied is actually much greater in the frozen stress than in a model at ordinary room temperature. The linear relationship, however, between the load and the stress-optical effects is retained for a wide range of loads so that the stress distribution may be determined from such a model. Also, the frozen stress pattern remains unaltered when the model is cut or drilled with care.

5.3 Photothermoelasticity

Comparatively, more recently, a new technique of photoelastic analysis is increasingly being employed in thermal stress problems (53) (54) (55). This method has been termed PHOTOTHERMOELASTICITY. The problem may be a purely thermal stress problem due to a non-uniform temperature distribution or stress resulting from differential shrinkage as in composite structural systems. In this method, also, both two and three-dimensional approaches are possible. This method differs from the conventional methods outlined above, both in the mode of loading and in the nature of the resulting isochromatic fringes. In the

conventional methods loading is externally applied whilst in the photothermoelastic approach, advantage is taken of the thermal loads induced as a result of any temperature gradients or the differential shrinkage of the components of a composite material due to a uniform temperature change. This technique will be examined in a greater detail in the next chapter.

In general, the isochromatics resulting from this approach will be due to a combination of frozen stress and creep effects and elastic stresses depending on the creep and thermo-viscoelastic properties of the birefringent materials used in the test. This technique has been employed in this investigation and to interpret the results correctly, an understanding of the behaviour of binefringent materials is imperative.

5.4 Viscoelastic Behaviour of High Polymers

The response of polymeric materials to any form of loading is, in general, highly time and temperature dependent. At very short loading periods, the material exhibits a Hookean elasticity, the ratio of stress to strain being constant and independent of time. At longer loading periods this ratio does depend on time; the strains may become large, but they are recoverable if the load is removed. This is called delayed or retarded elasticity*. At still longer times, some of the

---

*Also known as HIGH ELASTICITY

strain may become irrecoverable showing that the material has deformed in part like a liquid rather than a solid, this is called flow. (56) (57) (58).

(i) Creep Characteristics

From the foregoing, in a creep test at constant stress and temperature, the strain, ϵ , may be generally expressed as:

$$\epsilon(t) = \epsilon_1 + \epsilon_2(t) + \epsilon_3(t) \quad \ldots\ldots\ldots \qquad (5.2a)$$

the parameters ϵ , ϵ_1.... are measured at time t. ϵ_1 is the part corresponding to the instantaneous elasticity and hence is independent of t; $\epsilon_2(t)$ and $\epsilon_3(t)$ are the delayed and flow deformations respectively. $\epsilon_3(t)$ is assumed to depend on the time according to Newton's law for viscous liquids. Hence equation 5.2a may be expressed as:

$$\epsilon(t) = \epsilon_1 + \epsilon_2(t) + t/\eta \quad \ldots\ldots\ldots \qquad (5.2b)$$

where η has the dimensions of viscosity. Figure 5.1a shows the type of creep curve which would be obtained with a specimen which obeys these assumptions. At very short times, the deformation under load consists only of the instantaneous elastic deformation ϵ_1; it then behaves like a hard solid. Later there is a region of transition in which the high elastic deformation develops, and the compliance** of the material changes.

** Ratio of strain at any time to stress.

to that of a soft solid. This transition region covers several decades of time. The flow term t/η may have some effect during the high elastic deformation; at very long times this term may become dominant and the material then behaves like a very viscous liquid, figure 5.1a.

(ii) Strain recovery

A strain recovery experiment may follow a creep test. The stress is removed and while the specimen recovers, the strain is measured as a function of time. On removal of the stress there is assumed to be instantaneous recovery, corresponding to the instantaneous deformation ϵ_1. Then there is delayed elastic recovery which corresponds to ϵ_2. If there is complete recovery, then there has been no viscous flow ϵ_3. It may be difficult, however, to distinguish between flow and very delayed elasticity..

(iii) Stress relaxation

In a stress relaxation test, the strain ϵ, is held constant and the stress and modulus become functions of time. Figure 5.1b shows the type of curve that may be obtained in a relaxation experiment. The initial stress is high corresponding to an instantaneous elastic response. The stress then falls as delayed elasticity takes place and if there is no flow, the modulus eventually falls to a constant finite value corresponding to that of a soft solid. If flow occurs, the modulus and stress eventually decreases to zero.

The above behaviour may be expressed by an equation in terms of the modulus at zero time $G_{(0)}$ as:

$$G_{(t)} = G_{(o)} - G_{E(t)} \quad \ldots\ldots\ldots \quad (5.3a)$$

where $G_E(t)$ is a function describing the change in modulus caused by the delayed elastic response. Alternatively, the equation may be written in terms of the modulus at infinite time $G_{(\alpha)}$ as:

$$G_{(t)} = G_{(\alpha)} + G'_{E(t)} \quad \ldots\ldots\ldots \quad (5.3b)$$

If viscous flow occurs $G_{(\alpha)} = 0$.

Comparison of the two curves in figures 5.1a-1b, shows that stress relaxation and creep follows a similar course and are found to be identical in the hard and soft regions. In the hard region $G_{(o)} = 1/\epsilon_1$ and in the soft region:

$$G_{(\alpha)} = 1/[\epsilon_1 + \epsilon_{(\alpha)}] \quad \ldots\ldots\ldots \quad (5.3c)$$

if there is no flow. However, in the transition region, the experiments give results, which though similar, are not identical It is found that the centre of the transition region does not occur at the same time in creep and stress relaxation experiments

(iv) Effect of Temperature

The properties of high polymers vary greatly according to the temperature at which they are tested. At sufficiently low

temperatures all plastics are hard with Young's Modulus in the region of 0.3 - 1.0 x 10^6 lb/in^2. This state of the plastic is referred to as the GLASSY STATE.

In general, any linear polymer* can, depending on its temperature, exist in each of the following states:

(i) the glassy state,

(ii) the retarded highly elastic or leathery state,

(iii) the instantaneous highly elastic or rubbery state, and

(iv) the viscous state.

The glasssy state corresponds with the lowest temperature range and the viscous with the highest. These states roughly correspond to those demarcated in the creep and relaxation behaviour. For a cross linked polymer**, viscous flow should be prevented by the permanent character of the molecular network structure, except at exceptionally high temperatures.

The widths and temperature ranges over which any particular polymer exhibits these different types of behaviour and their general positions on the temperature scale depend upon the chemical and physical structure of its molecules. The temperature of the transition for state (i) to state (ii) is called the GLASS TRANSITION TEMPERATURE. Although the elastic modulus, viscosity, density and other physical properties decrease only slowly with increasing temperature in the glassy state, at the

---

* A linear polymer is one which has continuous unbranched molecular repeat units in its network structure (58).

** A polymer with network formed by the linking together of previously formed polymer molecules via boded chemical structures, e.g. vulcanised rubber.

transition temperature these quantities fall quite drastically over a narrow temperature range.

5.5 TIME-TEMPERATURE SUPERPOSITION PRINCIPLE

It has been observed by many experimenters (56) (57) (58), that the curves which represent the viscoelastic behaviour of a single polymer sample, determined at several different temperatures, are similar in shape when plotted against a logarithmic time base, log t. These curves can be exactly superimposed by simply shifting them along the log t axis. This is known as the TIME-TEMPERATURE SUPERPOSITION PRINCIPLE and it applies to curves of stress relaxation, creep and their allied derivatives. Thus one MASTER curve can be drawn from a series of tests at different temperatures for creep or relaxation.

5.6 TEMPERATURE-STRESS-OPTICAL RELATIONSHIP

Hitherto we have discussed the mechanical behaviour of birefringent materials. However, from the standpoint of the photoelastic investigation, the most important behavioural aspect of the material, is its optical response during the various mechanical states. This is required for an accurate interpretation of the fringes present in a model which may pass through any of these various states.

A simple theory of the photo-elastic properties of molecular networks of long chains of random links, has been developed by Crawford, and Kolsky (59) and Treolar (60),

transition temperature these quantities fall quite drastically over a narrow temperature range.

5.5 TIME-TEMPERATURE SUPERPOSITION PRINCIPLE

It has been observed by many experimenters (56) (57) (58), that the curves which represent the viscoelastic behaviour of a single polymer sample, determined at several different temperatures, are similar in shape when plotted against a logarithmic time base, log t. These curves can be exactly superimposed by simply shifting them along the log t axis. This is known as the TIME-TEMPERATURE SUPERPOSITION PRINCIPLE and it applies to curves of stress relaxation, creep and their allied derivatives. Thus one MASTER curve can be drawn from a series of tests at different temperatures for creep or relaxation.

5.6 TEMPERATURE-STRESS-OPTICAL RELATIONSHIP

Hitherto we have discussed the mechanical behaviour of birefringent materials. However, from the standpoint of the photoelastic investigation, the most important behavioural aspect of the material, is its optical response during the various mechanical states. This is required for an accurate interpretation of the fringes present in a model which may pass through any of these various states.

A simple theory of the photo-elastic properties of molecular networks of long chains of random links, has been developed by Crawford, and Kolsky (59) and Treolar (60),

from the kinetic theory of rubber-like elasticity. This theory predicts that at constant temperature, the difference between any two of the three principal refractive indices of a network in pure homogeneous strain is proportional to the difference in the two corresponding stresses. The constant of proportionality or stress optical coefficient is approximately inversely proportional to the absolute temperature and is independent of the degree of cross-linking of the network.

Experimental verification of the above theory has been obtained (61) for natural rubber and gutta-percha. In particular, it was shown that the stress optical coefficient is constant during creep and has the same value as for elastic equilibrium. In the same work it was found that the constant for amorphous cross-linked polythene and polymethylene, measured in their rubbery state (elevated temperatures), decreased markedly with increasing degree of cross-linking. This decrease can be accounted for on the basis of the theory of the photo-elastic properties of short chain molecular networks put forward by Treolar.

P. S. Theocaris (57) has carried out a series of creep and relaxation tests over a limited time interval, on both hot and cold-setting Araldite epoxy resins, and at temperatures up to the rubbery state. The characteristic mechanical and optical viscoelastic properties were derived from these tests; it was established from these tests that:

(i) The values of the stress-optical coefficient and the strain-optical coefficient are identical in creep and relaxation for various temperatures. Their corresponding master curves are

coincident and therefore the variation of birefringence follows the same law in creep as in relaxation.

(ii) The creep compliance master curves and the relaxation modulus master curves can be represented by functions which are the reciprocals of one another at any time. This shows the validity of the relationship established earlier in equations (ii) - (vi).

The significance of (i) will be appreciated in the next chapter on the experimental work which was conducted over a wide temperature range from the glassy state up to the transition.

CHAPTER 6

EXPERIMENTAL WORK

6.1 THE PHOTOTHERMOELASTIC TECHNIQUE

If an unrestrained homogeneous isotropic elastic body undergoes a uniform temperature change, then the state of strain produced in the material is everywhere isotropic. The expression for the strain e_T is,

$$e_T = \int_{T_o}^{T} \alpha dT$$

where T_o and T are the initial and final temperatures of the body and α the linear coefficient of thermal expansion; α may either be a constant or a function of the temperature. This thermal strain does not give rise to any stresses since the displacements are uniform and unimpeded. However if the body is subjected to any constraints or thermal gradients, stresses will be induced in it. If the thermal configurations of a structure are simulated by a model made from a suitable birefringent material, the resulting stress distribution can successfully be studied photoelastically. Three different kinds of thermal stress problems can be envisaged.

(i) Thermal stresses due to steady-state temperature gradients

This represents a class of problems in classical thermoelasticity and essentially conventional two-dimensional photoelastic techniques are employed except that the loading is thermal rather than mechanical. Such problems have been investigated (53) in order to verify the photothermoelastic method since exact solutions are available for certain

configurations, e.g. a long beam subjected to a steady-state parabolic temperature distribution. Some three-dimensional models, e.g. the long circular thick-walled cylinder, have been successfully studied by this method.

(ii) Transient Thermoelastic Problems

A sudden non-uniform temperature change applied to a body, produces stresses. In this case, the temperature distribution in the body and the associated strains and stresses all vary with time. By suitable instrumentation the isochromatics associated with the changing stresses can be obtained at desired intervals, (50).

(iii) Restrained Shrinkage Problems

The third class of thermal stress problems is encountered in bonded composite structures, e.g. reinforced solids and solid propellant grains for rockets. By comparison with the above types of problems (i) and (ii), these are the simplest to simulate experimentally. However they form an important and growing field of stress analysis by photothermoelastic techniques. When the bonded composite structure experiences any uniform temperature change, stresses are developed in it due to the differential expansion and also the differences in the elastic constants of the component materials. Thus by bonding a birefringent material to a second material, either by casting against it or by applying a suitable adhesive, the change in or development of birefringence with temperature may be observed. This method of analysis has been adopted in the present investigation which is presented below.

6.2 SHRINKAGE AND ADHESIVE STUDIES

The restrained shrinkage method has been used by many experimenters e.g Durelli et al (55) (62) for different shrinkage problems. The behaviour of birefringent materials, as described in the previous chapter, makes a preliminary study of the model materials to be used in any tests under varying temperature configurations imperative. In addition, in order to eliminate extraneous stress producing effects, during the experiment, certain characteristics are desirable in any material chosen for the tests.

(i) Desirable Properties of Test Materials

In the present study, which consists basically of casting a resin around metallic rods at an elevated temperature, the following qualities would have to be fulfilled by the test materials:

a) A hot-setting material with negligible or mild exothermic reaction during gelation. This is important in order to avoid an undesirable rise in temperature within the model as this might be non-uniformly distributed and give rise to stresses. With excessive exotherm, volumetric distortion might take place as well as the entrainment of air bubbles. This last factor is also influenced by the fluidity of the casting resin.

b) A negligible polymerisation shrinkage of the resin system is required so as to avoid stresses not purely due to thermal shrinkage which is mainly the consequence of moelcular rearrangement; the geometrical distortions e.g.

buckling produced by this kind of shrinkage in large plate models, for instance, can affect the thermal stress distributions.

c) Good bonding between the component materials is desirable since compatibility is a necessary condition of the shrinkage process as explained in Chapter 1. This should also leave the interface bond undisturbed on cutting the model into slices for photoelastic analysis.

d) The resin should possess a reasonably high figure of merit, Q, defined as $Q = E/f = n/\epsilon$ where E is the Young's Modulus, f the material fringe constant, n, the number of fringes and ϵ the strain. Hence Q is a measure of the fringe sensitivity of the material in response to strain.

(ii) Preliminary studies of resin systems

For the reasons stated above a preliminary study of the currently available photoelastic materials was carried out for the selection of the material best suited to the tests.

a) BAKELITE SR9098 + ACCELERATOR Q17448 + CATALYST Q17447 (SUPPLIED BY BAKELITE LTD.) This is a polyester resin in liquid form and can be cured at various temperatures. When tested, it exhibited excessive polymerisation shrinkage even on a macroscopic scale. A $\frac{1}{4}$ in. thick plate casting with a circular glass inclusion produced a severely buckled plate. The material also became soft at slightly elevated temperatures.

b) ARALDITE MY753 + HY922 (SUPPLIED BY CIBA LTD.)

This is a liquid cold setting resin and can be cured at various temperatures from room temperature upwards to about 100°C. It produced excessive exotherm with increasing casting temperature and size of casting and proved to be most unsuitable. However it had the advantage that since it can be cast and cured at various temperatures, the level of residual stresses and hence isochromatics resulting from a composite casting could be controlled by curing at a selected temperature.

c) ARALDITE CT200 + HT901 (SUPPLIED BY CIBA LTD.)

This resin is solid and melts at 120°C and may be cured successfully at 110°C - 150°C. When tested, it produced negligible polymerisation shrinkage and exotherm. Repeated tests with thermocouples located at the centre of a large mould in the form of a cylindrical vessel of the same dimensions as the mould to be employed in the main experiment (4.3 in. diameter and 7 in. long), showed that there was practically no exotherm at curing temperatures of 110°C - 120°C. The resin poured easily at 120°C without trapping any air bubbles. Its pot life was found to be about 2 - 3 hours at 110°C and solidification was complete after 5 - 7 hours. This meant that enough time would be available for the mould and its contents to attain a uniform cure temperature of the oven before the onset of polymerisation. This system has a high figure of merit and is widely used in this country and elsewhere for three-dimensional photoelastic work (63) (64). It was therefore adopted for the tests.

(iii) Choice of Fibre Material

Because of its excellent bonding with Araldite and its transparency, glass rods (E-glass) were first considered for the tests. However their unsuitability was soon discovered when on cooling the cast mould down to room temperature, repeated cracking of fibres and matrix was experienced; the whole matrix and fibres cracked rather drastically. Other alternative materials therefore had to be considered.

After tests with steel, copper, and aluminium (alloyed) rods, the last was selected for its ease of cutting, lightness, good bonding with Araldite, cheapness and availability. However, initially some difficulty was experienced in obtaining a good bond which would not break during the cutting process. Even careful and thorough abrasion and cleaning agents* could not improve this. Aluminium is highly chemically reactive; when exposed to the atmosphere, it quickly forms a protective thin coating of its oxide which prevents its further degradation. The higher the time and temperature of exposure, the thicker the oxide film formed and the more difficult it is to bond effectively with Araldite.

It is normal in most casting procedures to heat the mould to the same temperature as the molten resin before pouring so as to avoid distortions due to non-uniform temperature distribution. It was discovered that by pouring the Araldite into

---

*e.g. ethylene tetrachloride, acetone, etc.

the mould whilst the latter was still cold (room temperature), the rods having just been assembled after cleaning, the bond was considerably improved. Since the material gels over a long period, and as aluminium is an excellent heat conductor, the rods and vessel would soon attain the oven temperature. Adhesion was further ensured mechanically by cutting short shallow and narrow slots along the sides of the rods far removed from the regions of interest. The stress concentrations produced by these slots would be highly localised and would have no effect on the overall fringe patterns. The particular aluminium alloy selected was BSS/EIC supplied in $\frac{1}{2}$ in. diameter rod.

(iv) Properties of Araldite CT200 + HT901

The manufactures of this resin (CIBA Ltd. of Daxford, Cambridge) have extensive data on the mechanical and electrical properties of the material. (63).

Up to the glass transition temperature, 105-110°C, the material behaves in a brittle manner when tested over a relatively short period. The values of the Young's Modulus and the thermal coefficient of expansion remain practically constant over this temperature range. However, like all polymeric materials, it has a tendency to creep over a period of time.

The room temperature elastic fringe constant was obtained from a compression specimen and the frozen stress constant from tension specimens at 120°C the critical temperature. Table 6.1 gives the various properties of the araldite and

PROPERTY	ARALDITE*	ALUMINIUM+
(E) Young's Modulus, x 10^6 lb/in^2	0.46	10
(α) Expansion coefficient, x 10^6/°C	63	24
(v) Poisson's Ratio	0.35	0.33
(fe) Material Fringe Value, lb/in^2/in/fringe	55.5	-
(fr) Frozen stress fringe value, lb/in^2/in/fringe	1.438	-
(Ef) Effective Young's Modulus for frozen fringes, lb/in^2	2150	-
(Tc) Critical Temperature °C	120	-
(Tg) Glass Transition Temperature, °C	105-110	-

Table 6.1: Mechanical and Photelastic Properties of Araldite CT200 and Aluminium (EIC)

---

*Averaged from sample tests

+From "The Properties of Aluminium and its Alloys"; The Aluminium Development Association; Information Bulletin No.2.

aluminium. The resin/hardener weight ratio used here and in all subsequent tests, was in the recommended proportions of 100 parts to 30.

(v) Casting of Models

The geometrical arrangement of the fibres adopted in the tests was that of a hexagon for reasons already mentioned. Fortunately this arrangement has several planes of symmetry, thus simplifying the photelastic analysis which will be presented in the next chapter. Three different packing factors (m = 4.5, 3, 2.5), see Figure 1.1 corresponding to fibre volume fractions of 0.179, 0.403 and 0.580 were studied for both continuous and discontinuous fibres.

A base for each model was made from a disc of Araldite 1 in. thick, drilled for the required spacing and treated with release agent to prevent adhesion to main model. The disc located the seven aluminium rods accurately as the Araldite was cast around them in a cylinder about 7 ins. high and about $4\frac{1}{4}$ ins in diameter, also treated with release agent. Casting was carried out at 120°C followed by sixteen hours of furing at 110°C, the mould finally being slowly cooled to room temperature (20°C) at a rate of 2°C per hour.

For each packing factor, three different lengths of discontinuity were studied, namely $\frac{1}{4}$ in., $\frac{1}{2}$ in and $\frac{3}{4}$ in. These various configurations are tabulated below in Table 6.2.

m	LENGTH OF GAP			
4.5	0	$\frac{1}{4}$ in	$\frac{1}{2}$ in	$\frac{3}{4}$ in
3	0	$\frac{1}{4}$ in	$\frac{1}{2}$ in	$\frac{3}{4}$ in
2.5	0	$\frac{1}{4}$ in	$\frac{1}{2}$ in	$\frac{3}{4}$ in
2 *	0	-	-	-

Table 6.2 Fibre Geometry and Discontinuity

For m = 2 i.e. the case where fibres lie in continuous line contact with each other, one model was obtained. The discontinuity in the central fibre was achieved by screwing the upper portion of the central rod into a bar made of Araldite which had been accurately drilled to be supported by the two extreme rods in a straight line as shown in Figure 6.1. The use of Araldite as support for both the base and the upper rods was necessary so that relative movement of the matrix would not take place; this would otherwise change the true stress distribution due to the presence of the rods alone.

(vi) Cutting the Slices

In the case of the models cast around glass rods, transverse slices were cut using a large diameter diamond wheel cutter at high speed (24,000 RPM) and very slow feed, the model and wheel being profusely supplied with liquid coolant.

---

*No useful information was obtained for this.

Three different available workshop machines were considered for slicing the Aluminium/Araldite model which couldnot be cut on the diamond wheel since the rather soft aluminium would tend to clog the diamond wheel and damage it. These were (i) a milling machine, (ii) a band saw and (iii) a power saw. Trial cuts were made with these machines to evaluate their suitability.

a) Milling Machine This is a horizontal milling machine with a wheel cutter. Whilst this produced excellent surface finish, it was found to exert too much force on the specimen during cutting. Also the size of the specimen was too large to enable a complete cut to be made through the model in one traverse of the machine bed. The cuts therefore had to be taken in bits requiring the model to be turned round with possible consequent mal-alignment. This procedure of cutting proved to be rather slow and cumbersome and repeatedly gave broken bonds due to the excessive force of the machine.

b) Band Saw This proved to be the quickest way of cutting the slices. However the saw bench had no feeding or clamping mechanism and these had to be done by hand. Added to this, the continuous movement of the saw and its small thickness produced excessive heat by friction which was not easy to eliminate even by prodigious supply of coolant which again had to be done manually. Surface finish was poor and this method proved most unsuited to the work.

c) Power Saw

The power saw has a rigid hacksaw blade of dimensions 14 in. x 2 in. x 0.10 in. x 10 t.p.i.; it also has an adjustable dashpot mechanism which controls the depth of cut per stroke and hence the pressure exerted on the specimen. It has facilities for clamping the model and an automatic coolant supply system. By setting the dial on the dashpot to give minimum pressure, this machine proved to be the best suited to the work; the finish was fairly good.

One specimen was cast without any inclusions and sliced up on the machine. On examination the slices were found to show negligible birefringence. This was proof that (i) the cutting process did not introduce any extraneous stresses into the slices and (ii) the residual stresses from the restrained shrinkage (i.e. with the aluminium inclusions) were practically all due to differential shrinkage.

(vii) Polishing of Slices

Initially it was decided to improve the finish of the cut slices by fly-cutting both faces. There was difficulty, however, in getting them uniformly clamped on the machine bed and the slightest flutter of the specimen produced non-uniform cutting. Otherwise the finish obtained in this manner was excellent. In the end, careful polishing with sandpaper by hand proved to be a quick and satisfactory method.

(viii) Slicing Planes

For each model geometry slices were cut as follows:

a) SLICE I - a transverse slice from the mid-section of the model,

b) SLICE II - a meridional slice through the centre of three rods in a straight line,

c) SLICE III - a meridional slice through the central rod and at 90° to SLICE II,

d) SLICE IV - a meridional slice through any two adjacent rods surrounding the central rod.

Figure 6.2 shows the various planes in which the above slices are located in the model. The thickness of the slices was about 0.1 in. Figures 6.3a - 3j show typical isochromatic patterns associated with the different slices.

(ix) Check for Infinite Fibre Array Simulation

The seven-rod arrangement in the models is supposed to yield the same stress distribution around the central fibre as for an infinite hexagonal array of these fibres in an Araldite matrix. To check the validity of this, one model with m = 3 with nineteen rods was cast. Figure 6.4b shows the isochromatics in a transverse section, SLICE I, which are practically of the same form and distribution as those from the seven-rod model, figure 6.4a.

(x) Recording of Photoelastic Data

Frozen stress tests on Araldite (65) have shown that the level of the frozen stress isochromatics slightly decreases from the value immediately after freezing, over a period of time. However, the initial value is found to be attained again after a further period of time. In most conventional three-dimensional photoelastic work, therefore, the practice

is to wait for the stabilisation of the fringes before recording them. However, in the present tests, the presence of elastic stresses in the models would give rise to stress relaxations and hence irretrievable loss of fringes with the passage of time. Figure 6.3f shows the isochromatics for m = 3 ($\delta = \frac{3}{4}$ in. immediately after cutting the slice. The isochromatics from the same slice recorded after six months' storage at room temperature, are shown in figure 6.5 and there is a reduction in the level of fringes.

The procedure adopted, therefore, was to carry out the various stages of the tests from the casting stage to the photographic recording of data, in rapid succession. A sodium monochromatic light source was used to record the isochromatics and a white light source for the isoclinics. By a suitable combination of lenses, magnifications of up to 4 were obtained and accuracy of data improved considerably.

6.3 CALIBRATION TESTS

Having obtained the isochromatics, we now have to investigate their nature and assign meaningful stress values to them. In conventional two- or three-dimensional analysis this is a simple matter. However, in the present case, since the fringes developed gradually over a temperature range from around the critical, various tests have to be carried out to evaluate the effective fringe constant for the models.

(i) Elastic and Frozen Fringes

To determine the nature of the isochromatics in the specimens, the metal component of the slices from both transverse

and meridional planes (SLICES I and II) were carefully removed and the resulting isochromatics examined. Figures 6.6a - 6b show the fringes from such slices; figures 6.7a - 7b show plots of the total fringes and residual fringes along particular lines. These show that:

(i) both the released and residual fringe patterns are of the same form throughout the material, and

(ii) they occur in approximately equal numbers.

The problem of calibration therefore resolves itself into the determination of the relationship between fringe order and strain for that part of the composite isochromatic fringe system which is released when the constraints are broken and that part which remains, bearing in mind that creep might occur in the experiments.

(ii) Dog-bone Tests

Tests were performed on a dog-bone specimen , Figure 6.8, of the form recommended by Sampson (66). In these tests, specimens were cast in an aluminium mould and subjected to the same curing and cooling cycle as the models. Adhesion was obtained at all points except along the shank of the specimen where the two side pieces were treated with release agent and removed before the specimen and its mould were cooled in the oven at the same rate as the models. By suitable arrangement of a polariscope and camera the isochromatic in the dog-bone specimen were photographed at various temperatures during cooling, Figure 6.9.

The fringe order in the shank obtained from separate tests is plotted against temperature in Figure 6.10. The results are clearly reproducible and yielded a single straight line and therefore one calibration constant for the temperature range.

The bonds at the ends of the dog bone specimens were broken at intervals from 0-5 days after cooling to room temperature. All the specimens were free of isochromatics, Figure 6.11a-11b, showing that the residual shrinkage stress was purely elastic.

Allowing for both differential thermal effects and the elasticity of the sides of the mould, an expression for the rate of appearance of fringes with temperature can easily be obtained as follows:

The strain e_{S1} in the shank of the dog bone due to the free differential contraction of the shank and the ends of the mould is:

$$e_{S1} = (\alpha_f - \alpha_m)T \quad \ldots\ldots\ldots \qquad (6.1)$$

where α_f and α_m are the thermal coefficients of linear expansion of the aluminium and araldite respectively and T the temperature.

Considering the constraint of the sides of the mould, if e_{ST} is the total strain in the shank and e_{S2} the strain in the sides, then for equilibrium,

$$e_{S2}E_fA_f = e_{ST}A_mE_m \quad \ldots\ldots\ldots \qquad (6.2)$$

where A_f, A_m are the total cross-sectional areas of the sides of mould and shank respectively and E_f, E_m, the respective Young's Modulii.

From equation (6.2):

$$e_{S2} = \frac{A_m E_m}{E_f A_f} \cdot e_{ST}$$

Also

$$e_{ST} = e_{S1} + e_{S2}$$

$$= (\alpha_f - \alpha_m)T + \frac{A_m E_m}{A_f E_f} \cdot e_{ST}$$

$$= (\alpha_f - \alpha_m)T / (1 - \frac{E_m}{E_f} \cdot \frac{A_m}{A_f}) \quad \ldots\ldots\ldots \quad (6.3)$$

The stress σ_S in the shank is given by,

$$\sigma_S = E_m e_{ST} = NF$$

where N is the number of fringes in the shank and F the material elastic fringe value of the Araldite.

Hence

$$NF = \frac{E_m(\alpha_f - \alpha_m)T}{(1 - \frac{E_m}{E_f} \cdot \frac{A_m}{A_f})} \quad \ldots\ldots\ldots \quad (6.4)$$

Substituting the appropriate values from Table 6.1 into equation (6.4), we obtain:

$$\frac{dN}{dT} = \frac{(0.46 \times 10^{6}) \times (24-63) \times 10^{-6}}{55.5(1 - \frac{0.46}{10} \times \frac{0.125}{.5}}$$

$$= -0.31$$

This value compares with that obtained from Figure 6.10 i.e.-0.306. It is clear therefore, that the usual photoelastic constants are directly applicable to the elastic part of the shrinkage process.

6.4 Creep Tests

To determine the nature of the frozeh finges, a series of short-time creep tests were carried out on tensile specimens at various temperatures up to the critical, 120°C. Lines were scribed on the specimens and any permanent strains measured on a projection microscope to an accuracy of ± 0.00001 in. The time for the duration of the creep tests at each temperature was two hours, the same as the cooling rate in the models.

Except at temperatures greater than about 100°C no permanent fringes or strains were obtained. Tests above 100°C gave the normal frozen stress fringe value of 1.438 p.s.i./fringe/in.

With the two calibration values established, it is possible to separate the elastic from the frozen stress systems and analyse each separately. The complete separation of the stresses will be the subject of the next chapter.

CHAPTER 7

ANALYSIS OF EXPERIMENTAL DATA

7.1 INTRODUCTION

Generally, the optical data as recorded, by themselves, do not directly give the separate stresses. This is because different states of stress with different principal magnitudes but all differing by an arbitrary isotropic system, produce equal photoelastic effects.

On free boundaries, however, since the direct stress in the direction of the normal to the surface is known to be zero, the magnitude and direction of the boundary stress lying in a plane parallel to the tangent plane at a point in the surface, is directly given by the value of the fringe order and isoclinic respectively for normal incidence in the plane.

In separating the stresses in two-dimenionsal photoelastic models, a number of methods may be resorted to. These methods, are in the main:

(i) Mechanical methods, e.g. lateral extension and grid measurements yielding values of strain in the surface of the plate,

(ii) A relaxation numerical method based on the Laplace Equation $(\frac{\partial^2}{\partial x^2} + \frac{\partial^2}{\partial y^2})(\sigma_1 + \sigma_2) = 0$, for generalised plane stress conditions,

(iii) The oblique incidence method devised by Drucker (67),

(iv) Interferometric methods for determining isophaics i.e. locus of points having the same principal stress sum $(\sigma_1 + \sigma_2)$,

(v) Step by step integration methods, e.g. the shear difference method and the method based on the Lamé-Maxwell Equilibrium Equations.

Details of these methods may be found in standard texts on photoelasticity, e.g. references (44), (51), (67). Of the above methods only (v), i.e. the integration method is applicable to the separation of stresses in three dimensions from frozen stress models. Essentially this is an extension of the governing equilibrium equations in three-dimensions. Thus, in general, in order to separate the three principal stresses, P, Q, R, from photoelastic data at a point in the body, two orthogonal planes containing the point would be required. When the body contains planes of symmetry the procedure for obtaining the required data becomes simpler.

7.2 PLANES OF SYMMETRY

The normal to a plane of symmetry at any point in the plane is a principal axis at the point. Hence a slice cut from any such plane would give the principal stress differences (P-Q) say, and their directions at any point in the plane. The other principal stress difference (P-R) say, at any point may be found by cutting a slice orthogonal to the first and whose mid-plane passes through the point. To do this for several points in the plane would entail a lot of labour. To avoid this, the method of oblique incidence may be employed using the first slice alone, e.g. see reference (68).

7.3 EXTENSION OF LAMÉ-MAXWELL EQUATIONS IN THREE-DIMENSIONS

Equations of equilibrium at a point, of the Lame-Maxwell type, have been formulated in three-dimensions (69). In general, none of the three lines of principal stress passing through any point is a plane curve and the application of these equations to a step-by-step integration procedure is impracticable since this would involve the determination of principal stress directions for several points lying in different planes.

However, for a plane of symmetry, it is known that a line of principal stress is a plane curve and from equilibrium considerations, the differential equation can be derived as:

$$\frac{\partial P}{\partial S} + \frac{P-Q}{\rho_2} + \frac{R-P}{\rho_3} \cdot \text{Cos } \alpha = 0 \quad \ldots\ldots\ldots \qquad (7.1)$$

dS is the increment of length along the P line of stress ρ_1, ρ_2, ρ_3 the radii of curvature of the P-, Q-, and R- stress trajectories at the point and α is generally the inclination of ρ_3 to the P-stress trajectory, as shown in Figure 7.1.

The two systems which permit an easy evaluation of these parameters are:

(i) the case of an axisymmetric stress distribution. In this case, the R-stress trajectories are circles with their centres on the axis of symmetry; any plane which contains the axis of symmetry is also a plane of symmetry.

(ii) The case where the P-stress trajectory is the intersection of two planes of symmetry. Here α is zero at all points and equation (7.1) reduces to:

$$\frac{\partial P}{\partial S} + \frac{P-Q}{\rho_2} + \frac{R-P}{\rho_3} = 0 \quad \ldots\ldots\ldots \qquad (7.2)$$

7.4 SHEAR DIFFERENCE METHOD

The shear difference method in two-dimensional analysis, has also been extended to three-dimensional problems (70). This method is general and may be used to determine the six components of stress along any line in an arbitarily loaded body.

Using the stress system shown in Figure 7.2a and neglecting body forces, the equilibrium equation in the X-direction is:

$$\frac{\partial \sigma_x}{\partial x} + \frac{\partial \tau_{xy}}{\partial y} + \frac{\partial \tau_{zx}}{\partial z} = 0 \quad \ldots\ldots\ldots \qquad (7.3)$$

In figures 7.2b-2c an arbitarily chosen line in the solid body has been aligned with the x-axis. Upon integration of equation (7.3), the stress at any point k is given by:

$$\sigma_{x(K)} = \sigma_{x(A)} - \int_A^K \frac{\partial \tau_{yx}}{\partial y}\, dx - \int_A^J \frac{\partial \tau_{zx}}{\partial z}\, dx \quad \ldots\ldots\ldots (7.4)$$

where $\sigma_{x(A)}$ is the stress at an initial point A which would in most cases coincide with the boundary where at least one stress would be completely known. $\frac{\partial \tau_{yx}}{\partial y}$ and $\frac{\partial \tau_{zx}}{\partial z}$ may be

determined in the same manner as in two-dimensional problems, e.g. reference (50), from the two slices containing the line of integration from the XZ and XY planes respectively.

Replacing the integrals by summations, equation (7.4) becomes:

$$\sigma_{x(K)} = \sigma_{x(A)} - \sum_{A}^{K} \frac{\Delta \tau_{yx}}{\Delta y} \Delta x - \sum_{A}^{K} \frac{\Delta \tau_{zx}}{\Delta z} \Delta x \quad \ldots\ldots\ldots \qquad (7.5)$$

The summations can be evaluated graphically. From Mohr's Circle or other considerations,

$$(\sigma_x - \sigma_y)_K = [(p-q)_K (\text{Cos } 2\emptyset)_K]_{xy} = F[\eta_K (\text{Cos } 2\emptyset)_K]_{xy}$$

$$(\sigma_x - \sigma_z)_K = [(p-q)_K (\text{Cos } 2\emptyset)_K]_{xz} = F[\eta_K (\text{Cos } 2\emptyset)_K]_{xz} \quad \ldots\ldots (7.6)$$

where xy and xz denote values obtained from the XY and XZ planes respectively, $\emptyset$, the isoclinic parameter, F the model fringe value and η the fringe order, all measurements referring to the point K.

Having thus obtained the five stress components, namely σ_x, σ_y, σ_z, τ_{xy}, τ_{xz}, the last component, τ_{yz}, may be obtained by the method of oblique incidence from either slice. For details of the application of the oblique incidence method, see for example, reference (68). It may be mentioned that this method is subject to serious inaccuracies for regions of high shear stress gradients.

7.5 ANALYSIS OF PHOTOELASTIC DATA

The three-dimensional methods of stress separation outlined above, are applicable only to frozen stress models in which the fringe pattern in the body is unaltered on cutting out the slices. In our present models, however, there are both frozen and elastic fringes in the slices. The number of elastic fringes within the model changes slightly upon cutting the slices due to the relief of the stresses in the orthogonal direction to the plane of the slice.

Tests as conducted in the previous chapter, showed that the residual elastic fringe distribution has the same form as the frozen fringes in the slices. Thus by analysing the frozen stress fringes separately, and knowing the boundary conditions in the various planes of the slices for both the elastic and frozen fringes, we can evaluate a correction factor for the elastic portion of the isochromatic fringe system to obtain the true distribution in the model. We shall proceed to show how this was achieved.

(i) Continuous Rods

The numerical effort involved in general three-dimensional separation of stresses was reduced in the present work since the hexagonal arrangement of the rods allowed for the existence of several planes of symmetry. The isochromatics associated with the various slices are shown in Figure 6.3; the isoclinics and stress trajectories are shown in Figures 7.3a-3e. The lines of interest are HJ and DB (Figure 7.3a, 3b), HJ is the intersection of the planes of SLICES II and IV and DB that

of the planes of SLICES I and II. HJ and DB are stress trajectories and they coincide with isoclinic parameters.

(ii) Boundary Stresses (Initial Conditions)

Since the model was not subjected to any constraints on its boundary, the normal component of stress everywhere on the boundary is zero. In the transverse slice, SLICE I, the outermost dark fringe at the edge of the disc represents an isotropic* region. Hence if Q, R, is the stress system in this slice, R = Q = 0 around the edge. This region extends up to the point M, Figure 7.3a.

On the top and bottom edges of the meridional slice, SLICE II, since the axial stress P is zero, the fringe orders at these edges give directly the values of the Q-stress.

(iii) Integration in Transverse Plane

Starting from the point M in the transverse plane, SLICE I, Figure 7.3a, the integration was carried out in stages along MA, AD and DB as follows:

a) Analysis Along MA

MA is the intersection of the two planes of symmetry, - i.e. SLICES I and III. The stress trajectories for SLICE III, were found to be straight lines except in a small region close to the ends of the rods. This state of affairs also applies to SLICE IV and is due to plane strain conditions. Hence

---

*an isotropic point or region is a region of zero order of fringe and is characterised by a constant dark field (in white light) during the plotting of isoclinics; all the isoclinic parameters pass through this point or region.

along MA the Lame-Maxwell equation i.e. equation (7.2) reduces to:

$$\frac{\partial Q}{\partial s} + \frac{Q-R}{\rho_1} = 0$$

since ρ_2 is ∞. Q-R and ρ_1 can be obtained from SLICE I only and the procedure effectively reduces to a two-dimensional type of analysis.

b) Analysis along AD (Figure 7.3a)

The integration here is similar to that along MA requiring only the transverse slice. The initial conditions are the values obtained at A previously.

It may be observed that in the transverse slice, since the axial elastic stress P has been released by cutting, the elastic residual stress system Q_e and R_e approximate to a plane stress system. Similar plane stress conditions can be said to exist at the bottom and top edges of the model where the axial component of stress is zero. Indeed in the vicinity of H, Figure 7.3b, the stress trajectories are straight lines indicating that this state of plane stress extends over a finite thickness. However, due to the release of the R-stress in SLICE II, the value of the elastic stress given by the apparent fringe order would differ from the true plane stress elastic fringe order at H as obtained from the analysis in the transverse plane.

c) Correction for Elastic Fringes

The frozen fringes have been shown previously to have

the same form of distribution as the residual elastic fringes, see Figures 6.7a-7b; they also represent the elastic stress distribution in the model. Thus if f_e is the true elastic fringe order and f_f* the frozen fringe order at a point in the model, then $f_e = cf_f$; where c is a constant factor. At H

$$f_e = f'_{e(D)}$$

where $f'_{e(D)}$ is the residual elastic fringe order at D in the transverse plane corresponding to the stress in direction DB, i.e. the Q-stress.

Hence, $$c = \frac{f'_{e(D)}}{f_{f(H)}}$$

and $$f_e = \frac{f'_{e(D)}}{f_{f(H)}} \times f_f$$

$$= \frac{f'_{e(D)}}{f_{f(H)}} \times \frac{f_T}{2}$$

where f_T is the total number of apparent fringes at the point since $f_f = f_{T/2}$.

Having determined the correction factor for the elastic fringes, the integration is next switched into SLICE II along HJ and JX, Figure 7.3b.

---

*f_f is always the true frozen fringe order in both slice and model.

(d) Analysis along HJ

Using the correction factor for the elastic fringes, the integration is carried out along HJ using the Lame-Maxwell equation and noting that $1/\rho_2 = 0$ from SLICE IV. The equation here reduces to:

$$\frac{\partial P}{\partial S} + \frac{P-Q}{\rho_1} = 0 .$$

Q is known at H. From the stress trajectories and isochromatic patterns it can be seen that the P- and Q-stress attain terminal constant values in regions away from the edge indicating plane strain conditions.

(e) Analysis along DB

Again after correcting the elastic fringes as described above the integration is conducted along DB in the transverse slice, Figure 7.3a, using as the initial value, the Q-stress at H obtained previously. The relevant equation in this case is:

$$\frac{\partial Q}{\partial S} + \frac{Q-R}{\rho_1} = 0$$

where ρ_1 is measured from the transverse slice; $1/\rho_2 = 0$ from the meridional SLICE II.

(ii) Analysis of Discontinuous Rods

(a) Isochromatic Patterns

Figures 6.3a-3j show typical isochromatic patterns for various fibre spacings and discontinuity from different planes

within the model. The following observations may be made about the fringe patterns:

(i) In SLICE II, Figures 6.3e-3f, the fringes show the same mode and level of distribution as for the continuous fibre in regions removed from those containing the discontinuity since the middle rod is long enough to establish plane strain conditions (parallel isochromatics) some way up its length.

(ii) The position of the two isotropic points in SLICE II are reversed depending on the length of the discontinuity and the packing factor m. These points lie either on the transverse line of symmetry or on the central axis, Figures 6.3e-3f. For most of the models the two points lay on the transverse line of symmetry.

(iii) The slices from the mid-transverse plane show (Fig.6 isotropic regions which increase in area with increasing length of discontinuity. This region approximates/as assumed to a condition of rotational symmetry in the proposed numerical computational model earlier.

For the purposes of the analysis, the main interest was the stress distribution in the discontinuity along the two lines of symmetry ox' and o'z', Figure 7.4

(b) Isoclinics and Isostatics

Figure 7.3c-3d show typical isoclinics and isostatics in SLICE II for discontinuous fibres. Notice that the set of stress trajectories does not change as we pass through the isotropic point.

From the observations made about the fringe pattern, the same fringe correction factor was adopted as for the respective cases of the continuous rods and the analysis conducted systematically starting from the edge E along EL, Figure 7.3c.

(c) Analysis along EL

Using the corrected fringe orders the integration was carried out as in the case of the continuous rods, by either the Lamé-Maxwell equations or the shear difference method, depending on the nature of the stress trajectory along EL. For example, in Figure 7.3d (m=3, $\delta=\frac{3}{4}$ in.), EL does not remain coincident with a stress [illegible] trajectory along the whole length and the shear difference method was adopted.

(d) Analysis along LK (Figure 7.3c)

Having arrived at the point L the analysis was switched over along OLK using data from both the transverse and the meridional slice (SLICE II). OLK is coincident with the zero isoclinic for all the models and hence the Lamé-Maxwell equations were adopted for analysis.

(e) Analysis along KG (Figure 7.3c)

Using data from SLICES II and III the analysis was performed along KG which was also coincident with the zero isoclinic.

7.6 ACCURACY

In all the models except those for m = 2.5, very clear and sharp isoclinics were obtained. In the case of the models for m = 2.5, cracks persistently appeared at the tips of the rods in the discontinuity. On examination of the solid model, the crack was found to extend around the circumference of the rod in the form of a cone within the gap. Both the isochromatics and isoclinics were therefore distorted and no accurate data could be obtained from them, figure 6.3g.

The main source of inaccuracies was in the measurement of radii of curvatures of the stress trajectories. This is to be expected in any photoelastic work.

7.7 RESULTS

(i) Continuous Fibres

Figure 7.5 shows the distribution of computed radial stresses in the transverse section of the matrix along the two lines of symmetry; the separated radial stresses from the photoelastic analysis along the line OX in Figure 3.2 are shown as points for comparison. The computed and experimental values have been assumed equal at the interface, (x/X) = 1.0. The variation of one distribution from the other is within the limits of experimental and analytical error throughout the range.

(ii) Discontinuous Fibres

Referring to Figure 7.4, the three stress components P, Q, and R are shown plotted in Figures 7.6-7.7, for the

two packing factors m = 3 and m = 4.5 and for δ/ρ = 1, 2 and 3.

(a) Stresses along ox' (Figure 7.4)

The axial stresses Px, all start with tension at the interface 0 at the inside of one of the outer fibres and change to compression which increases up to a maximum at the centre of the gap (x'/X') = 1, Figure 7.6a. For each value of m the stresses at the interface (x'/X' = 0) are the same for all gaps and as the discontinuity decreases the stresses increase and the point along ox' at which the change to compression occurs moves towards the interface. As the fibre spacing increases, the axial tensile stresses extend over a wider region.

The circumferential stresses Rx' behave in a similar manner to the axial stresses Px' starting with tension of approximately the same magnitude at the interface and changing to compression, Figure 7.6b-6c. However the corresponding points of change along ox' occur at shorter distances from 0. The radial stresses Qx' have their maximum compressive values at the interface and decrease to a uniform compressive value about midway along ox'; from this point onwards, the radial and circumferential stresses have equal uniform values as shown by the isotropic regions in the photoelastic slices from the transverse section, e.g. figure 6.3b.

(b) Stresses along o'z' (Figure 7.4)

The axial stress distributions on o'z', Pz', are shown in Figure 7.7a. These are all compressive and almost uniform, the magnitude of the stresses increasing as the

fibres become closely spaced and as the discontinuity decreases. As would be expected, both the radial and circumferential stresses on o'z' have the same values for the same fibre geometry indicating conditions of axial symmetry, Figure 7.7b.

(iii) Shear Stress (τ) along Discontinuous Fibre (Figure 7.4)

Starting from the tip of the discontinuity, the shear stresse (τ) along the discontinuous fibre have been plotted in figures 7.8a-8b for both packing factors and for each discontinuity. The shear stresses are high at the tip and fall to zero a few fibre-widths along the fibre. The smaller the fibre spacing and discontinuity the larger the shear stresses, and the longer the distance along the fibre over which they fall to zero for a particular fibre spacing.

7.8 COMPARISON WITH PLANE MODEL

The results obtained for the experimental model clearly prove the validity of the objections raised about the plane model. At this point doubts may be raised about the usefulness of plane model in other work related to composite studies previously mentioned. It should be remembered that the shrinkage system is an internally self-equilibrating system requiring a precise simulation of the shrinkage process. In the other types of work where external loads are specified, the internal mode of constraints are automatically satisfied to a good approximation of the real system in accordance with the St. Venant's principle, as long as the E_f/E_m ratio is sufficiently large.

D I S C U S S I O N

1. EXPERIMENTAL TECHNIQUES

The photothermoelastic technique of stress analysis is being extensively employed in a variety of thermal shrinkage problems. Two distinct applications have emerged:

(i) A comparative study of shrinkage stresses in bonded structures to evaluate the best design shape of the structure (55) (62) (71) (50). In this, a suitable calibration factor may be derived, based for instance, on the known value of the strain at a region removed from the bonded interface and the associated fringe number for the material. Fringe concentration factors can thus be measured for different geometrical configurations to obtain the shape which gives the least stress concentration.

(ii) The second approach is to obtain a satisfactory calibration of the fringes in terms of stress to be used subsequently in determining the absolute magnitudes of the separate stresses in either a two- or three-dimensional bonded structure. The main difficulty in this, is in the calibration procedure and the relief of stresses when slices are cut from three-dimensional models as mentioned in an earlier chapter.

(a) Calibration Procedure

Sampson (66) has suggested a method of calibrating the fringes from the dog-bone tests also employed in the present work. In this method a factor 'C' was introduced into equation (6.4) to account for the lack of perfect restraint in the dog-bone system (and indeed for any other shrinkage system) thus:

$$\frac{dN}{dT} = \frac{CE_m(\alpha_f - \alpha_m)}{F\left(1 - \frac{E_m}{E_f} \cdot \frac{A_m}{A_f}\right)} * \quad \ldots\ldots\ldots \quad (D.1)$$

Using this factor, a dimensionless stress system expressed as

$$\frac{P-q}{E\Delta} = \frac{C,N}{\overline{N}}$$

was proposed to be used in the interpretation of the fringes in a restrained shrinkage model. In this expression, P-q is the stress difference at a point, E, the Young's Modulus, N the fringe order in the model, $\overline{N}$ the fringe order in the shank of the dog-bone and Δ the free thermal differential contraction strain.

In subsequently applying this dimensionless form of the principal stress difference to a three-dimensional model, Sampson failed to account for the stresses relieved due to the slicing although as has been presently revealed, their effect is not negligible. In evaluating the constant C, Sampson used the frozen stress constants of the material since on removing the specimen from its mould, it became apparent that the source of the fringes was predominantly of the frozen type. Further, the sue of this coefficient as suggested, contradicts a previous stipulation that the model (in this case the dog-bone specimen) and prototype must be geometrically similar, since otherwise the value of C would be different in another system of restraint. Such a coefficient is therefore valueless and provided the nature

---

*In his derivation, Sampson neglected the effect of the restraint of the sides of the mould. His expression was: $\frac{dN}{dT} = \frac{CE_m(\alpha f - \alpha_m)}{F}$

of the fringes in a dog-bone has been determined, the fringe orders found for any other similar elastic system must apply.

Note that in the present investigation, the dog-bone tests were conducted to ascertain the nature of the fringes resulting from the differential thermal shrinkage in the material used for the photoelastic analysis. By substituting the elastic constants into the expression equation (6.4), the value of dN/dT was the same as the experimentally measured value. Hence it was concluded that the elastic fringes in the subsequent analysis of the model must be assigned the same stress value as that obtained from a conventional elastic calibration test. Further, the creep tests established both the constancy of the properties over the temperature range, and the nature of the frozen-in fringes.

(b) Viscoelastic Effects

Data on the temperature and strain-rate dependence of the properties of Araldite are not available. It is however known that a complex relationship exists between the mechanical and optical responses and the time-temperature-load history of polymeric materials at temperatures below the critical in a manner as previously described in an early chapter.

The question may be raised as to why the photoelastic data in the slices were not recorded after the elastic fringes had stabilised. The dog-bone calibration tests had established beyond doubt that the elastic part of the fringes in the model was wholly attributable to elastic effects and since the problem was essentially one of residual stress measurement in

an absolute sense, the instantaneous elastic modulus was the most significant property. Also in the finite element method viscoelastic effects of the plastic were not taken into account, the matrix material (for the ARL systems) being considered as perfectly Hookean over the whole temperature range. Furthermore, the dissimilarity in elastic properties and elastic behaviour of the component materials, in particular the Poisson's ratios, would not make for accurate comparison between photelastic results recorded after delayed elastic response, and the numerical results. To minimise any changes with time all slices were cut and the photoelastic data obtained from them as soon as the casting, curing and cooling cycle was complete.

(c) Plane Strain Model

The choice of plane strain models for the experimental investigation was (i) to eliminate the effect of 'pinching' and (ii) to enable the method to be extended to the study of stresses near discontinuities once it was established for continuous fibres. 'Pinching' is the shrinkage effect in the direction perpendicular to the plane of the plate (plane stress model) at the interface thus creating a three-dimensional state of stress, see for example reference (55). The effect is that the photoelastic patterns exhibit slightly less fringes near the interface than if the whole field were truly two-dimensional.

In elasticity problems if certain conditions are satisfied, all the in-plane stresses are the same for the same boundary

conditions in both plane stress and plane strain. These conditions are (72):

(i) the problem must be linear,

(ii) loads must be specified in terms of boundary stresses (first boundary value problem) and,

(iii) the body is simply connected, or a multiply-connected body with the loads on each closed portion of the boundary in equilibrium.

The shrinkage problem, however, does not satisfy condition (ii) since it is a mixed boundary value problem, i.e. the restraints at the bonded boundaries are given in terms of displacements. To obtain an exact correspondence of the plane stress and plane strain solutions, the elastic constants must be modified. This is done by a simultaneous solution of two modified forms of the general expression of Hooke's law (75). Clearly in all practical unidirectional fibre composite materials, the conditions away from the boundaries will be those of plane strain so that the models chosen for this analysis should provide data which correspond to the actual conditions.

(d) Accuracy

Within the limits of experimental error, and, in particular errors associated with the graphical integration in the photo-elastic separation of the stresses, there is good agreement between the stress distributions obtained by the two methods for continuous fibres, Figure 7.5. It has been previously established that in the restrained shrinkage method the total fringe order in the model represents the elastic stress

distribution and the fringes remaining in the slices after the load is broken and the fibres are removed, are wholly attributable to the deformations imposed on the primary bond structure of the resin (57), (66). These frozen fringes are fully representative (as in any other photoelasticity work using frozen stress techniques) of the elastic stress distribution in the composite so that the sum of the two sets of fringes (elastic and frozen) also represents a purely elastic stress distribution in the composite. Because of this, the comparison of the photelastic results with the purely elastic solution given by the finite element method, is justified even though the properties of the ARALDITE matrix do not remain constant over the range of temperature drop considered. The corresponding temperature drop for computation assuming purely elastic conditions which is chosen to apply in the numerical procedure would be different from the 90°C used in the experiments because the experimental shrinkage system comprises both elastic and frozen stress behaviour. It was found that this temperature drop was about 50°C.

2. RESULTS

(i) Matrix Stresses and Elastic Properties

It is evident from the results of the finite element analyses for continuous fibres in Chapter 3 that the shrinkage stresses resulting from a temperature change in a composite material can be large. For a given random set of composite systems, the most significant factor which determines the

magnitude of the matrix shrinkage stresses is the value of its Young's Modulus; high matrix values of Young's Modulus produce correspondingly high stresses, whilst the Young's Modulus of the fibre is not significant. However, for a given matrix material, the stresses were found to be directly proportional to the following parameters:

(i) the difference between the coefficients of thermal expansion of fibre and matrix, $(\alpha_m - \alpha_f)$;

(ii) the ratio of the coefficients of thermal expansion, α_m/α_f and

(iii) the difference between the Young's Modulii of matrix and fibre, $(E_f - E_m)$.

No dependence on the ratio E_t/E_m was found.

(ii) Tensile Stresses in Matrix

The results also show that in most composite materials, there exists a mixture of tensile and compressive stresses in the principal directions, as a result of a temperature change. The state of the stress depends on the fibre density. For most fibre spacings the radial stresses are mainly compressive except for very dense packing of the fibres when tensile stresses occur in the centre of the tricorn, Figure 1.2.

The development of tensile stresses within the matrix has been explained in Chapter 1 (q.v.), using an 'interference' model, and the results prove the validity of the shrinkage mechanism as postulated. With decreasing fibre spacing tensile stresses are established to maintain the adhesion between matrix and fibre. The less stiff the matrix material the greater the

tendency for tensile stresses to develop. It is clear from the interference model that this is a factor of the difference between the shrinkage coefficients ($\Delta\alpha$), the greater the value of $\Delta\alpha$ the greater the tendency for the interference gaps to appear as in Figure 1.2a. Thus the Araldite composite systems ($\Delta\alpha \sim 50 \times 10^{-6}/^{o}C$) showed tensile stresses in the tricorn for m = 2, 2·08 and 2·125 whilst the rest of the systems ($\Delta\alpha \sim 12 \times 10^{-6}/^{o}C$) gave tension only for the one case of maximum fibre density, namely m = 2.

(iii) Radial Compression in Matrix

For all fibre spacings, the radial stresses remain compressive along a line joining the centres of any two adjacent fibres and the stresses increase, the closer the fibres are packed. The variation of the radial stresses at the interface B, (and at any point on ox in Figure 3.2) with fibre spacing is shown in Figure 3.6a. For all composite systems, the compressive radial stress increases sharply from its value at m = 2 to a maximum at m = 2.25; thereafter it decreases gradually to an asymptotic value corresponding to the single fibre analysis.

Measured round the interface, the radial stresses remain nearly constant for widely spaced fibres when they approximate to the case of a single fibre, but they change from compressive to tensile for closely packed fibres. Assuming symmetrical packing the change is cyclic, occurring six times for a hexagonal packing and four times for a square arrangement. The tangential stresses were found to be positive along the interface and beyond into a larger part of the matrix for all fibre spacings as postulated even though the radial stresses change

along the same path. The radial and tangential stresses at A, (Figure 3.2) were found to be approximately equal in magnitude and had the same sense since A is an isotropic point.

(iv) Fibre Stresses

The fibres were found approximately to be in a state of uniform biaxial compression for most spacings except those small enough to produce radial tensile stresses within the matrix up to the interface. In the latter case, depending on the spacing, the fibre stresses became tensile in the appropriate regions as shown in Figures 3.8a-8b. Figure D.2 shows the isochromatic patterns in a slice from the transverse section of a Glass/Araldite model; it shows a uniform isochromatic field in the glass, thus confirming the numerical results from the finite element analysis. Further, examination of the computed results showed that along any radial line, the radial stresses vary continuously throughout matrix and fibre whilst a sharp discontinuity at the interface occured in the tangential stresses. This is because at the interface radial stresses must be the same for equilibrium whilst in the tangential direction compatibility conditions require equality of strains.

(v) Discontinuous Fibres

For the reasons of computer-model inadequacy already discussed in Chapter 4 and from the consequent discrepancies in results from the numerical and photoelastic analyses of the shrinkage stresses around discontinuities, attention here will be confined mainly to the results from the photoelastic work.

These results are the more realistic and pertinent to real composite materials.

For the case of continuous fibres embedded in a matrix, the axial stress within the matrix is tensile as explained earlier, and this was found to be the case in the photoelastic analysis. The magnitude of the axial stress increased with decreasing fibre spacing. However in the neighbourhood of a discontinuity, since the fibres are in both radial and axial compression resulting from shrinkage as explained in Chapter 1, the matrix material lying in the gap directly between the ends of the fibres must also be in compression. The matrix material in the gap behaves more and more like a piece of fibre as the gap becomes shorter so that axial stresses in the matrix become more uniform and compressive as those in the fibre.

The axial and tangential stresses at the interface were found to be approximately equal. The length of the discontinuity (δ_o) beyond which the axial stress in the centre of the gap vanishes may be obtained from Figure D.1. For $m = 4.5$ the value of δ_o is about two fibre diameters and for $m = 3$, δ_o is about two and a half fibre diameters.

An isotropic state of stress in the transverse plane in the region around the centre of the discontinuity and lying between the ends of the fibres, was found to exist for both fibre spacings and all the discontinuities. This region is therefore in a state of triaxial compression which eliminates the possibility of crack initiation. The radial and circumferential stresses in the isotropic region attain their minimum

constant values at a certain value of δ; if δ is increased beyond this value, the stresses are unchanged. At this point and beyond, the presence of the gap has no effect on the stress distribution as the fibre end may be regarded as isolated from each other, without any interacting effects.

The magnitude of the shear stress at the tip of the discontinuous fibre (measured along the side), increases with both decreasing fibre spacing and discontinuity. As reported earlier on, persistent cracking of the brittle Araldite matrix occurred when the fibres were packed closely together ($m = 2.5$), Figure 6.3g. In this case the crack developed in a manner as shown in figure D.3 around the sharp tip of the fibre along a line inclined at about 30° - 45° to the horizontal and spreading out into the matrix in the form of a cone. Examination of the isochromatics around the tip of the fibre, Figures 6.3e-3g, shows that the line of maximum shear stress in the matrix, coincides with the line of the crack.

Baker and Cratchley (74) and Ham and Place(75) have performed fatigue tests on silica-reinforced aluminium and tungsten-reinforces copper composites, respectively, and observed the formation of cracks near a fibre end at about $45^{\circ}C$ to the axis of the fibre. Initial shear stresses would aggravate the situation and any fatigue, creep or crack tests on composites should take due cognizance of their presence for a more correct interpretation of results. For instance, in the test by Ham and Place, the forming temperature of the composite was $1100-1200^{\circ}C$, enough to create extremely high shrinkage stresses.

3. EFFECT OF EXTERNALLY APPLIED LOAD

The shrinkage stresses initially established in a composite material as a result of its fabrication method, would influence the behaviour of the composite under a subsequent external loading. If we consider for instance, the effect of a tensile load applied in the axial direction of the fibres, then for continuous fibres and in regions removed from fibre discontinuities, in discontinuous fibres, this would augment the initial axial tensile stresses in the matrix, thus precipitating matrix failure earlier whilst fibre failure would be delayed since the fibres are initially in compression. The compressive strength of the composite as a whole is therefore enhanced.

The existence of residual compressive stresses in discontinuities will improve the composite strength in tension. Tests on discontinuous-fibre tungsten/copper composites have been made by Kelly and Tyson (43) to determine the shear strength (τ) of the matrix at various elevated temperatures. It was found that pull-out experiments on the composites yielded values of τ higher by a factor of two or three than the values of τ calculated from composite strength theory. This was partially attributed to good bonding between fibre and matrix. Again in compression tests on the strength of single glass fibres embedded in a resin matrix, Broutman and McGarry (31) found that the bond strength increased with the cure temperature up to an optimum temperature above which the strength fell. Clearly these findings are inextricably linked with the residual stresses which in turn improve the

bond strength of the composite by offering a radial or axial constraint on the fibres.

The effect of axial load on the transverse radial stress has already been pointed out. The effect of an axial compression for instance is to create radial tension at the interface due to the unequal lateral expansions of fibre and matrix. Initial radial compression would therefore be desirable. However since the fibres take a far greater share of the load it is not likely that the lateral free expansion of the fibres would exceed that of the matrix and thus augment any initial compressive stresses. Thus in a situation where a composite may be subjected to excessive compressive loading, higher fibre volume concentrations would be required to ensure initial radial tensions in the matrix to prevent the incidence of cracks.

One instance in which the presence of residual stresses is desirable is when interfacial delamination occurs before composite failure. Here, radial compression in the matrix would provide a frictional bond necessary for composite strength to be maintained. This is more significant in a non-ductile matrix as in glass/plastic composites and this has been pointed out by Outwater (18). When delamination occurs then the fibre/matrix integrity is determined solely by the frictional restraint at the interface, and this is a direct function of the interfacial radial compression initially existing in the matrix.

GENERAL

In the computer analysis of the various composite systems, perfect adhesion was implicitly assumed. However, in some practical fibre/matrix combinations, the achievement of interfacial coherence presents great difficulties and this has been the subject of several investigations. Coupled with this is the surface degeneration of some fibres at elevated temperatures. However most of the systems studied can be realised in practice, e.g. see ref. (6).

The results from the computer analysis show that for most practical fibre reinforced materials there is likely to be a mixture of both compressive and tensile radial stresses within the matrix due to shrinkage if the composite is formed at a temperature above the ambient. This is also the case if the composite is formed at the ambient temperature and subsequently subjected to a temperature rise, except that the sign of the stresses is reversed. The closer the spacing of the fibres and the softer the matrix material, the larger the area in tension, the tensile region developing first from within the tricorn as postulated and gradually spreading out towards the interface and beyond with decreasing fibre spacing.

The resulting shrinkage may be high enough to generate cracks in brittle materials, or cause interfacial debonding or to plastically deform a ductile matrix. The longitudinal stress may be relieved by the fibres buckling to accommodate the shrinkage (76), and these buckled fibres provide a considerable source of weakness if the composite is to be loaded in compression or bending.

The total stress system in the composite will be the sum of the shrinkage stresses, the stresses from the differences in lateral expansion arising from unequal Poisson's ratios and the applied stresses. Even if the stresses generated by shrinkage cause no direct failure they may provide an initial state of stress which requires only small initial external loads to produce failure. Outwater (77) reports the sounds of resin cracking in filament wound pressure vessels at a pressure barely 15% of the final failures load, due to tensile stresses acting normally to the fibres. By far the greatest number of cracks occur in regions of high fibre density, especially where the fibres are in or nearly in contact.

When the fibres are brittle and the interface strong, fibre cracking may occur. The probable planes of failure deduced from the maximum tensile stresses are shown dotted in figure 6.8a and these form arcs between the compressively loaded contact lines along the fibres. A striking confirmation of this is provided by a photomicrograph of a cross section of glass fibres in an aluminium matrix due to Sutton et al (78); in addition sharp discontinuities in the fibres can cause cracks in the matrix as was found in the tests. The photomicrograph is presented by Sutton et al to show the propagation of cracks through the points of contact, but the source of the cracking and the reasons for the form of crack almost certainly arises from the causes we have discussed here.

It is clear from the results, in particular Figures 6.6a-6b, that both the sign and magnitude of the radial stresses are very sensitive to fibre spacing when the fibres are close together, which is the usual condition required for maximum strength. Where composites are formed by compaction or infiltration of coated fibres it should be possible to optimise the geometry to obtain a maximum strength by a suitable choice of coating thickness in any practical case. This form of fabrication seems to offer the best opportunity for the rational design of composite materials.

CONCLUSIONS

The mechanics of the thermal shrinkage process in unidirectional fibre composites has been explained and predictions successfully made on the nature of the stresses resulting from the thermal self-straining. The results should be applicable to other composite systems such as reinforced concrete. The present view of the shrinkage process invalidates the interference model as presented by Daniel and Durelli (23).

The shrinkage stresses in composite materials can be very large. The magnitude of the stresses for a given temperature drop, depends on the matrix Young's Modulus, the difference between the coefficients of expansion of matrix and fibre as well as their ratios but is independent of the ratios of the Young's Moduli.

The radial stresses in the transverse plane of the composite are mainly compressive and increase with decreasing fibre spacing except for very close spacings when tensile stresses develop from the centre of the tricorn within the matrix. The greater the difference between the expansion coefficients of the matrix and fibre, the greater the tendency for tensile stresses to develop. Below a certain spacing depending on the particular composite system, the tensile stresses spread out in the matrix and beyond into the fibre; when the fibres lie in continuous contact with each other (i.e. minimum spacing), the tensile stresses

pervade throughout matrix and fibre except in the vicinity of the line of contact where compressive contact stresses exist.

A triaxial state of compression exists in regions lying between the ends of discontinuous fibre ends and the axial stress in this region is always in compression. The likelihood of cracks developing from within this region purely from the shrinkage effects is diminished. However at the tips of the fibre ends the shear stresses are high enough to precipitate initial cracks in a brittle matrix such as a plastic.

For continuous fibre composites the overall strength in compression is enhanced whilst the presence of discontinuities tends to increase the tensile strength due to the nature of the resulting initial stresses from the thermal self-straining.

Good agreement has been found between stress distributions obtained from the plane strain model in the section normal to the fibres using the finite element method, and the experimental model using the technique of photothermoelasticity. By performing suitable calibration tests judged on the merits of the experimental model and method, it has been possible to assign an absolute stress value to the fringes in the restrained shrinkage system. The calibration constant as suggested by Sampson (66) has been found to be irrelelevant and inapplicable.

Plane and axisymmetric model idealisations of the composite system to study the shrinkage stresses around discontinuities have proved inadequate and unsuccessful.

A much more elaborate three-dimensional idealisation of the composite system would be required. However the feasibility of this approach is limited by the available computer storage capacity. Nevertheless, the finite element method has proved a powerful tool and it should therefore be possible to adapt it to solve conventional thermal stress problems encountered in engineering practice.

Finally, because both fibre and matrix failure may be influenced by shrinkage stresses especially in the composites where high performance is sought and a high fibre volume fraction consequently employed, it maybe desirable to design any particular composite material so that the fibre spacing is closely controlled.

R E F E R E N C E S

1. H.L. COX: "The Elasticity and Strength of Paper and Other Fibrous Materials". Brit. Jnl. Appl. Phys. 3, 72, 1952.

2. N.F. DOW: "Study of Stresses near a Discontinuity in a Filament-reinforced Composite Material". GEC Rept. R63SD61, 1963.

3. W.R. TYSON AND G.J. DAVIES: "A photoelastic Study of the Shear Stresses Associated with the Transfer of Stress during Fibre Reinforcement". Brit. Jnl. Appl. Phys. 16, 199, 1965.

4. M.J. IREMONGER AND W.G. WOOD: "Effects of Geometry on Stresses in Discontinuous Composite Materials". Jnl. Strain Analysis, 4, 2 1969.

5. A. KELLY: "Theory of Strengthening of Metals". Ch.1, Composite Materials, Iliffe London 1965.

6. Met. Revs; 10, 37, 1965.

7. "Fibre Composite Materials" (Papers presented at a Seminar of the ASM, Oct. 1964) ASM, Metals Pk, Ohio.

8. J.E. HOVE AND W.C. RILEY: "Ceramincs for Advanced Technologics". Wiley 1965.

9. R.V. COLEMAN: "The Growth and Properties of Whiskers". Met. Revs. 9, 35, 1964.

10. D.W. PETRAESEK AND J.W. WEETON: NASA Tech Note D1568, 1963.

11. D. CRATCHLEY: Powder Met., 11, 59, 1963.

12. D. CRATCHLEY AND A.A. BAKER: Metallurgia, 69, 153, 1964.

13. F. LÁSZLÓ: "Tesselated Stresses". Jnl. of Iron and Steel.
    Pt I - 1, 147, 1943
    Pt II - 2, 148, 1943
    Pt III - 2, 150, 1944
    Pt IV - 2, 152, 1945

14. A.L. FLORENCE AND J.N. GOODIER: "Thermal Stresses at Spherical Cavities and Circular Holes in Uniform Heat Flow". Jnl. Appl. Mech, 26, 293-294, 1959.

15. J. DUNDURS AND O.C. ZIENKIEWICZ: "Stresses Around Circular Inclusions Due to Thermal Gradients with Particular Reference to Reinforced Concrete". Jnl. Amer. Concrete Inst. p.1523, 1964.

16. T.R. TAUCHERT: "Thermal Stress Concentrations in the Vicinity of Cylindrical Inclusions". Jnl. Comp. Mtls. 3, 192, 1969.

17. E. STERNBERG AND E.L. McDOWELL: "On the Steady State Thermoelastic Problem for the Half Space". Quart Appl. Math., 14, 381, 1957.

18. J.O. OUTWATER: "The Mechanics of Plastics Reinforcement in Tension". Mod. Plastics, March 1956.

19. MCA-MIT: "Resin Shrinkage Pressures during Cure". Plastics Research Project, Progress Rept. Jan. 1959.

20. W.H. HASLETT AND F.J. McGARRY: "Shrinkage Stresses in Glass Filament-resin Systems". Mod. Plastics, Dec. 1962.

21. I.M. DANIEL: "Photoelastic Investigation of Residual Stresses in Glass-plastic Composites". ARF report 8194-3, 12, May 1960.

22. I.M. DANIEL AND A.J. DURELLI: "Photoelastic Investigation of Residual Stresses in Glass-Plastic Composites". SPI Sect. 19-A.

23. I.M. DANIEL AND A.J. DURELLI: "Shrinkage Stresses Around Rigid Inclusions". SESA Aug. 1962.

24. R.H. MARLOFF AND I.M. DANIEL: "Three-Dimensional Photoelastic Analysis of a Fibre-Reinforced Composite Model". SESA April 1969.

25. T. KOUFOPOULOS AND P.S. THEOCARIS: "Shrinkage Stresses in Two-Phase Materials". Jnl. Comp. Matls. 3, 308, 1969.

26. A.W. LEISSA AND W.E. CLAUSSEN: "Application of Point-Matching to Problems in Micromechanics". Ch.3. "Fundamental Aspects of Fibre-Reinforced Plastic Composites". Wiley, 1968.

27. "Composite Materials": Ed. L. HOLLIDAY, Van Nostrand, 1965.

28. D.F. ADAMS, D.R. DONER and R.L. THOMAS: "Mechanical Behaviour of Fibre Reinforced Composite Materials". Air Force Mtls. Lab., AFML-TR 67-96, 1967.

29. M.J. IREMONGER: Ph.D. Thesis, University of London 1968.

30. D.R.J. OWEN, J. HOLBECHE AND O.C. ZIENKIEWICZ: "Elastic-Plastic Analysis of Fibre-Reinforced Materials". Fibre Science and Technology, Elsevier Publ. Co. Ltd., England p.185, 1969.

31. L.J. BROUTMAN AND F.J. McGARRY: "Glass-Resin joint Strength Studies"; Mod. Plastics, Sept. 1962.

32. M.J. TURNER, R.W. CLOUGH, H.C. MARTIN AND L.J. TOPP: "Stiffness and Deflection Analysis of Complex Structures", Jnl. Aero Sci., 23, 9, Sept. 1956.

33. O.C. ZIENKIEWICZ AND Y.K. CHEUNG: "The Finite Element Method in Structural and Continuum Mechanics". Mc-Graus-Hill, 1967.

34. R.V.SOUTHWELL: "Relaxation Methods in Engineering Science" OUP, 1940.

35. B. FRAEJIS DE VEUBEUKE: "Displacement-Equilibrium Models in Finite Element Method", Ch.9 of Stress Analysis ed. O.C. ZIENKIEWICZ AND G.S. HOLISTER, Wiley 1965.

36. E.L. WILSON: "Finite Element Analysis of 2-Dimensional Structures." Structures and Materials Research, Department of Civil Engineering, Rept. No. 63-2, June 1963, Univ. of California.

37. D.F. ADAMS AND D.R. DONER: "Transverse Normal Loading of a Unidirectional Composite". Jnl. Comp. Mtls. 1, 1967.

38. M.J. IREMONGER AND W.G. WOOD: "Stresses in a Composite Material with a Single Broken Fibre", Jnl. Strain Analysis, 2, 239, 1967.

39. A.H. COTTRELL: "Strong Solids" Proc. Roy. Soc., 2, 1964.

40. "Physics and Chemistry of Ceramics". Ed. Cyrus KLUIGSBERG, GORDON AND BREACH, N.Y. 1963.

41. D.L. McDANIELS, R.W. JECH AND J.W. WEETON: NASA Tech. Note D-1881, 1963.

42. A. KELLY AND W.R. TYSON: "Proceedings of the 2nd International Materials Symposium", California 1964, Wiley.

43. A. KELLY AND W.R. TYSON: "Tensile Properties of Fibre-Reinforced Metals: Copper/Tungsten and Copper/Molybolenum". Jnl. Mech. Phy. Solids, 13, 1965.

44. C.J. SMITHELLS: "Metals Reference Book", Vols 1-3, Butterworths, London 1967.

45. D. SCHUSTER AND E. SCALA: "The Mechanical Interaction of Sapphire Whiskers with a Birefringent Matrix". Trans. Am . Inst. Min. Eng. 230, 1635, 1964.

46. J.S. ISLINGER ET AL: "Mechanism of Reinforcement of Fibre-Reinforced Structural Plastics and Composites". WADC TR 59-600 Pt 1, March 1960.

47. R.D. MOONEY AND F.J. McGARRY: "Resin-Glass Bond Study". 14th Am. Conf. Reinforced Plastics Div., SPI, Feb. 1956.

48. B.E. GATEWOOD: "Thermal Stresses in Long Cylindrical Bodies". Phil. Mag., Sev.7, 32, 1941.

49. H.T. JESSOP AND F.C. HARRIS: "Photoelasticity, Principles and Methods", Cleaver-Hum Press Ltd., London.

50. A.J. DURELLI AND W.R. RILEY: "Introduction to Photomechanics". Prentice-Hall, 1965.

51. M.M. FROCHT: "Photoelasticity" Vols. I & II, Wiley, 1957.

52. E.G. COKER AND L.N.G. FILON: "Photoelasticity" 2nd ed. CUP 1932.

53. G. GERARD: "Progress in Photothermoelasticity", Symposium on Photoelasticity, ed. M.M. FROCHT, Pergamon, 1963.

54. R.C. SAMPSON AND D.M. CAMPBELL: "Contribution of Photoelasticity to Evaluation of Solid Propellant Motor Integrity". Jnl. Spacecraft, 4, April 1966.

55. A.J. DURELLI AND V.J. PARKS: "New Method to Determine Restrained-Shrinkage Stresses in Propellant Grain Models", SESA, Nov. 1963

56. "Physics of Plastics", Ed. P.D. RITCHIE, London Iliffe, 1961.

57. P.S. THEOCARIS: "Viscoelastic Properties of Epoxy Resins Derived from Creep and Relaxation Tests at Different Temperatures". Rheologica Acta 2, 2, 1962.

58. P. MEARES: "Polymers: Structure and Bulk Properties". Van Mostrand 1965.

59. S.M. CRAWFORD AND H. KOLSKY: Proc. Phys. Soc. (London) 119, 1364, 1951.

60. L.R.G. TRELOAR: "The Physics of Rubber Elasticity". Clavendon, 1958.

61. D.W. SAUDNERS: "The Photo-Elastic Properties of Cross-Linked Amorphous Polymers", Trans. Faraday Soc. 52, 1414-3C, 1956.

62. I.M. DANIEL AND A.J. DURELLI: "Photothermoelastic Analysis of Bonded Propellant Grain" SESA March 1961.

63. "Araldite CT200 for Photoelastic Models", Ciba Instruction Sheet No. M32a, CIBA (ARL) Ltd., Duxford, Camb., England.

64. H. SPOONER AND L.D. McCONNELL: "An Ethoxyline Resin for Photoelastic Work", Brit. Jnl. Appl. Phys. p.181-4, June 1953.

65. M.M. LEVEN: "Epoxy Resins for Photoelastic Use", from ref. 53.

66. R.C. SAMPSON: "A Three-Dimensional Photoelastic Method for Analysis of Differential Contraction Stresses", SESA Sept. 1963.

67. M. HETENYI: "Handbook of Experimental Stress Analysis", Wiley N.Y.

68. J.W. DALLY AND W.F. RILEY: "Experimental Stress Analysis", McGraw Hill, 1965.

69. H.T. JESSOP: "Equilibrium Equations Along a Stress Trajectory in Three-Dimensions". Jnl. Sci. Instr. 26, Jan. 1949.

70. M.M. FROCHT AND R. GUERNSEY: "A Special Investigation to Develop a General Method for Three-Dimensional Photo-Elastic Stress Analysis", NACA Tech. Note 2833, Dec. 1952.

71. A.J. DURELLI AND V.J. DORKS: "Photoelastic Stress Analysis on the Bonded Interface of a Strip with Different End Configurations". Amer. Ceram. Soc. Bull. 46, June 1967.

72. I.N. MUCKHELISHVILI: "Some Basic Problems in the Mathematical Theory of Elasticity", P. NOORDHOFF, 1963.

73. S. TIMOSHENKO AND J.N. GOODIER: "Theory of Elasticity" McGraw Hill.

74. A.A. BAKER AND D. CRATCHLEY: Appl. Matts. Research Vol. 3, 215 1964.

75. R.K. HAM AND J.A. PLACE: "The Failure of Copper-Tungsten Fibre Composites in Repeated Tension". Jnl. Mech. Phys. Solids. 14, 1966.

76. B.W. ROSEN: "Mechanics of Composite Strengthening", Ch. 3 of Ref. 7.

77. J.O. OUTWATER: "The Promise and Reality in Filament-wound Laminates", Chemical Engineer, Oct. 1964.

78. W.H. SUTTON ET AL: Gen. Elect Co. Rept. Contract NOW-60-0465-d, 1960-64.

79. R.W. CLOUGH: "The Finite Element Method in Structural Mechanics". Ch. 7 of Ref. 35.

80. G. TEMPLE AND W.G. BICKLEY: "Raleigh's Principle and its Application to Engineering", OJP 1933.

81. A. MATTING AND G. EHRENSTEIN: "Interfacial Stresses in Glass Reinforced Plastics", Rept. of the Institute for Material Science of the Technical University, Berlin, 1966.

82. T.F. MACLAUGHLIN: "A Photoelastic Analysis of Fiber Discontinuities in Composite Materials", Jnl. Comp. Matts. 2, 1, 1968.

83. G.S. HOLISTER AND C. THOMAS: "Fibre Reinforced Materials", Elsevier, 1966.

84. 'Modern Computing Methods': Notes on Applied Science No.16 HMSO: 1961.

85. L.E.HULBERT: "The Numerical Solution of Two-Dimensional Problems of the Theory of Elasticity", Bulletin 198, Engineering Experiment Station, The Ohio State University, Columbus, 1963.

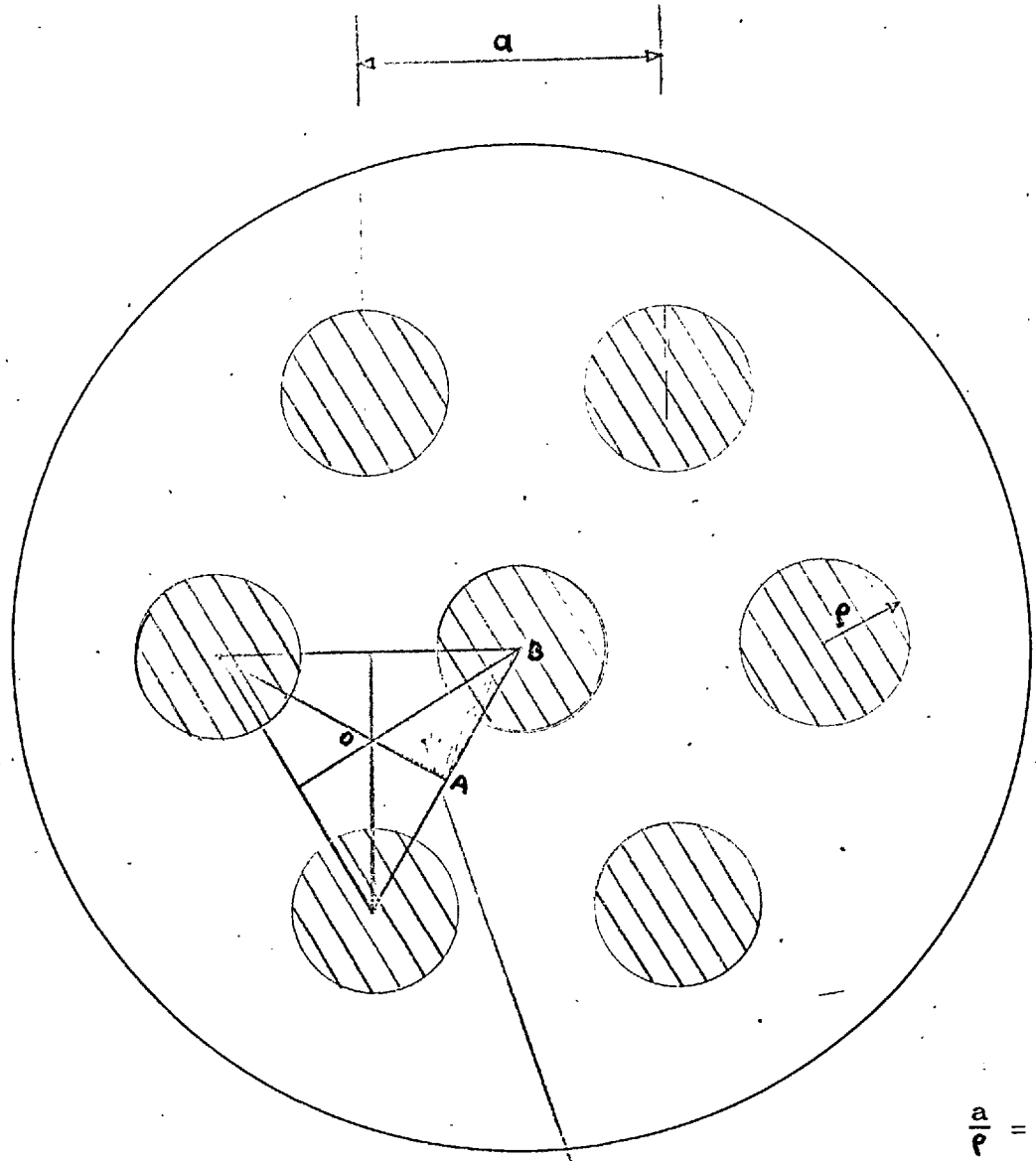

FIG.1.1: HEXAGONAL ARRANGEMENT OF FIBRES.

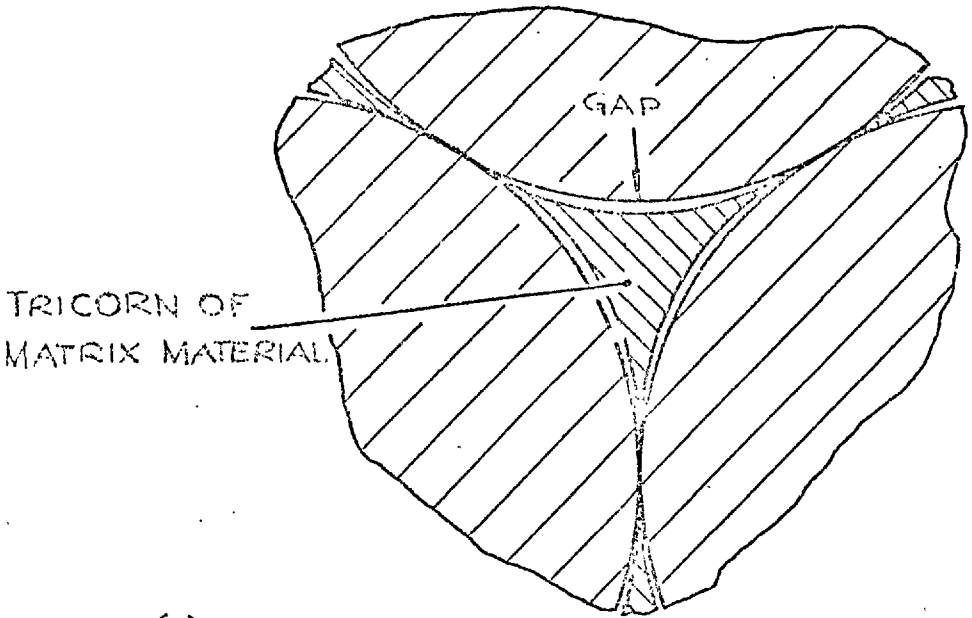

(a) INTERFERENCE MODEL, CLOSE PACKED RODS.

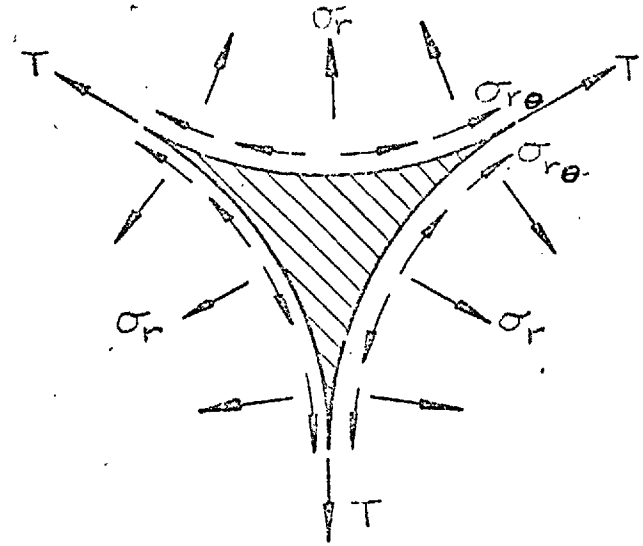

(b) TRACTIONS ON TRICORN OF ACTUAL SHRINKAGE SYSTEM

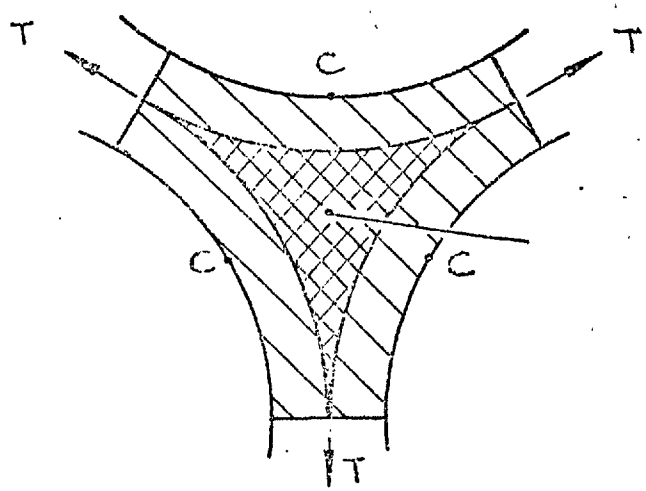

(c) GEOMETRY FOR RODS NOT TOUCHING

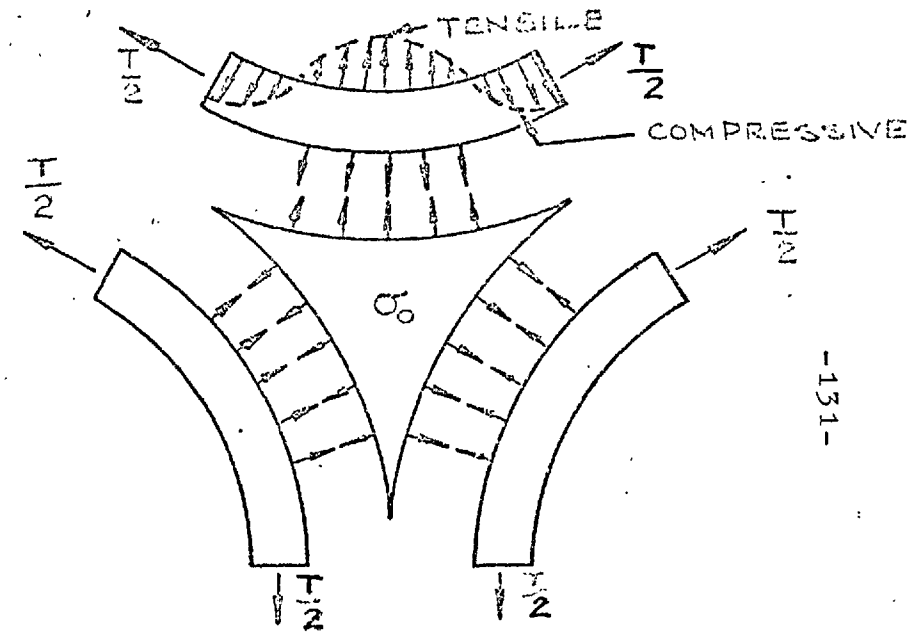

(d) SIMPLIFIED STRESS SYSTEM FOR (C)

FIG 1·2 THE INTERFERENCE AND ACTUAL SHRINKAGE SYSTEMS.

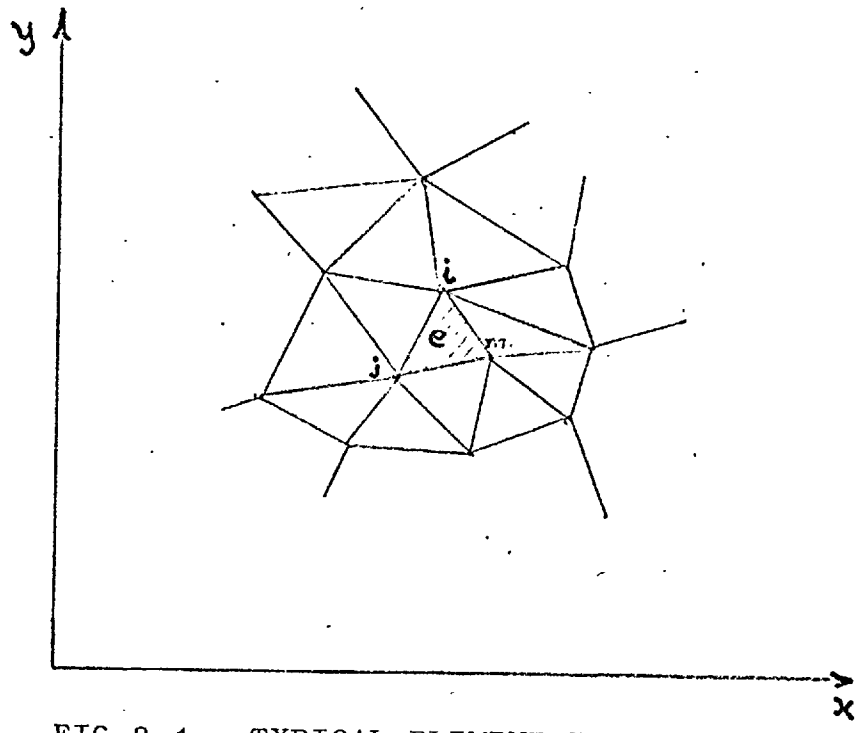

FIG.2.1a: TYPICAL ELEMENT IN A TRIANGULAR MESH.

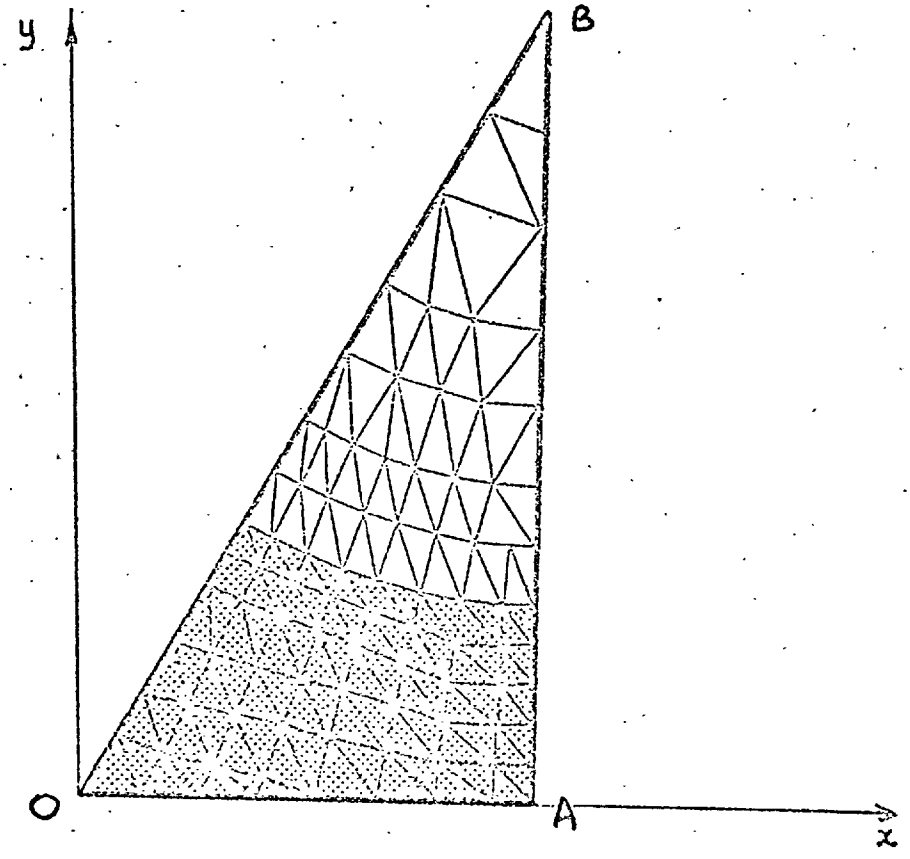

FIG:2.1b: TYPICAL TRIANGULAR MESH FOR FINITE ELEMENT ANALYSIS.

FIG.3.1: TYPICAL MESH (FULL-SIZE) FOR PLANE STRAIN ANALYSIS OF CONTINUOUS FIBRES, m=4.5,

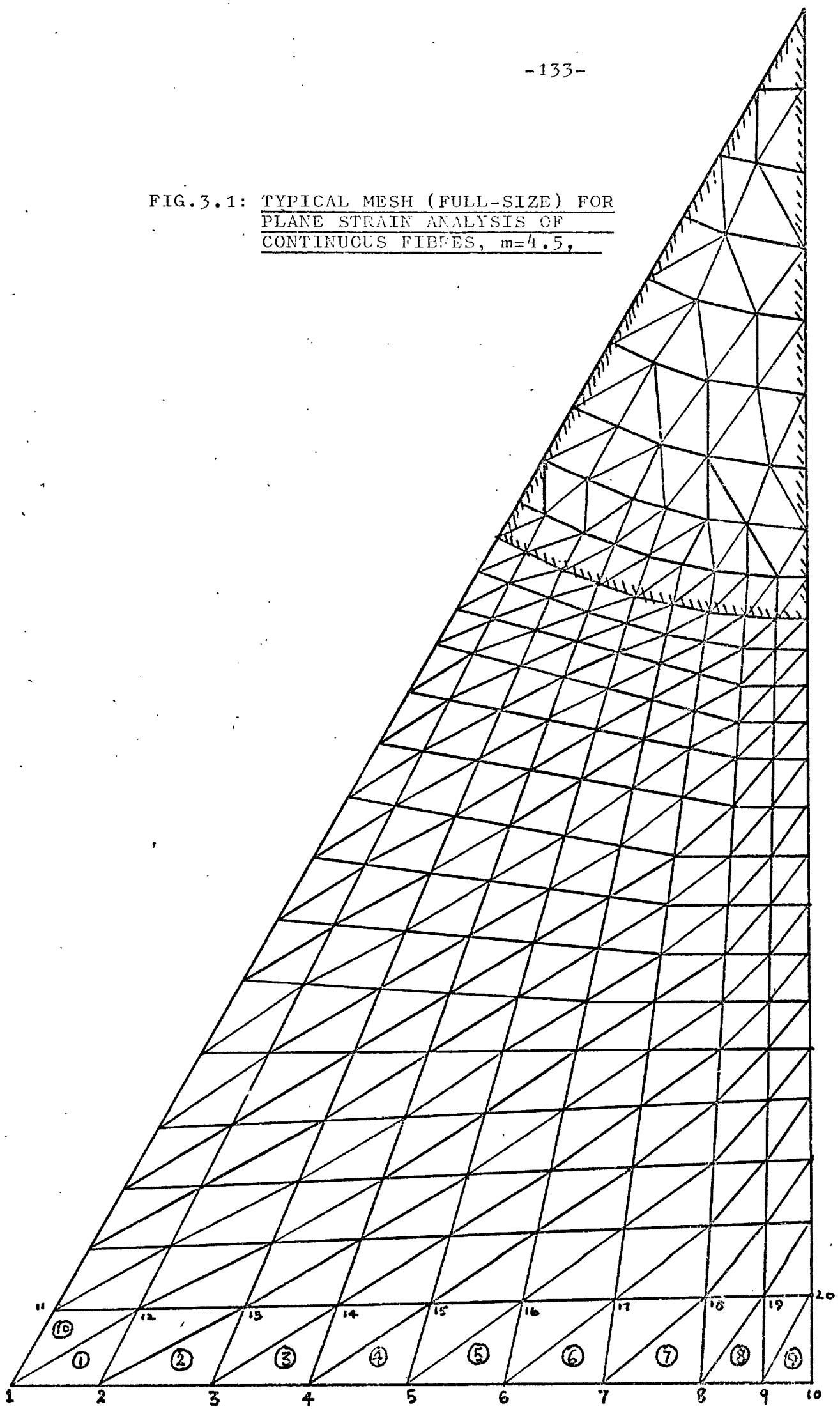

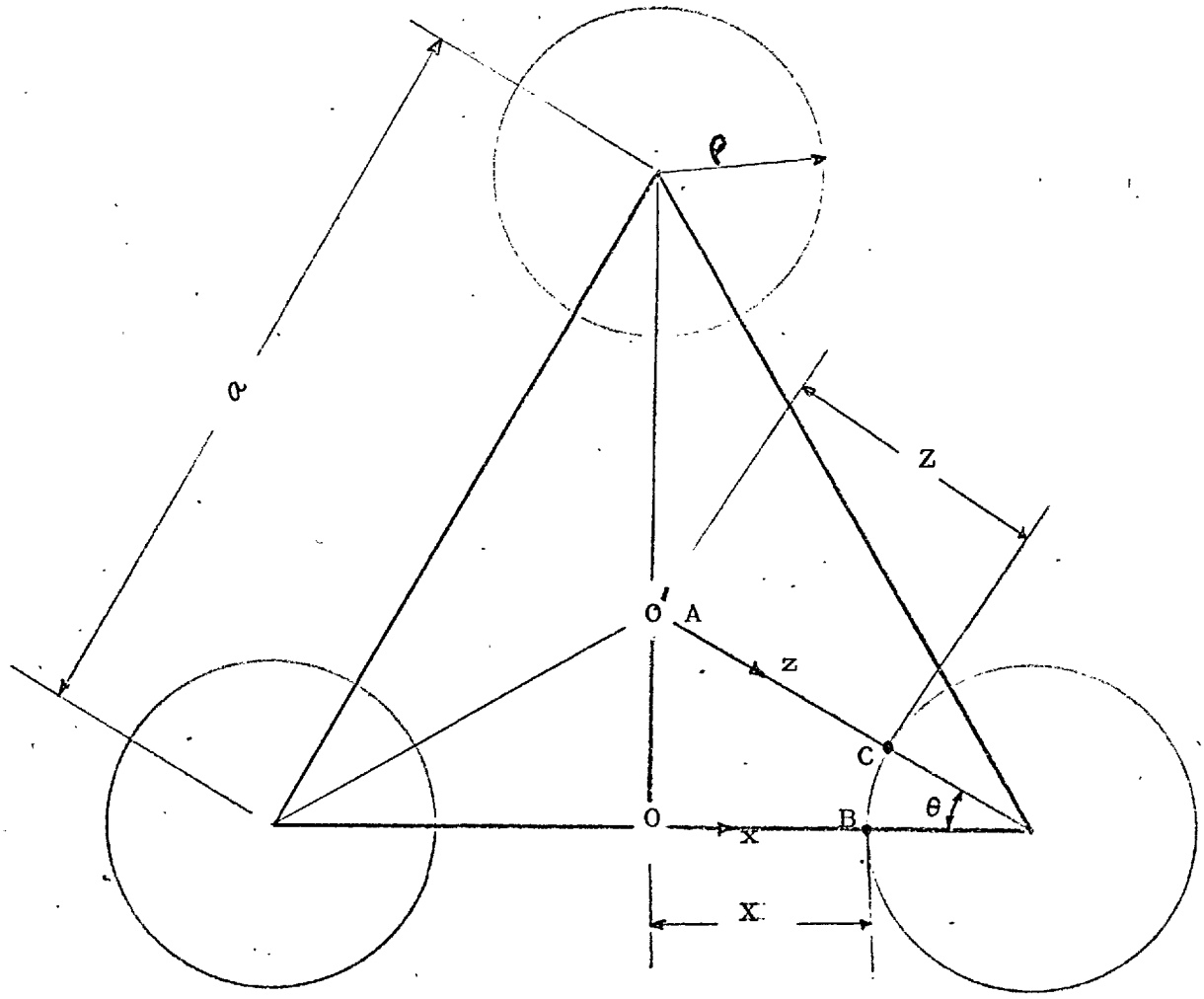

FIGURE 3.2: SELECTED LINES AND POINTS FOR PLOTTING STRESSES.

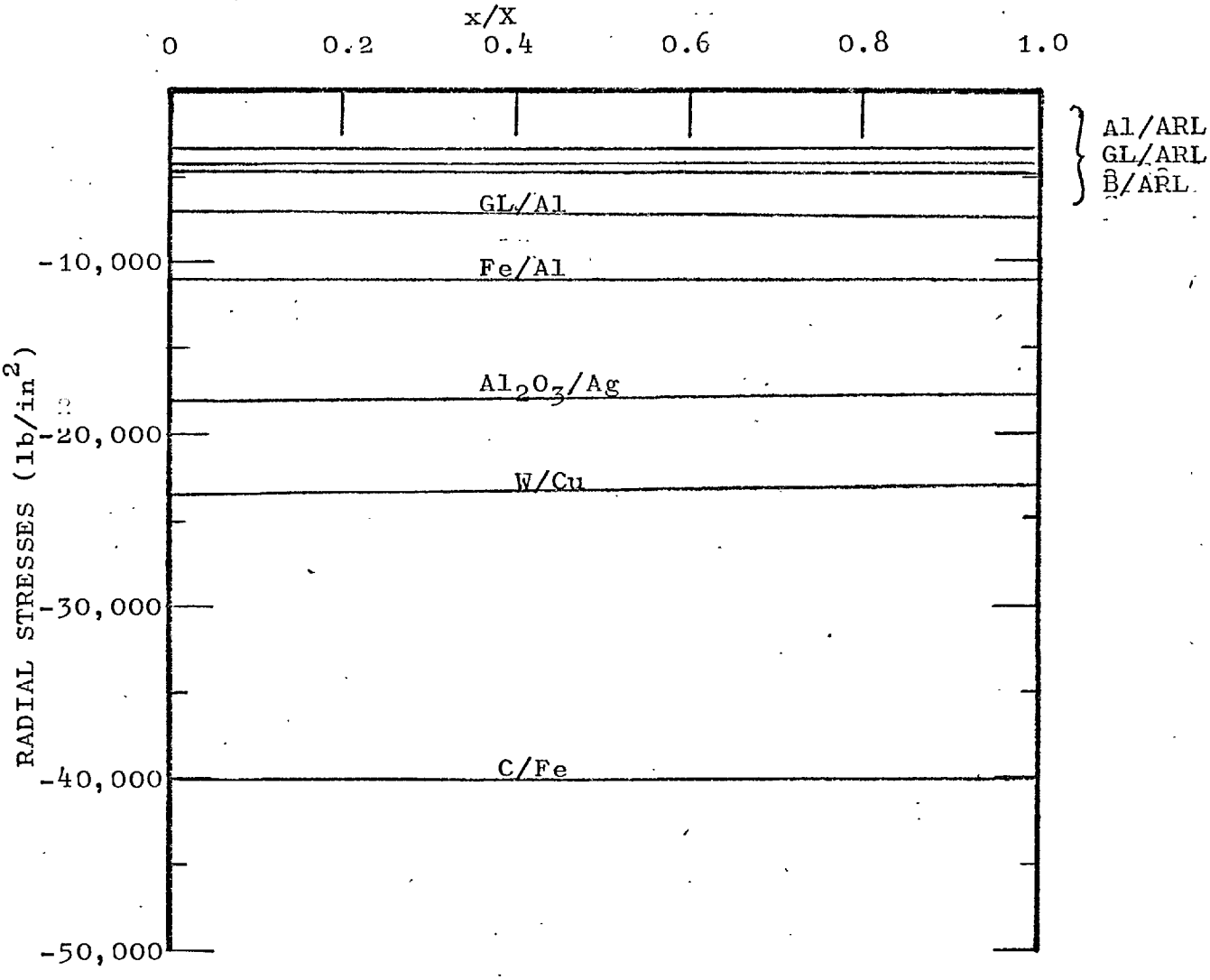

FIGURE 3.3a: VARIATION OF RADIAL STRESS ON ox FOR m=2.08.

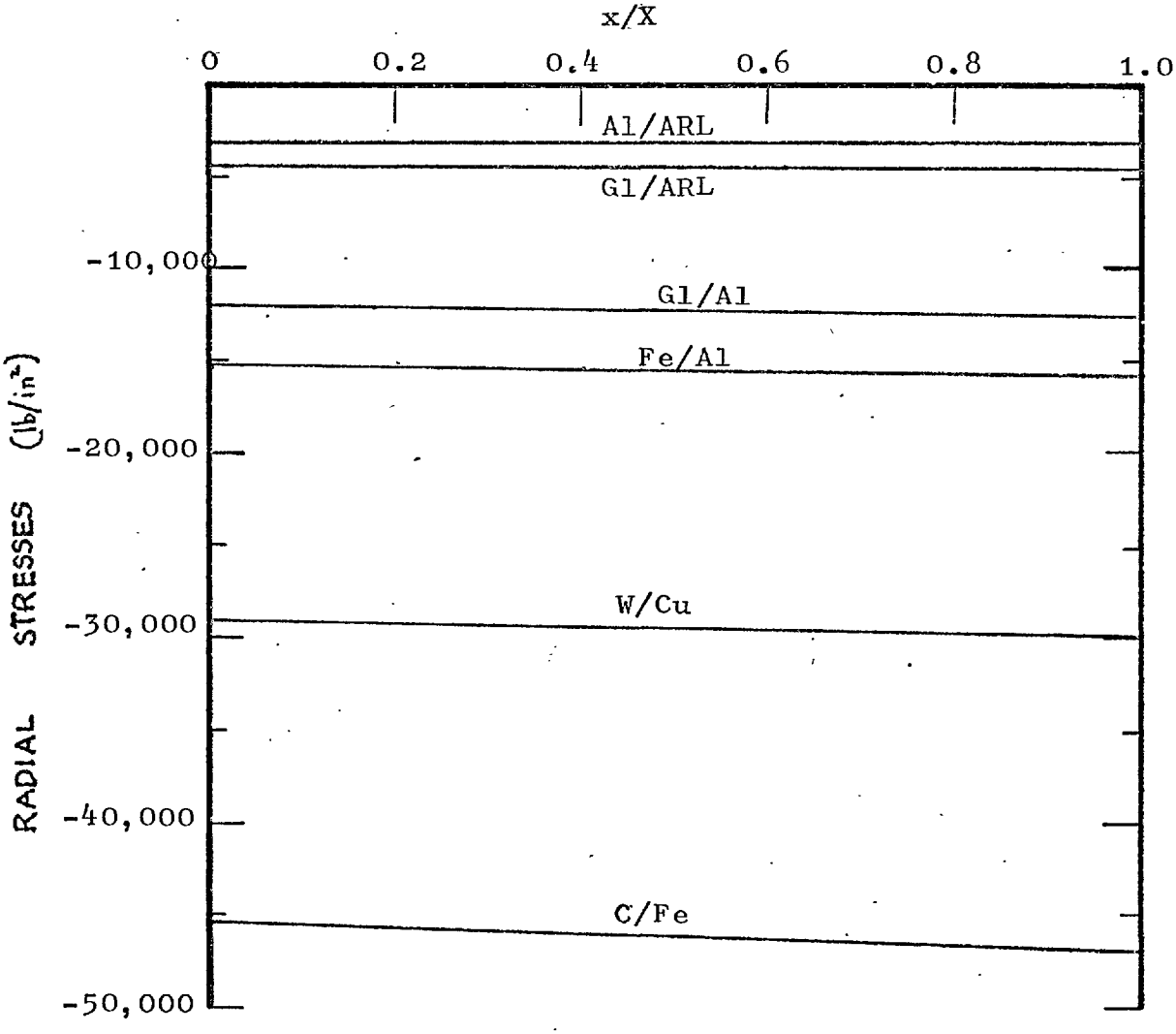

FIG. 3.3b: VARIATION OF RADIAL STRESS ON ox FOR m=2.125.

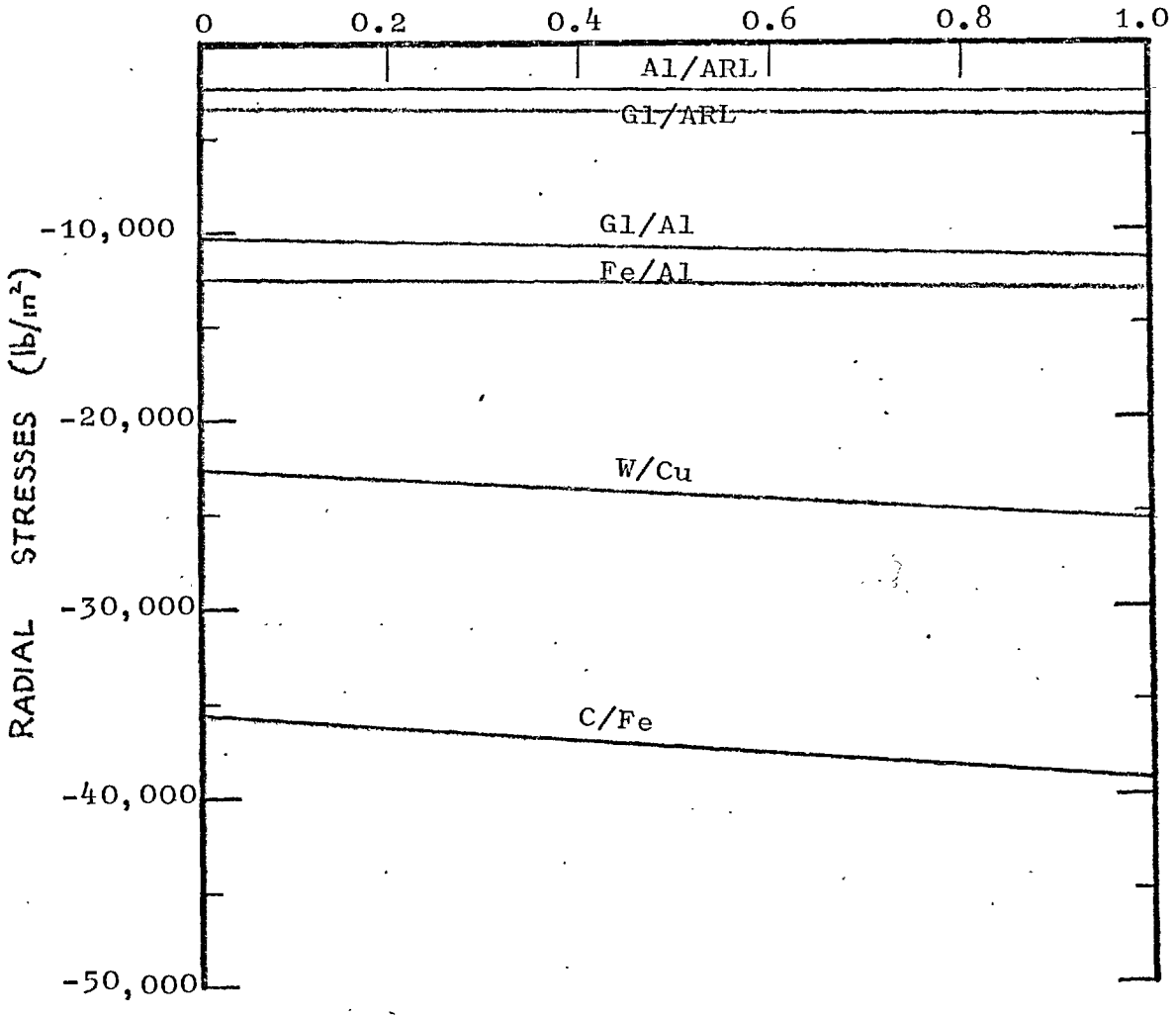

FIG. 3.3c: VARIATION OF RADIAL STRESS ON σx FOR m=2.5.

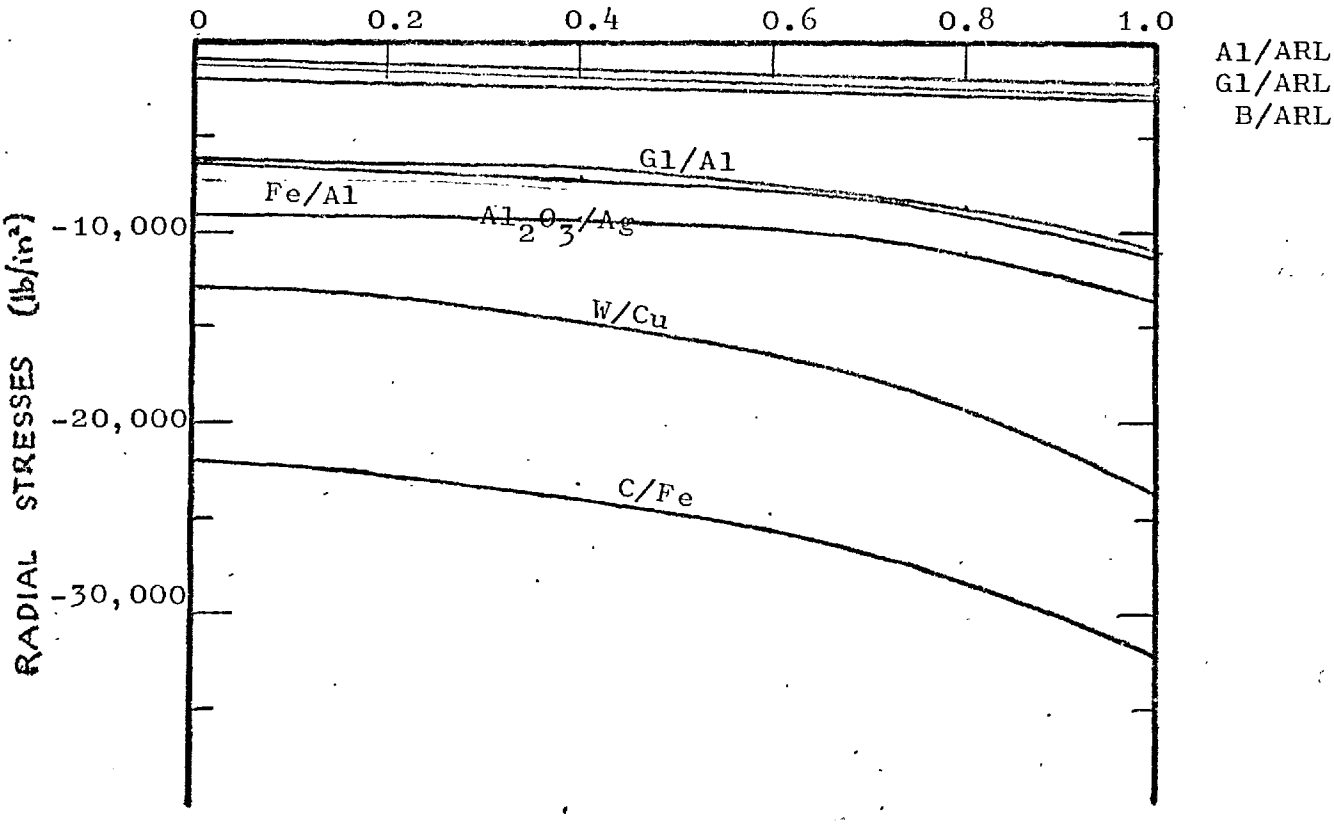

FIG.3.3d:VARIATION QF RADIAL STRESS ON ox FOR m=3.

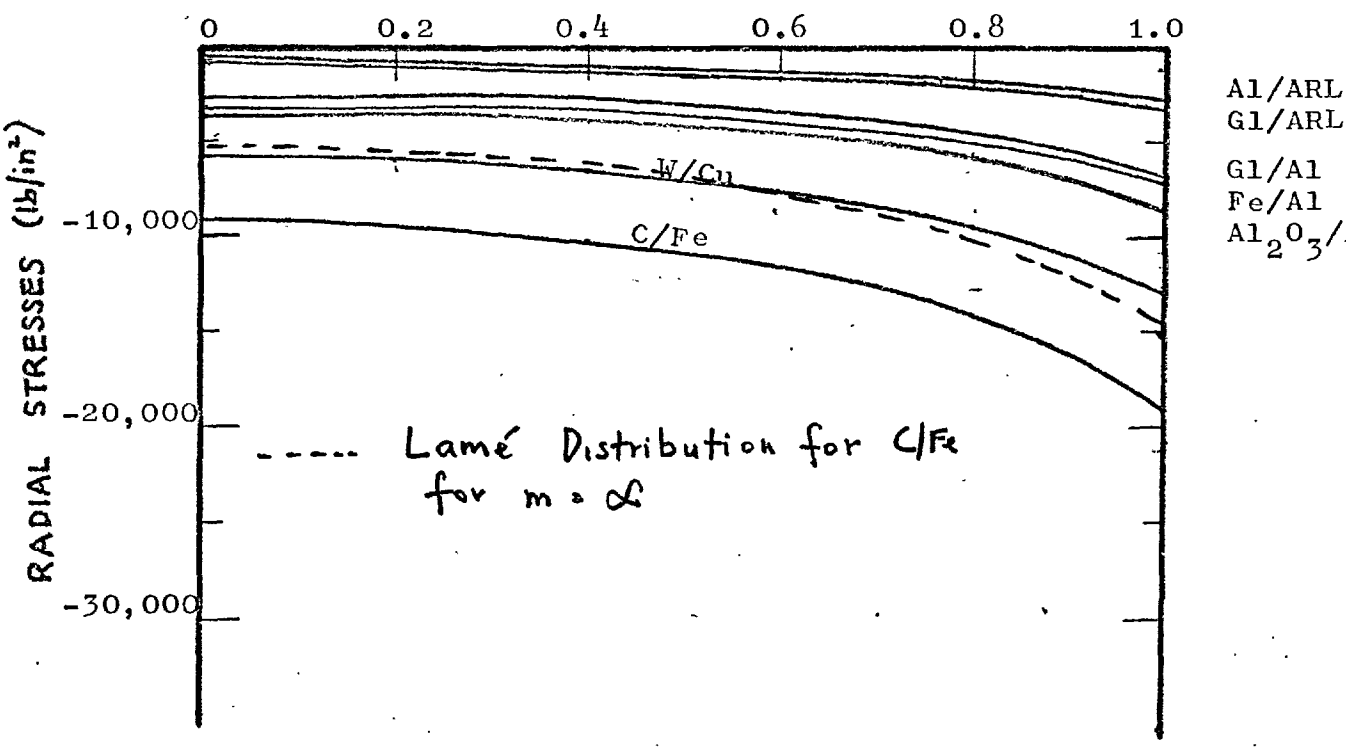

FIG.3.3e:VARIATION OF RADIAL STRESS ON ox FOR m=4.5

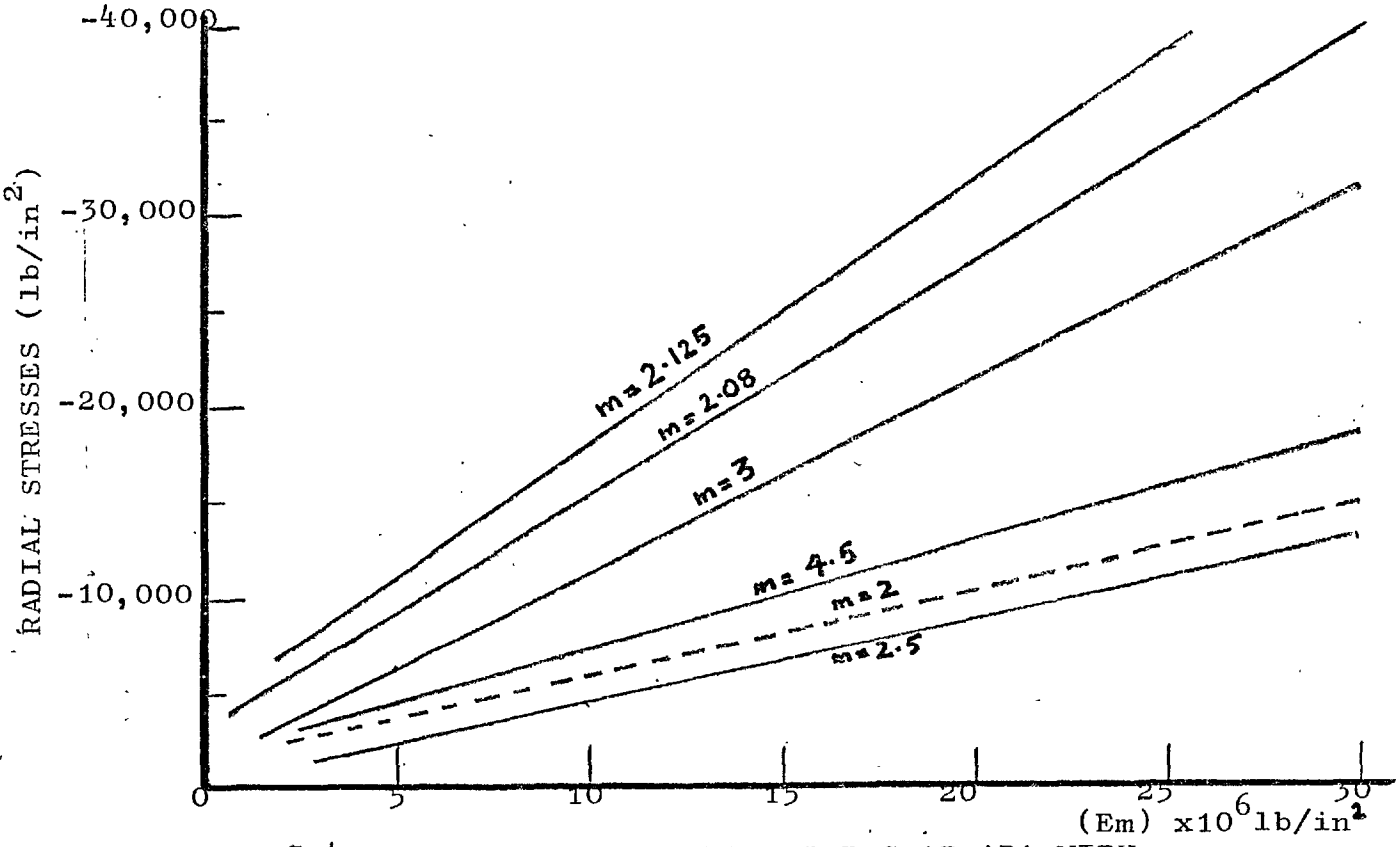

FIG.3.4a: VARIATION OF RADIAL STRESS AT 'B' WITH YOUNG'S MODULUS (Em) OF MATRIX.

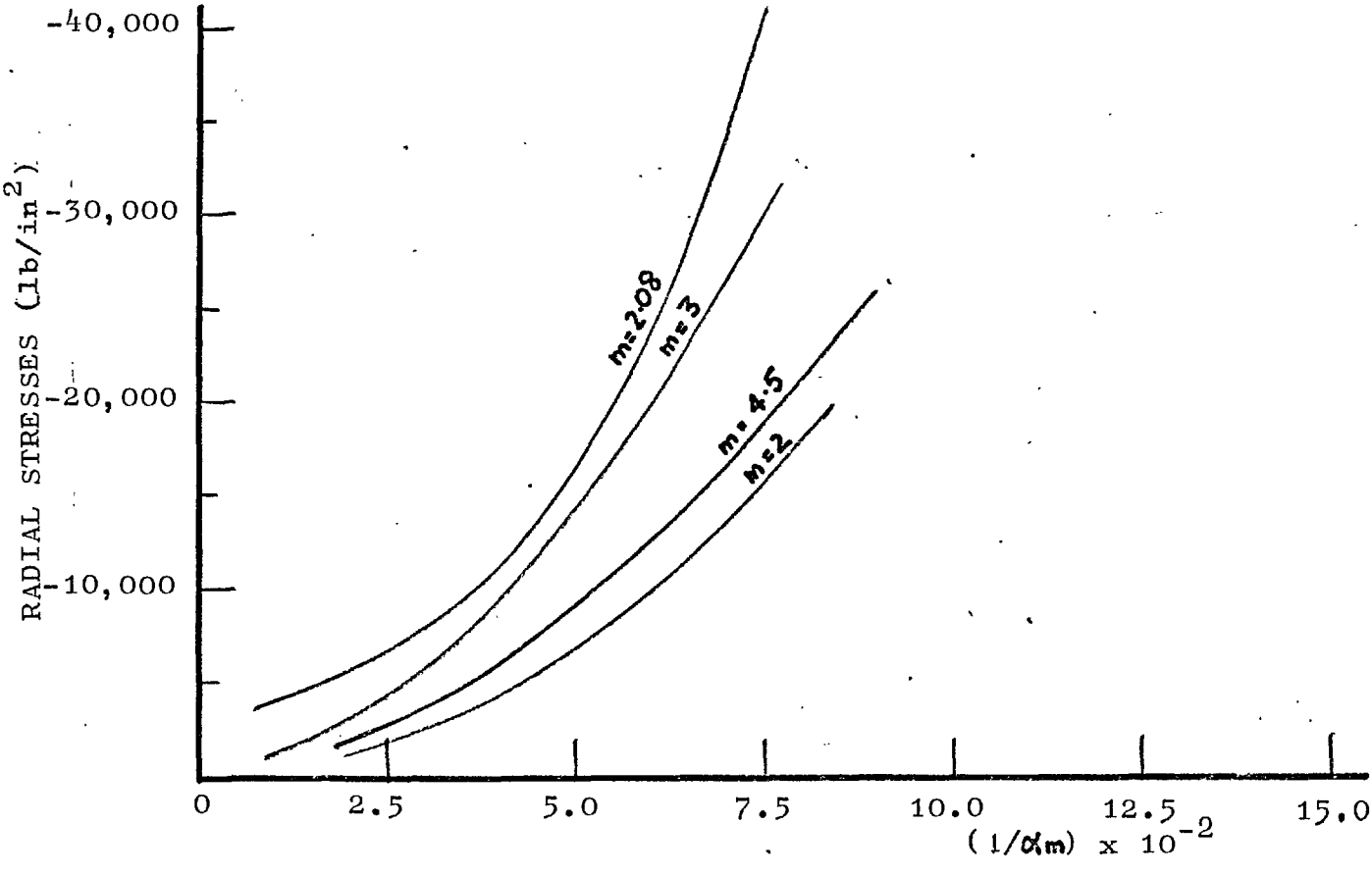

FIG.3.4b: VARIATION OF RADIAL STRESS AT 'B' WITH RECIPROCAL OF COEFFICIENT OF THERMAL EXPANSION (α_m) OF MATRIX.

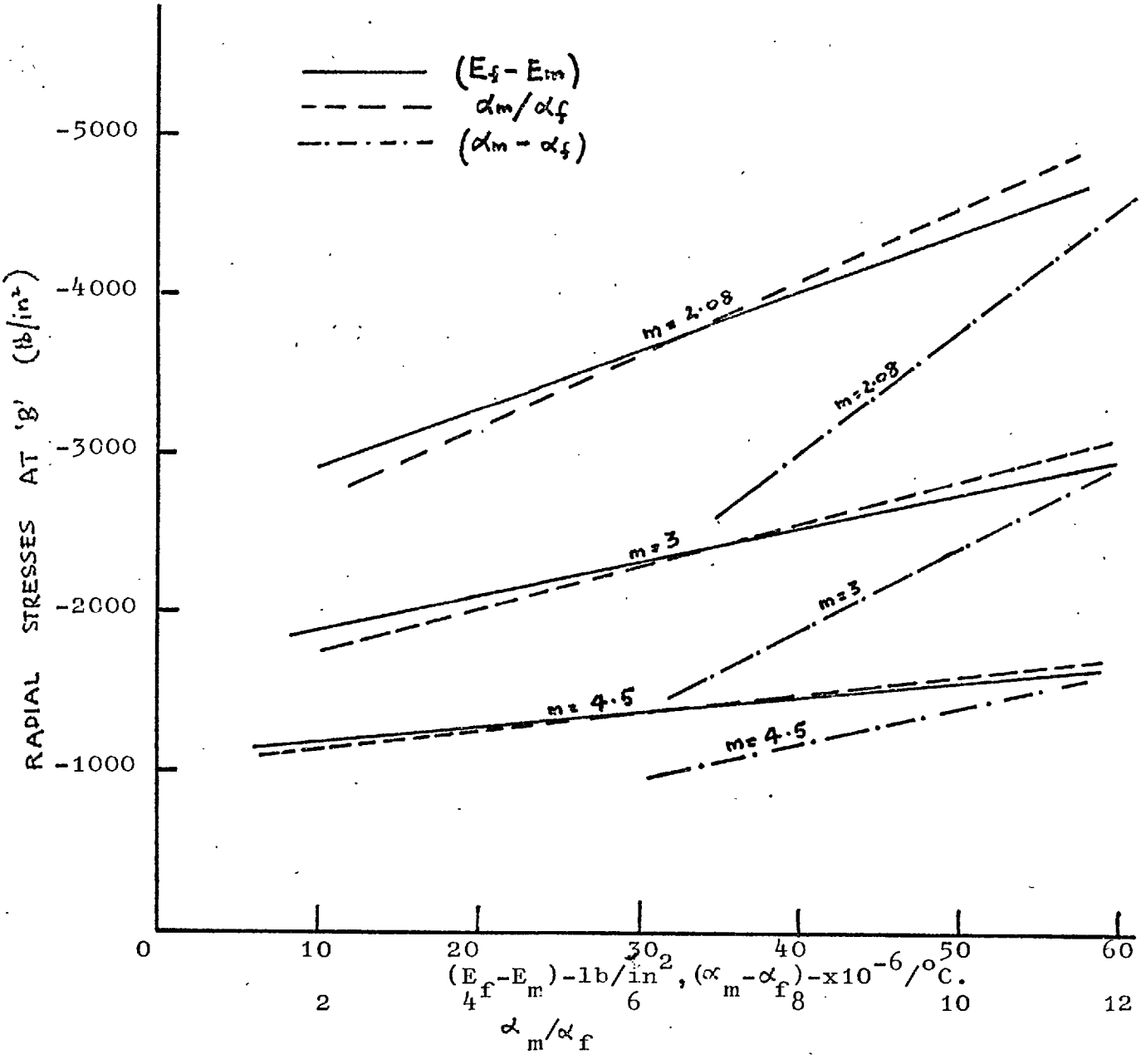

FIG.3.4c: VARIATION OF RADIAL STRESS AT 'B' WITH $(E_f - E_m)$, $(\alpha_m - \alpha_f)$ and α_m/α_f FOR ARALDITE COMPOSITE SYSTEMS.

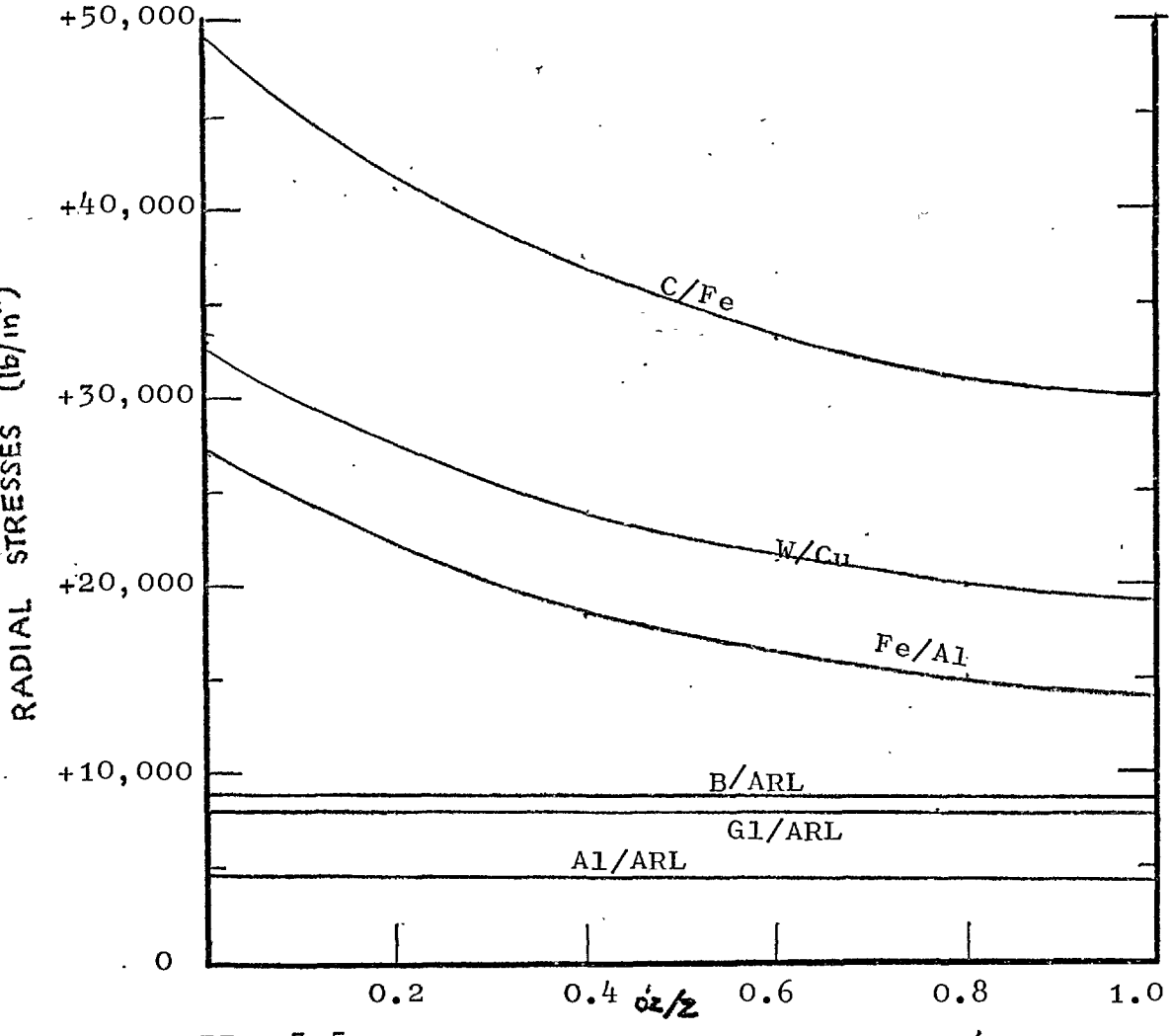

FIG. 3.5a VARIATION OF RADIAL STRESS ON σ'_z FOR m=2.

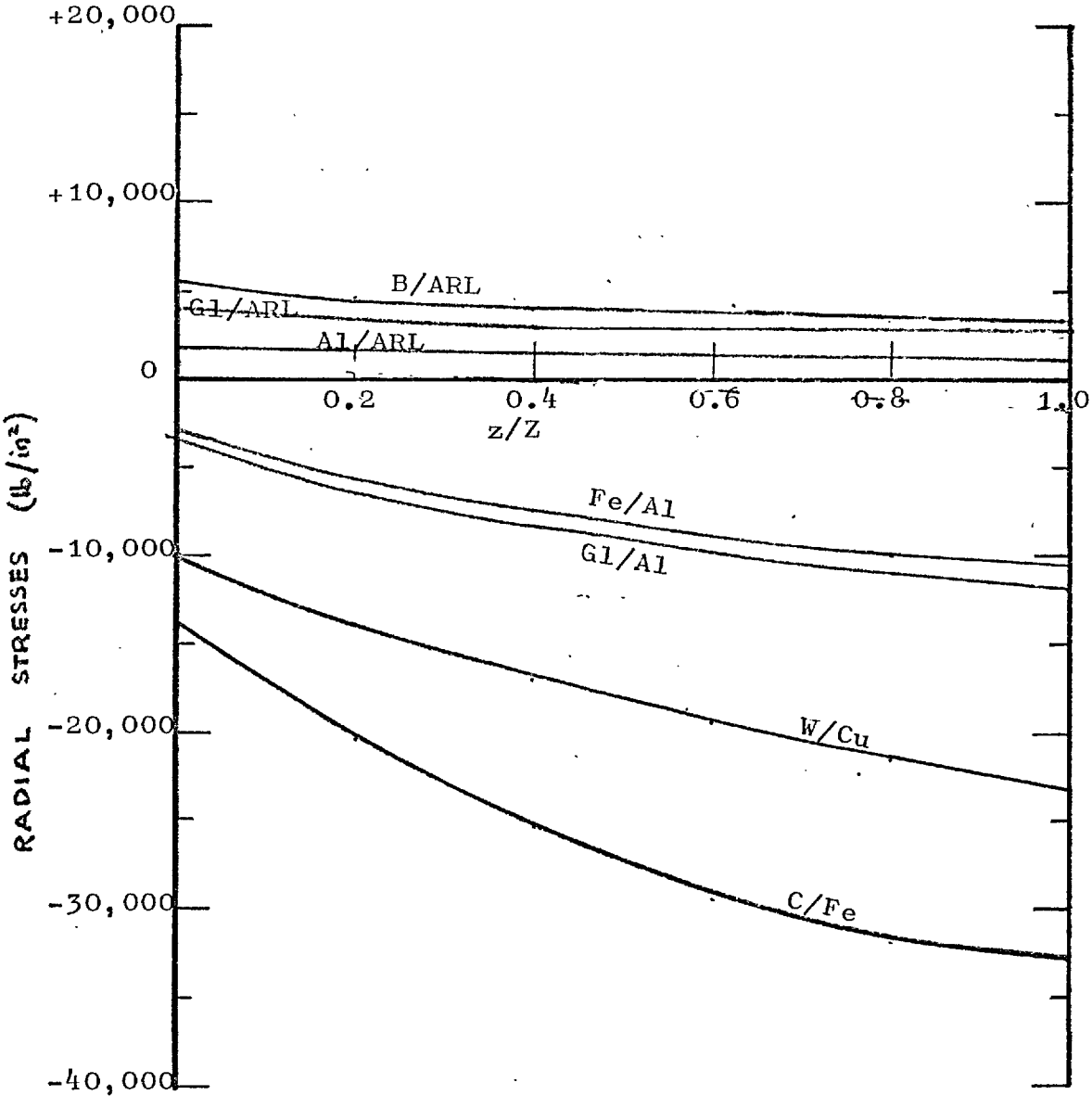

FIG.3.5b: VARIATION OF RADIAL STRESS ON σ_z FOR m=2.08.

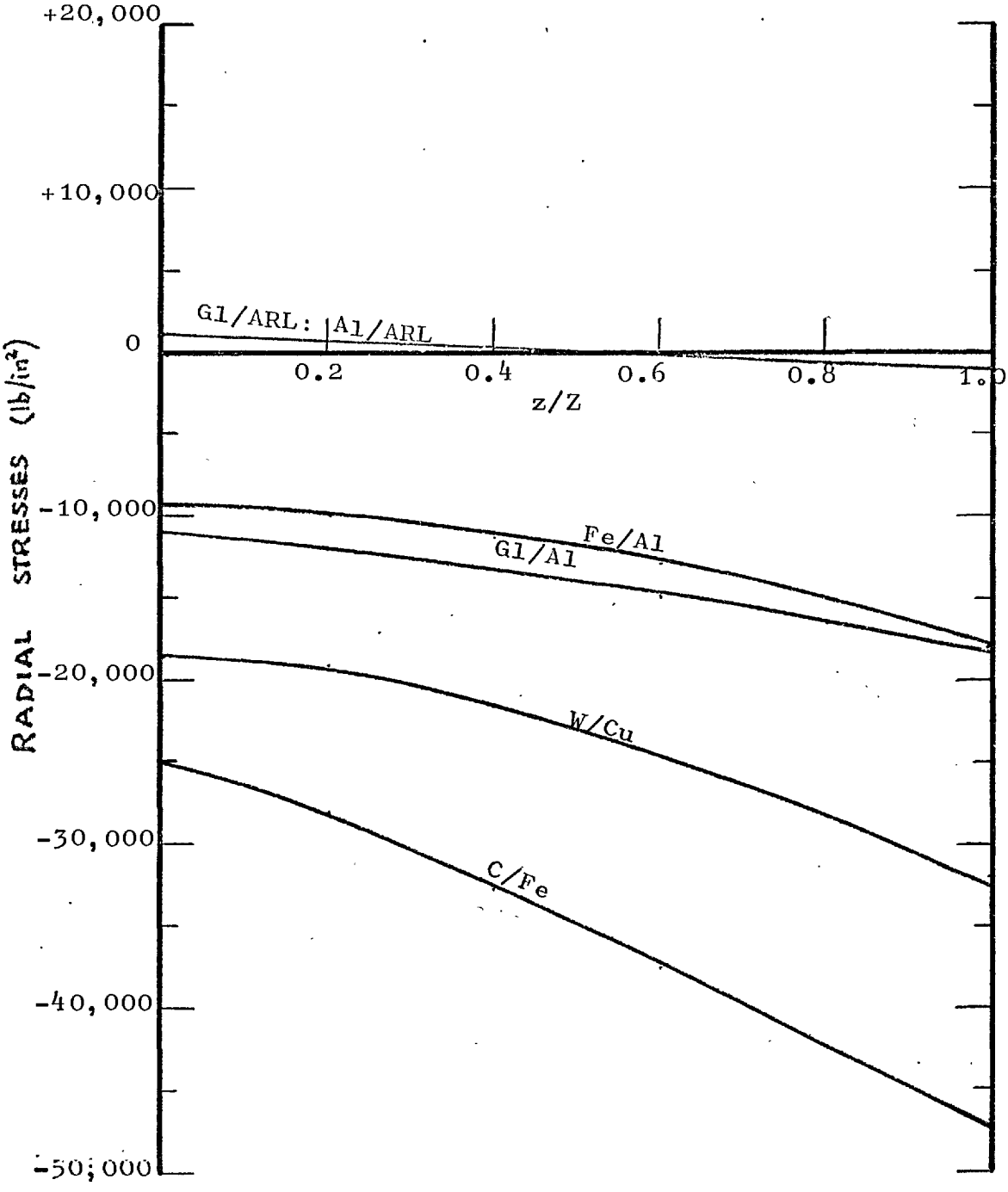

FIG. 3.5c: VARIATION OF RADIAL STRESS ON σ_z FOR m=2.125.

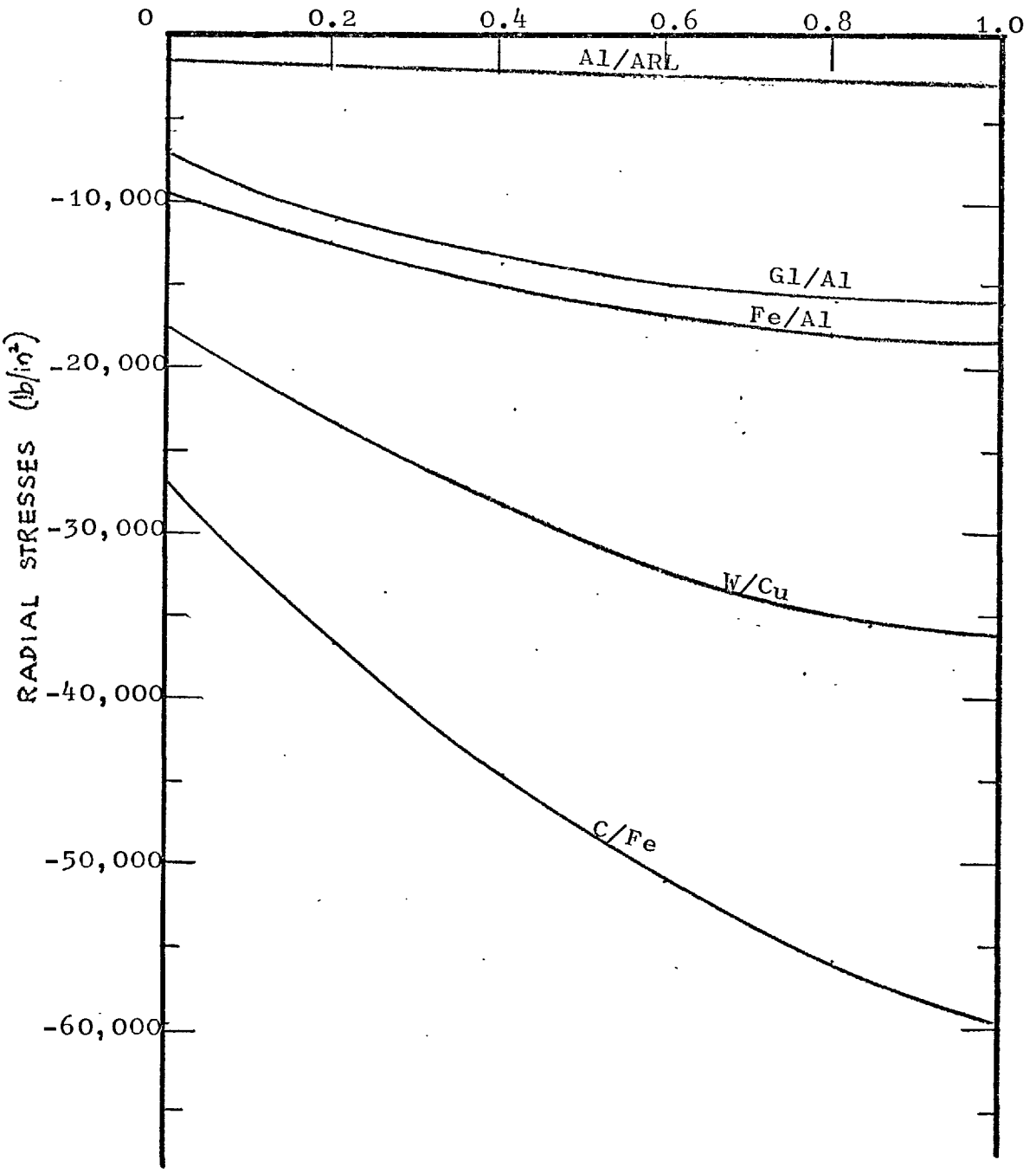

FIG. 3.5d VARIATION OF RADIAL STRESS ON σ_z' FOR m=2.5.

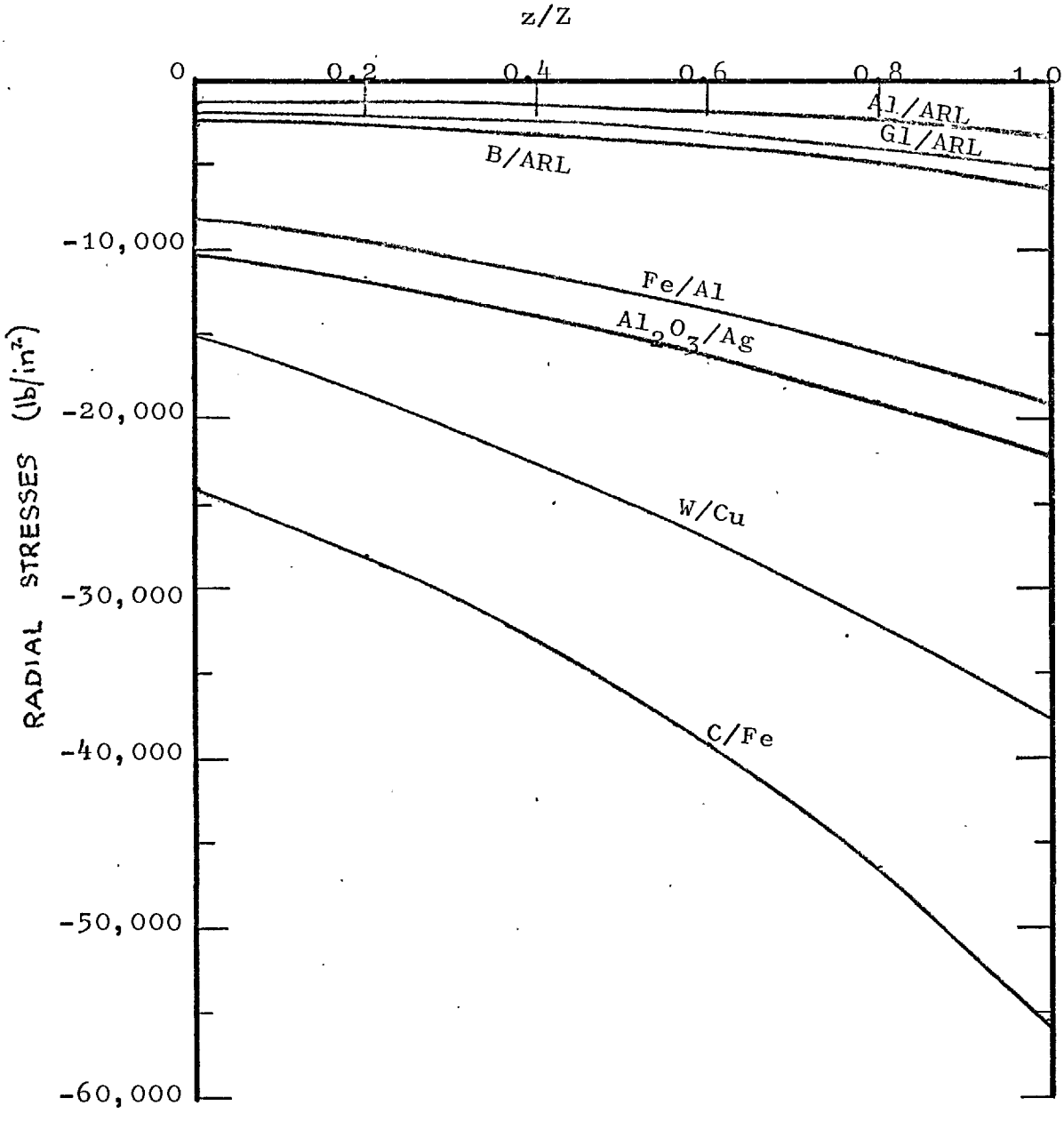

FIG.3.5e: VARIATION OF RADIAL STRESS ON σ_z FOR m=3.

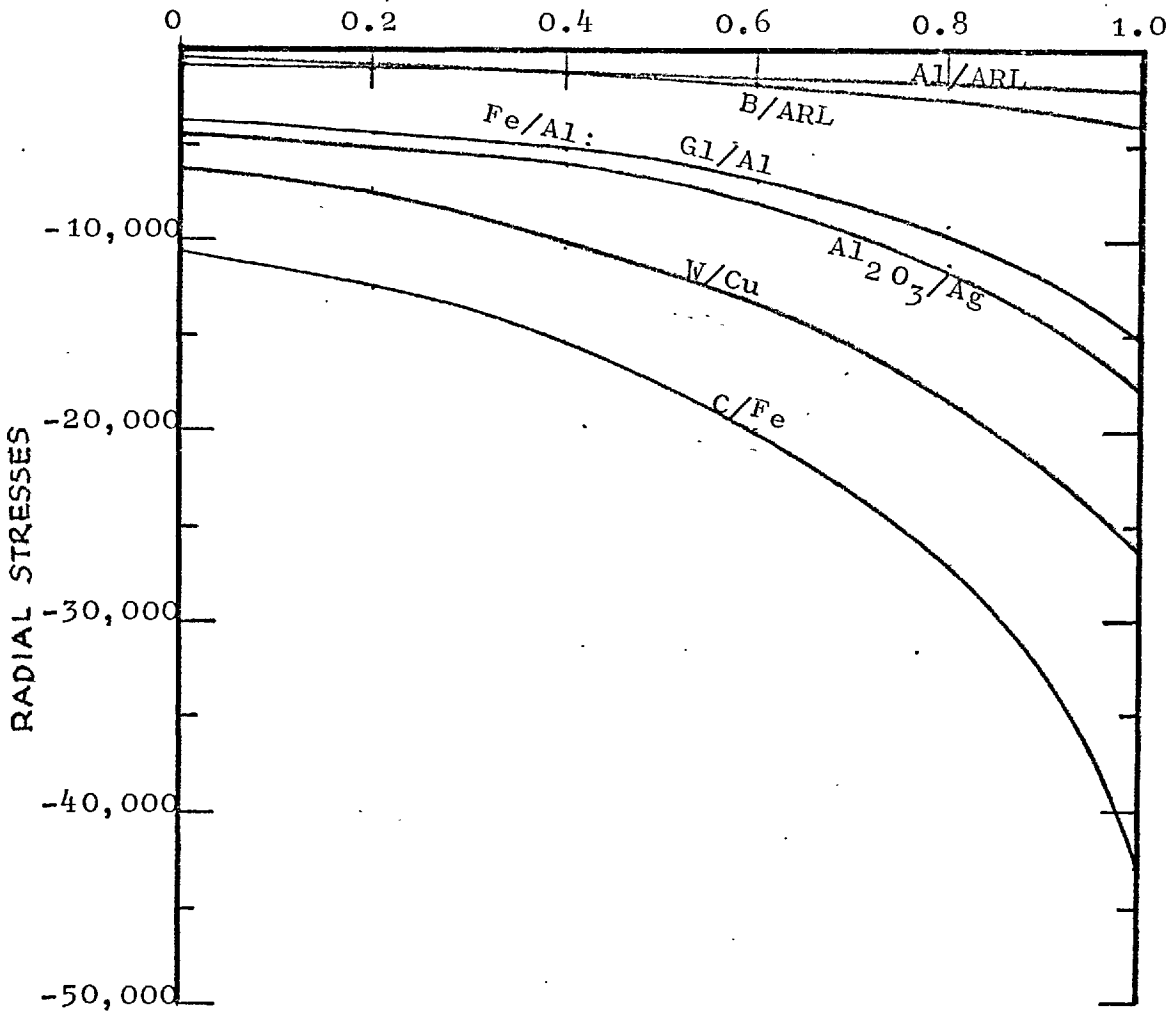

FIG.3.5f : VARIATION OF RADIAL STRESS ON σ_z FOR m=4.5.

FIG. 3·6a

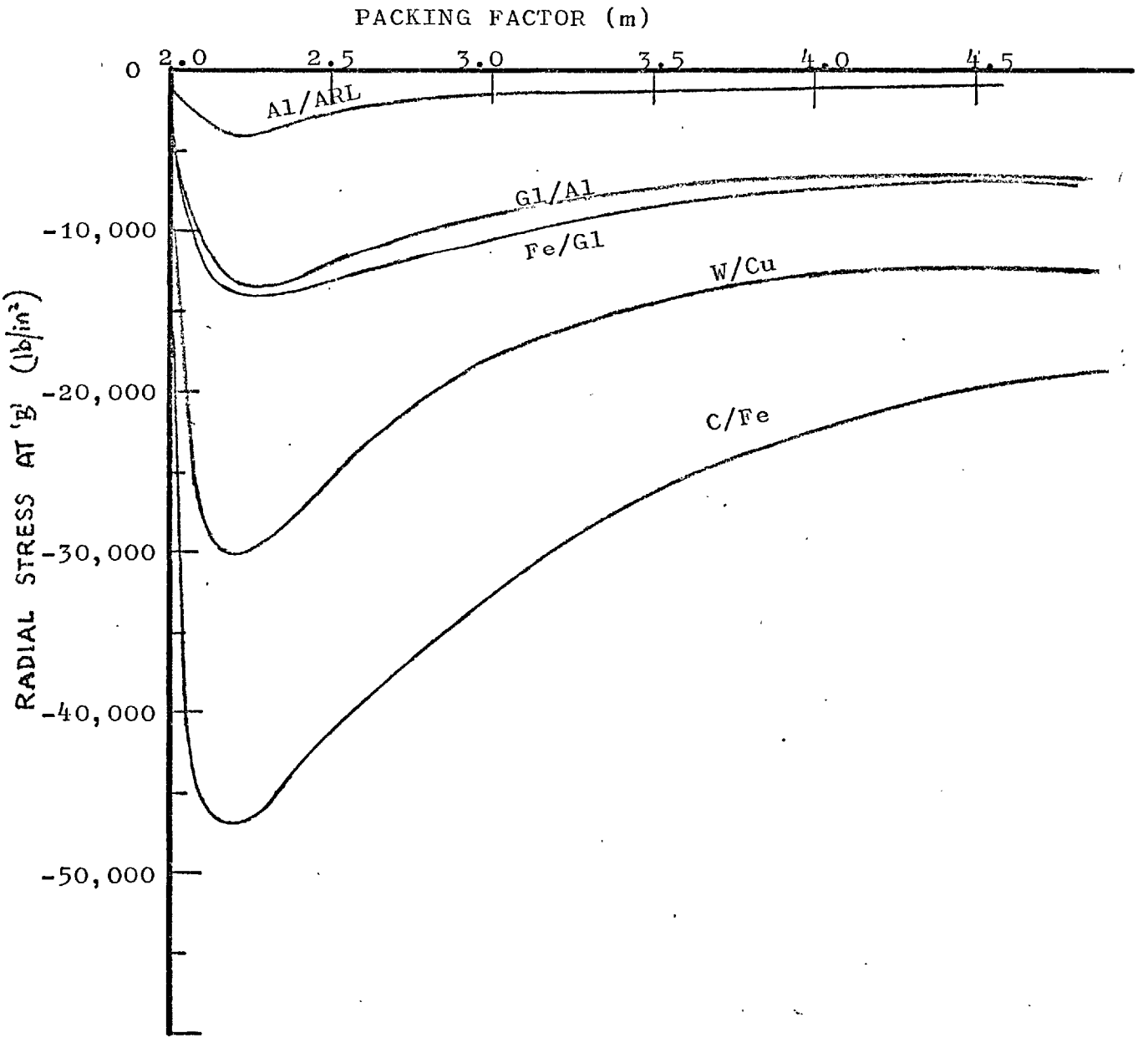

FIG. 3.6a: VARIATION OF RADIAL STRESS AT 'B' WITH PACKING FACTO

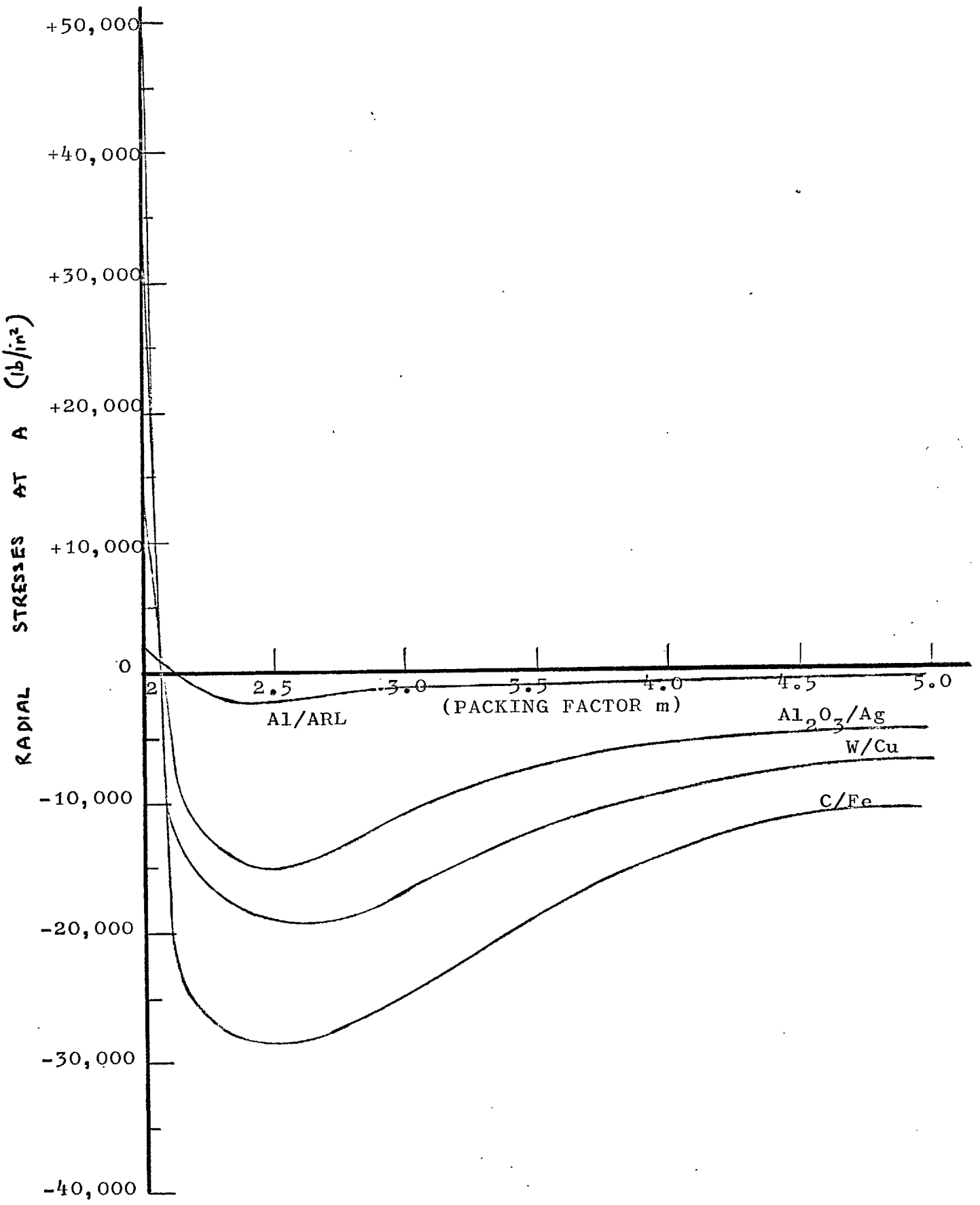

FIG. 6.6b: VARIATION OF RADIAL STRESS AT 'A' WITH PACKING FACTOR.

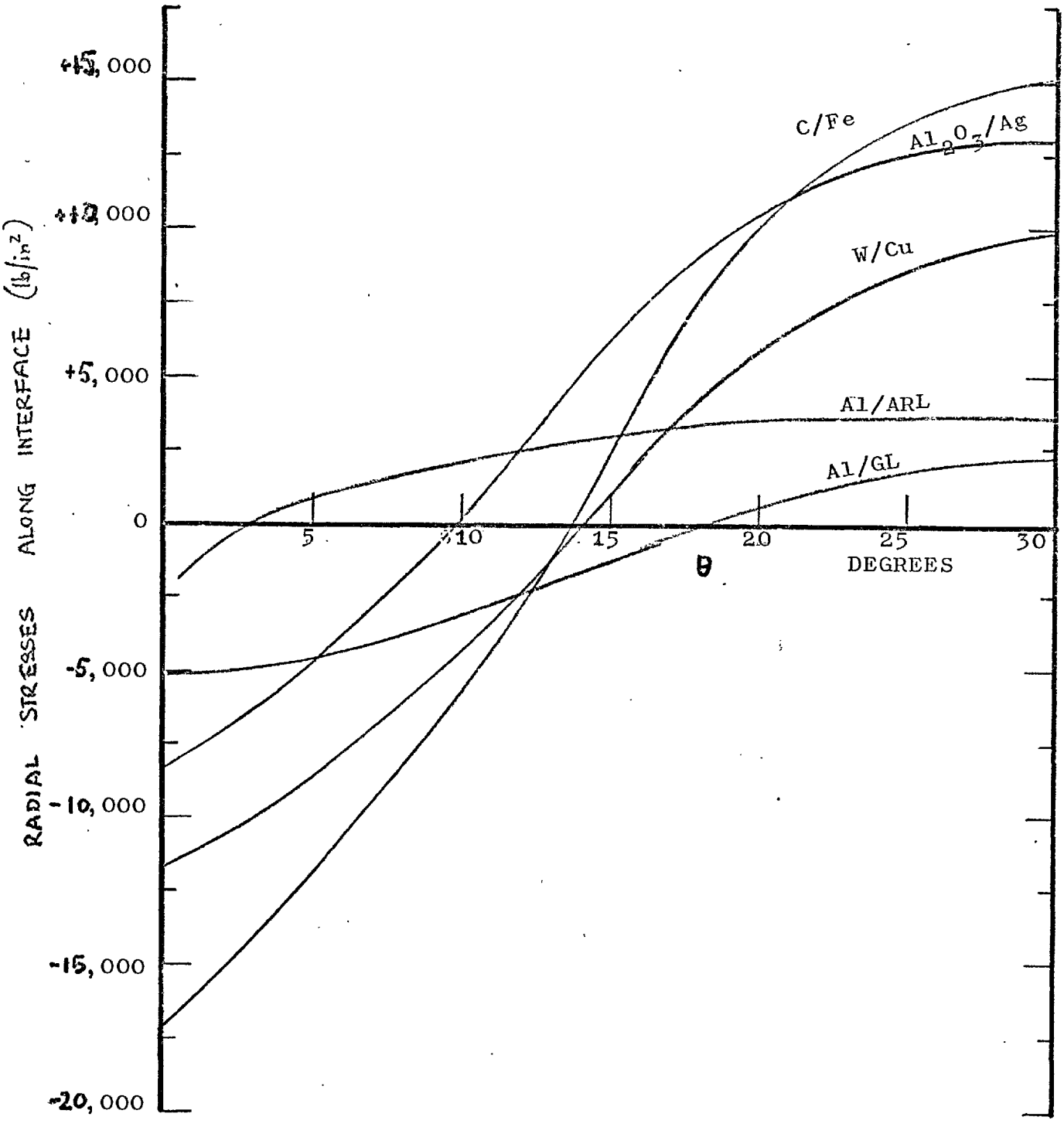

FIG. 3.7a: VARIATION OF RADIAL STRESSES ALONG INTERFACE FOR m=2.

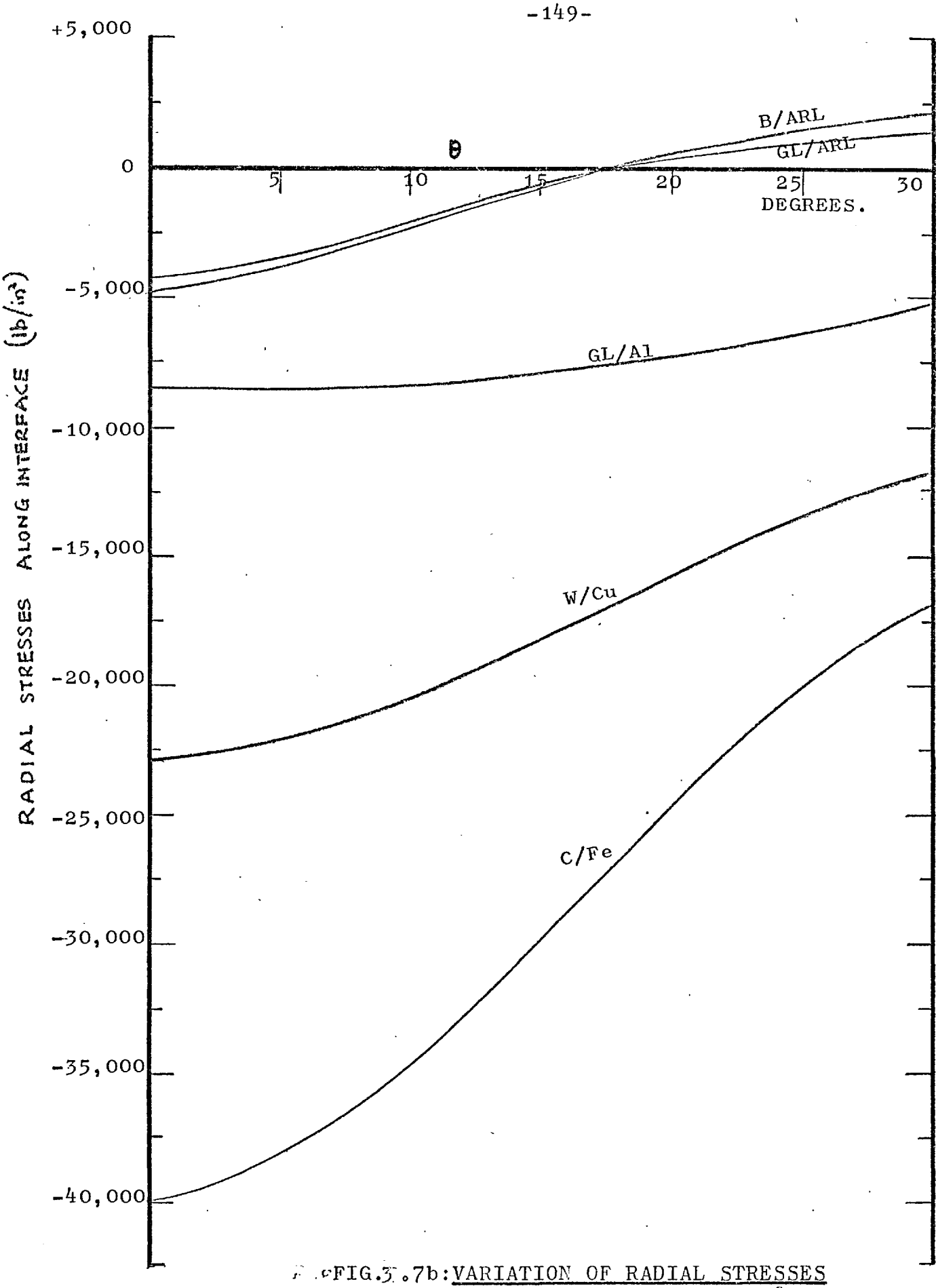

FIG.3.7b: VARIATION OF RADIAL STRESSES ALONG INTERFACE FOR m=2.08.

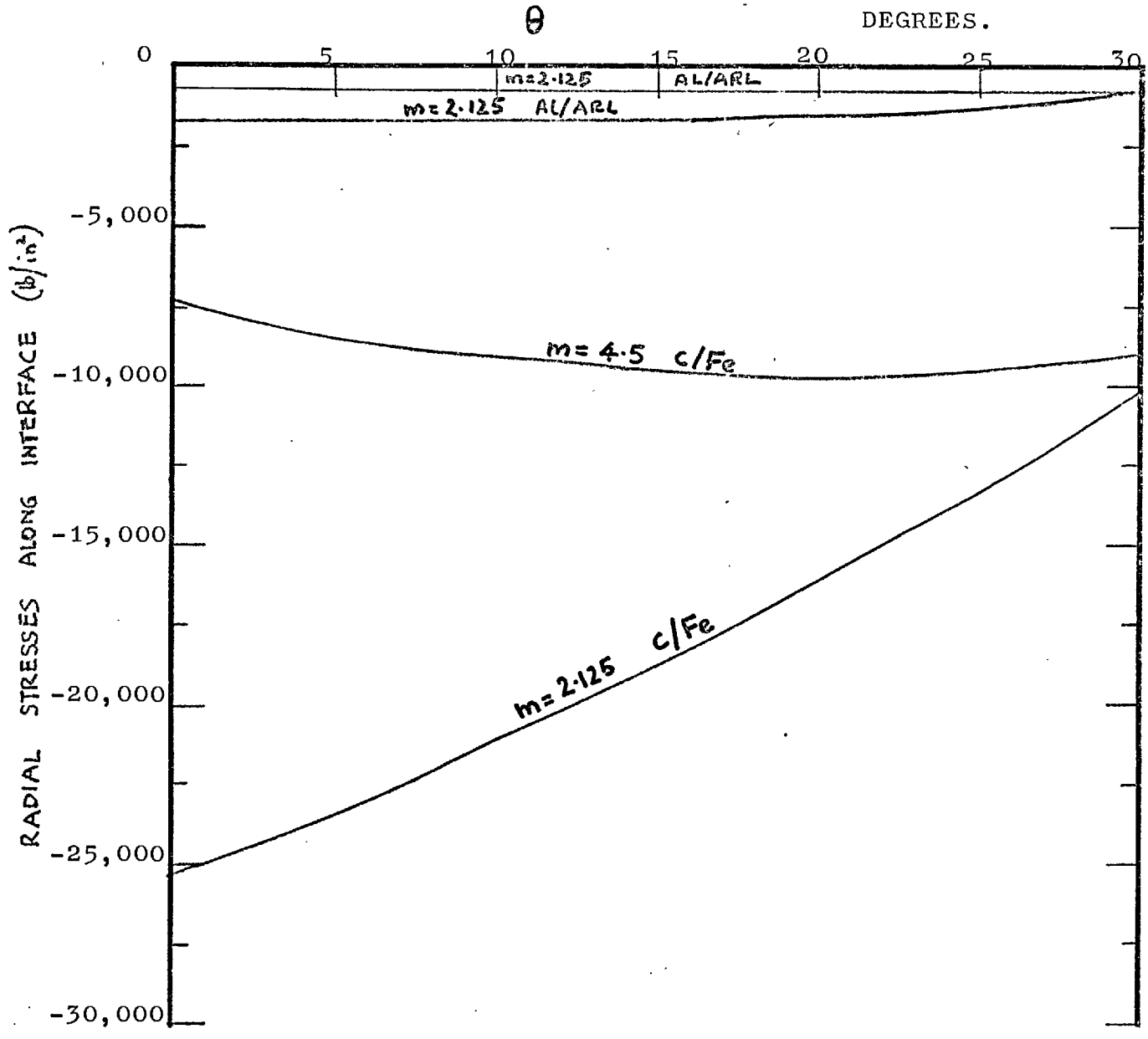

FIG. 3.7c: VARIATION OF RADIAL STRESSES ALONG INTERFACE FOR m=2.125 AND m=4.5. FOR Al/ARL and C/Fe SYSTEMS.

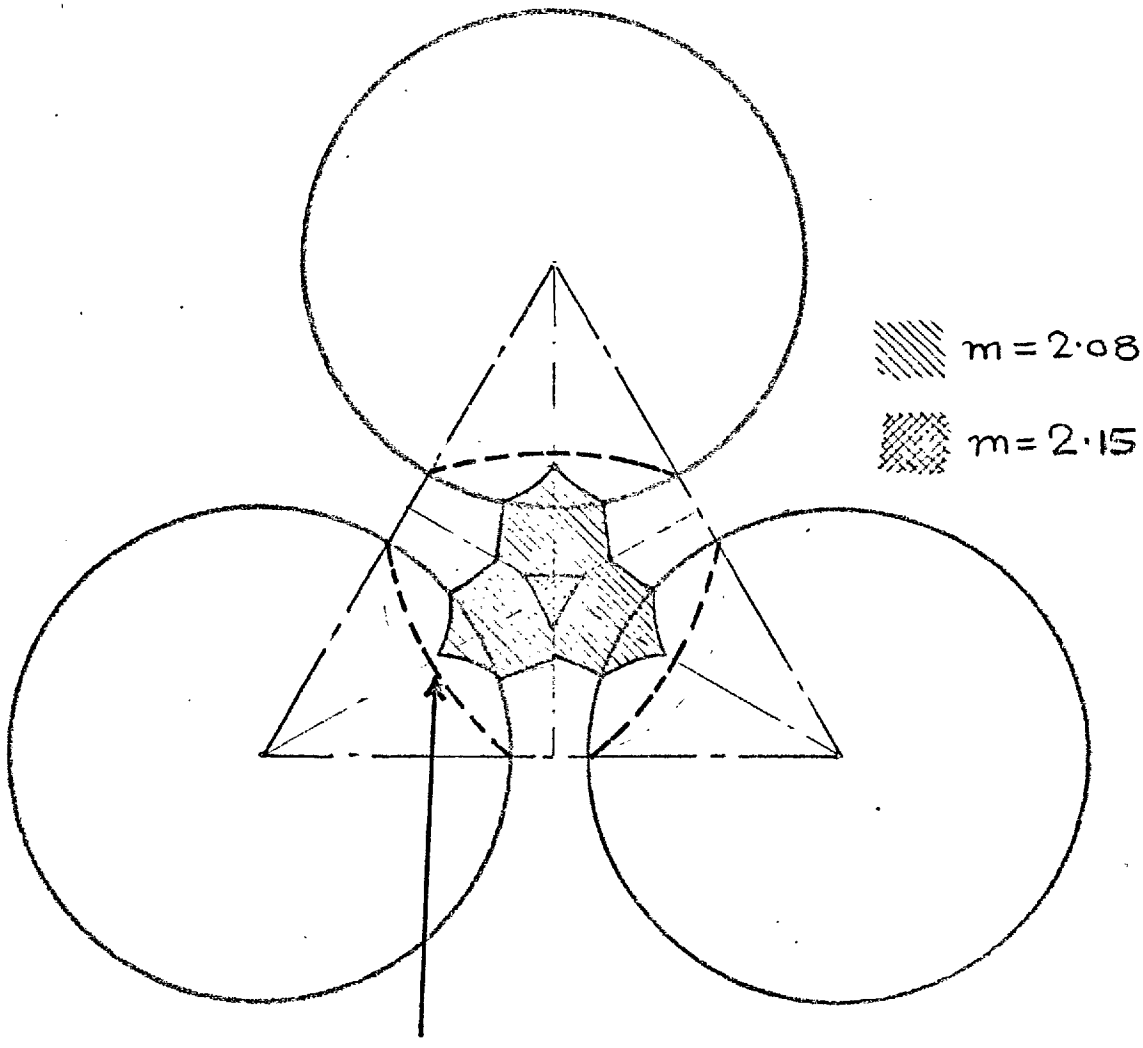

FIG.3.8a: REGION EXPOSED TO TENSILE RADIAL STRESS FOR CLOSELY SPACED FIBRES FOR GLASS/ARALDITE SYSTEM.

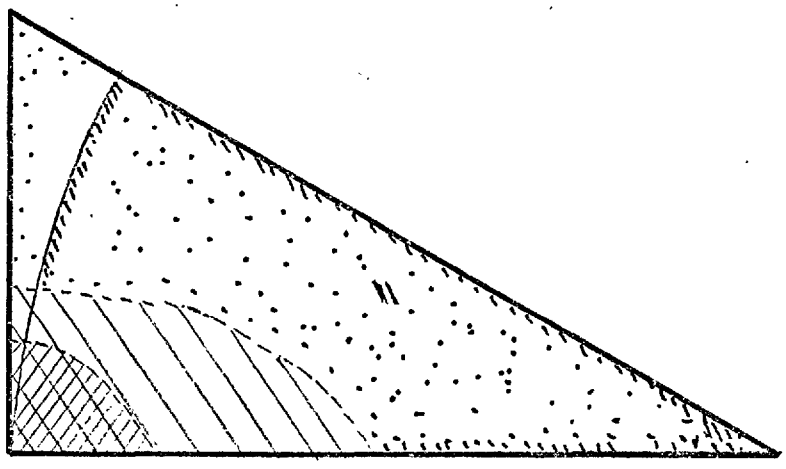

TENSION

REGION IN COMPRESSION FOR C/Fe SYSTEM

REGION IN COMPRESSION FOR Al_2O_3/Ag SYSTEM

FIG. 3.8b: RADIAL STRESS DISTRIBUTION FOR FIBRES TOUCHING.

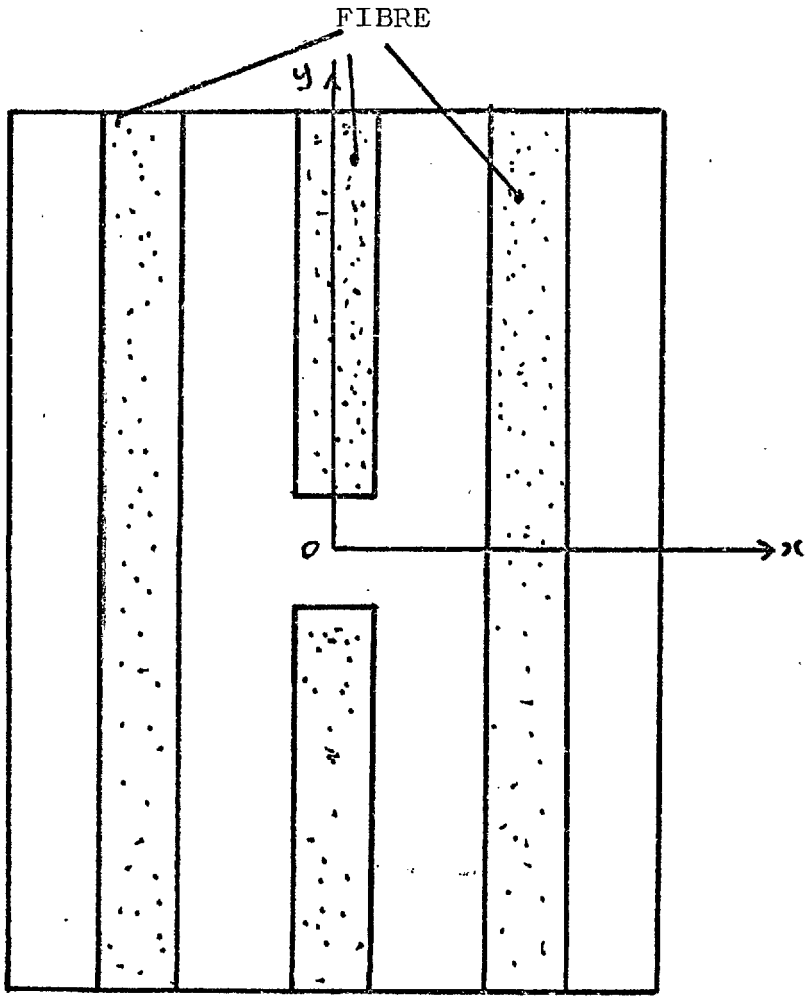

(a). LONGITUDINAL SECTION

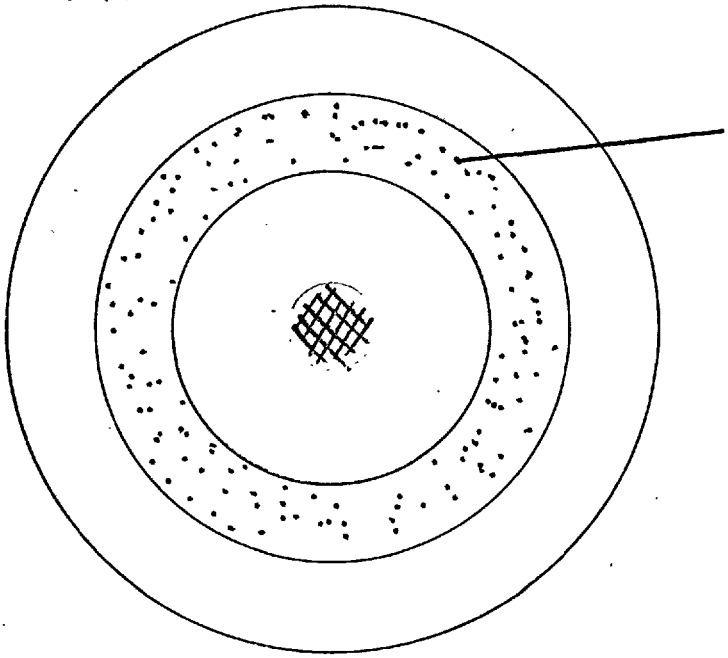

(b). PLAN VIEW

FIG.4.1: PLANE AND AXISYMMETRIC MODEL FOR FINITE ELEMENT ANALYSIS.

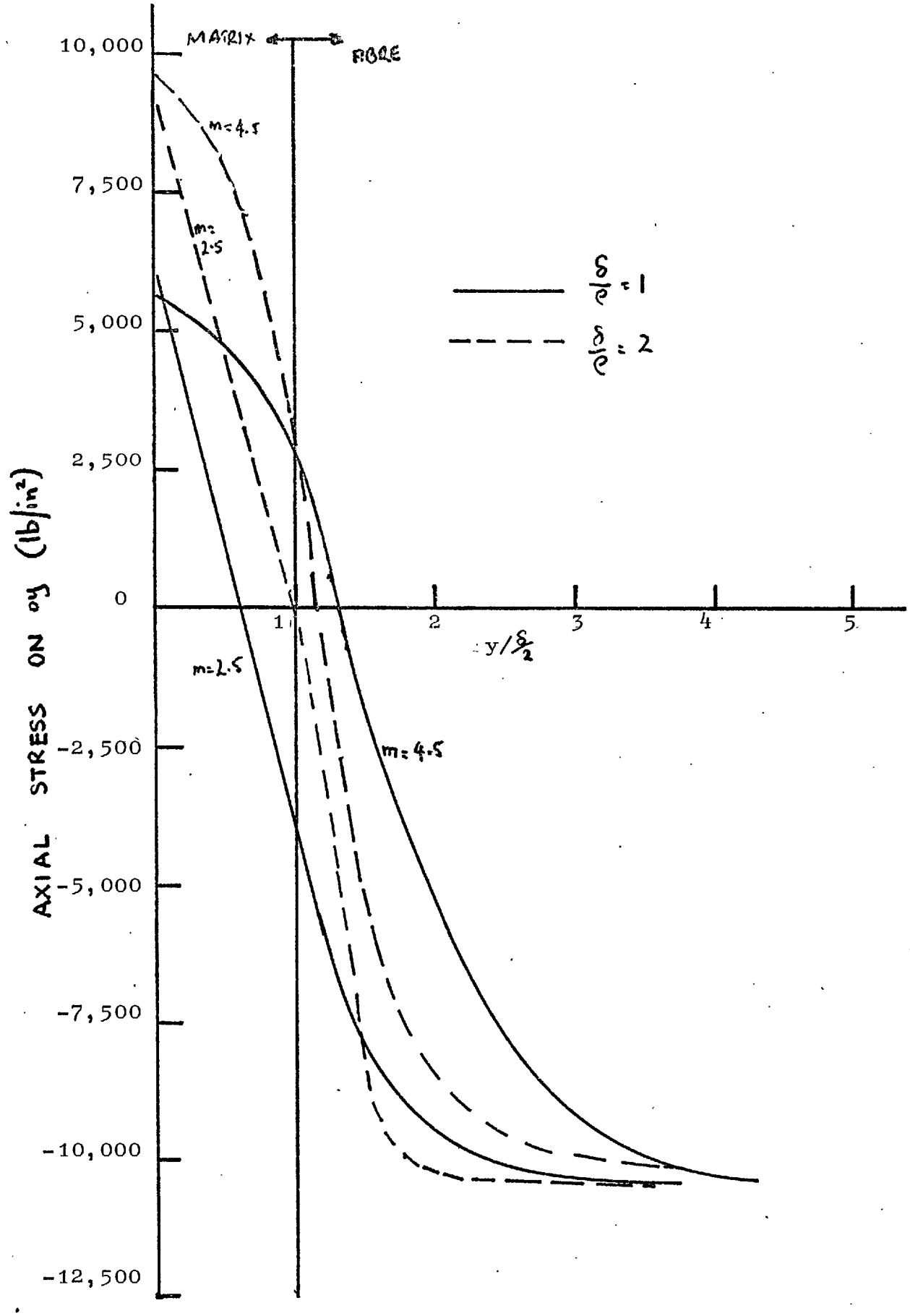

FIG.4.2a: AXIAL STRESS DISTRIBUTION ALONG CENTRE LINE σy FOR C/Fe FOR PLANE MODEL.

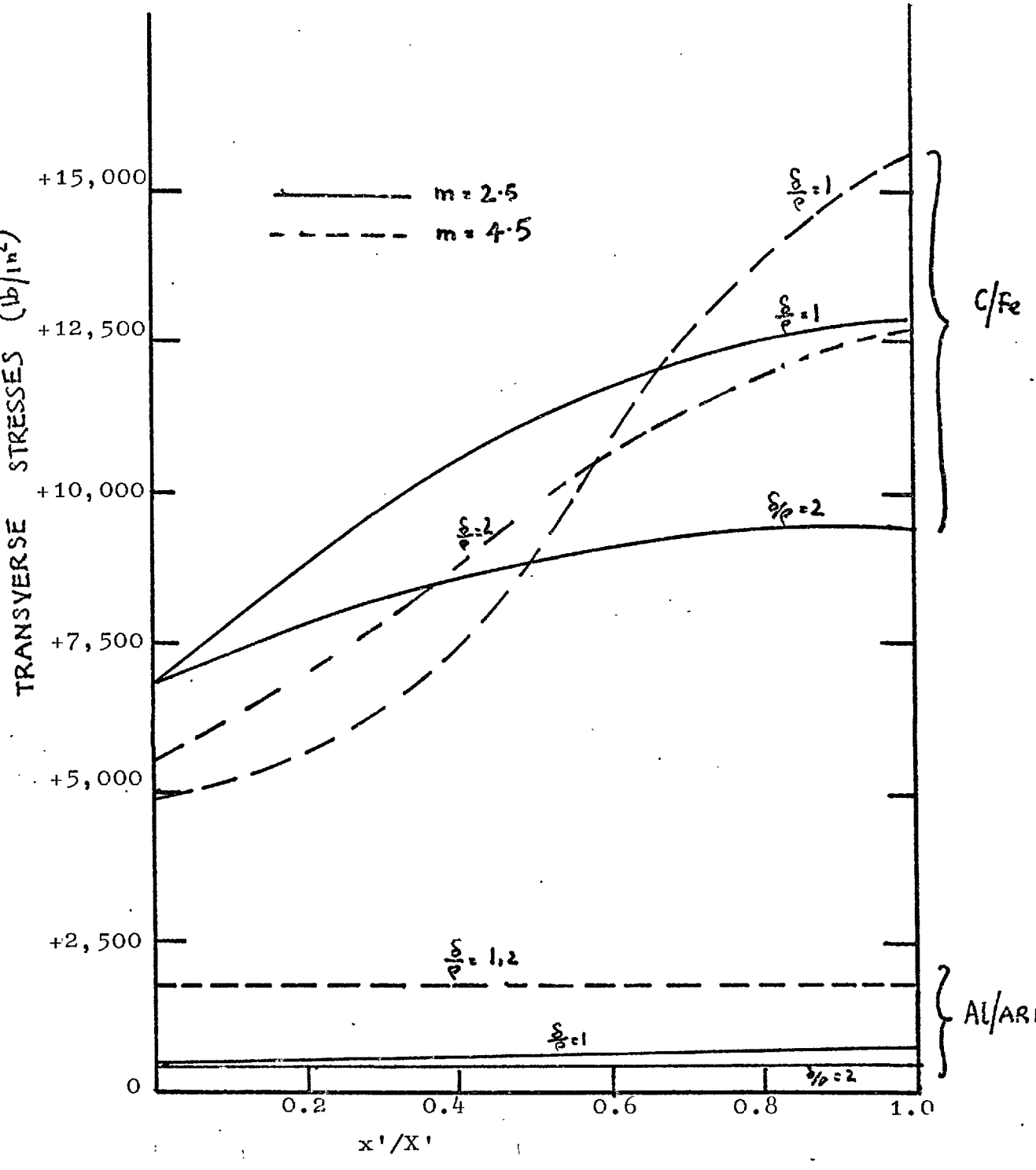

FIG.4.2b: MATRIX TRANSVERSE STRESS VARIATION ON ox' (FIG.7.4) FOR PLANE MODEL.

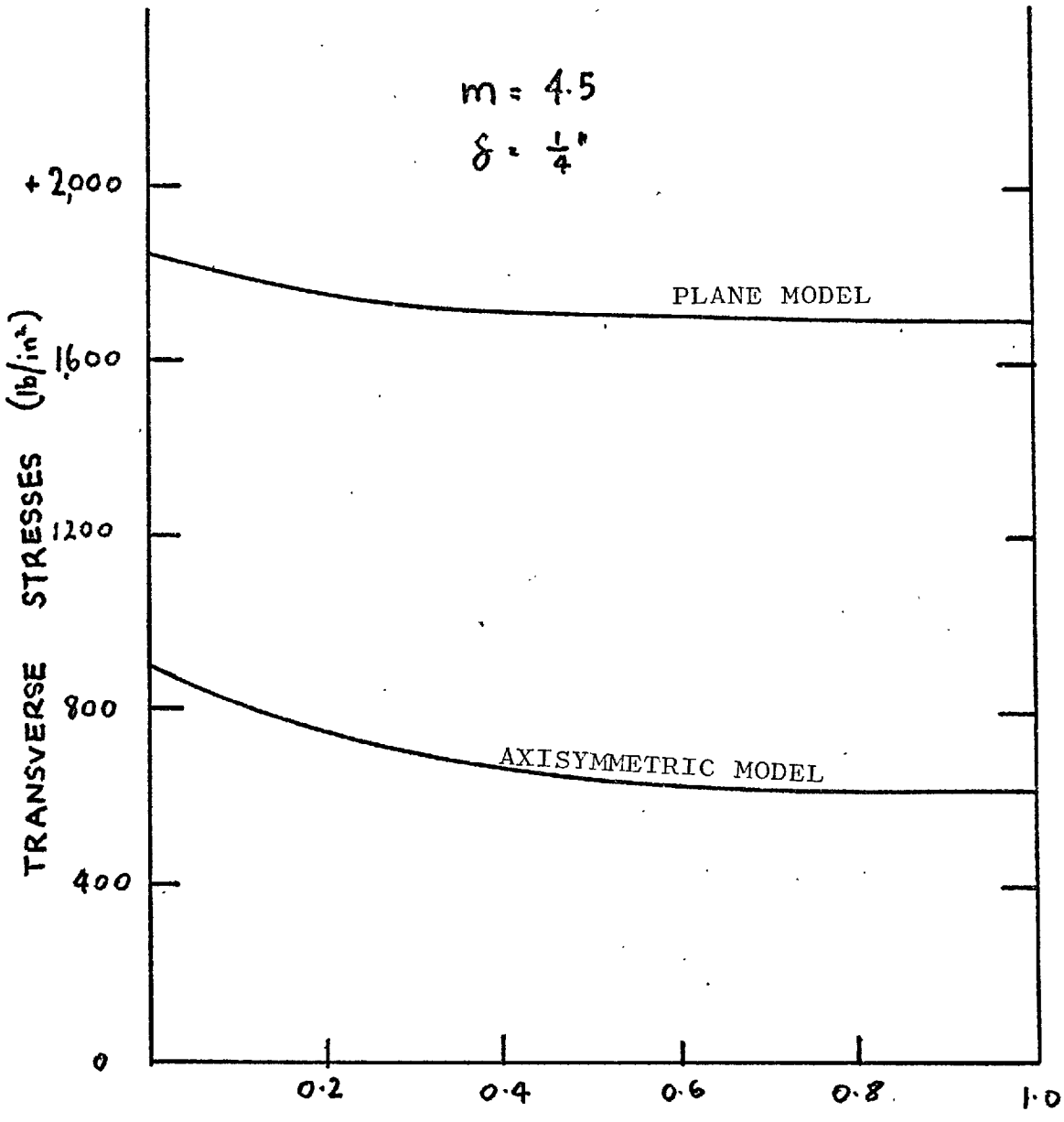

FIG.4.2c: MATRIX TRANSVERSE STRESS VARIATION ON σ'_x (FIG.7.4) FOR Al/ARL SYSTEM: A COMPARISON BETWEEN PLANE AND AXISYMMETRIC MODEL RESULTS.

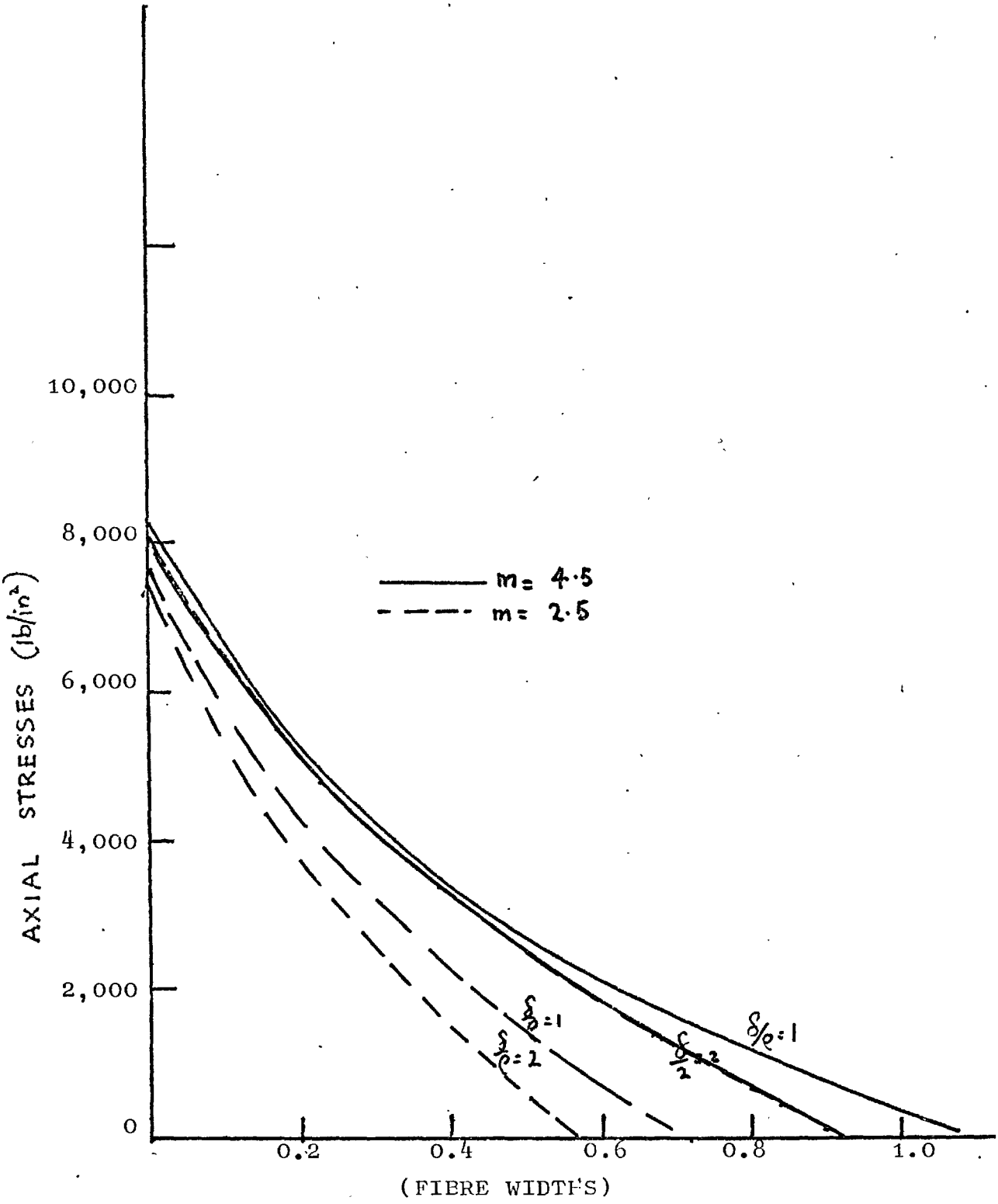

FIG. 4.2d: SHEAR STRESS VARIATION ALONG FIBRE FOR C/Fe SYSTEM FOR PLANE MODEL.

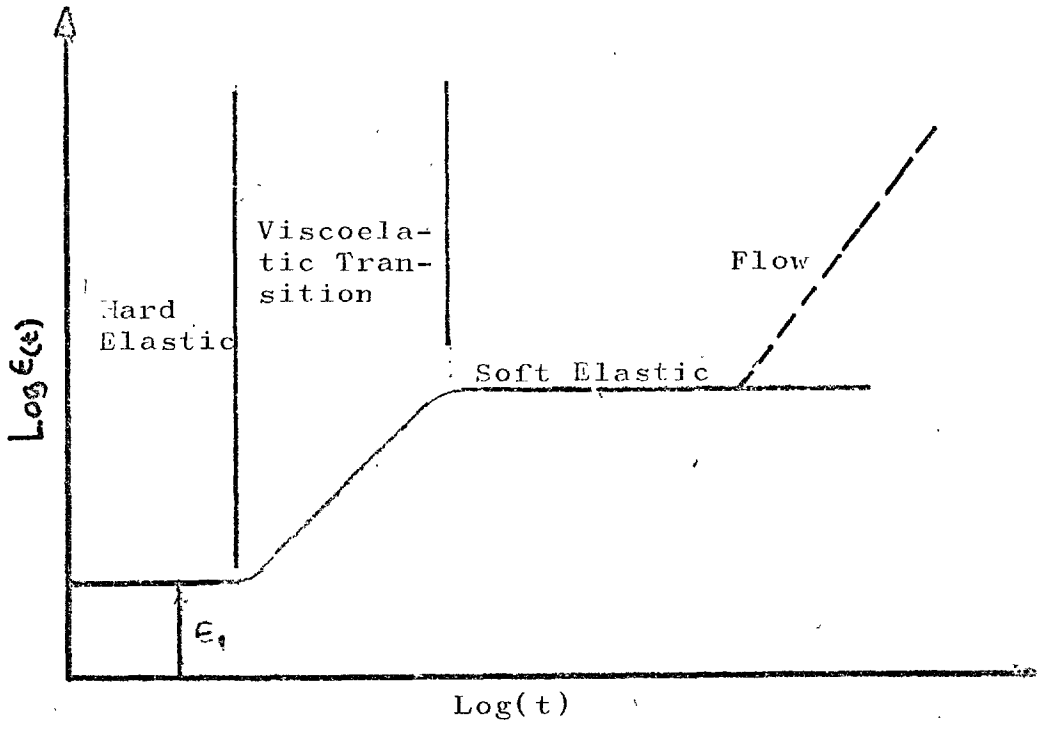

FIG.5.1a: TYPICAL CREEP CURVE OF A POLYMER.

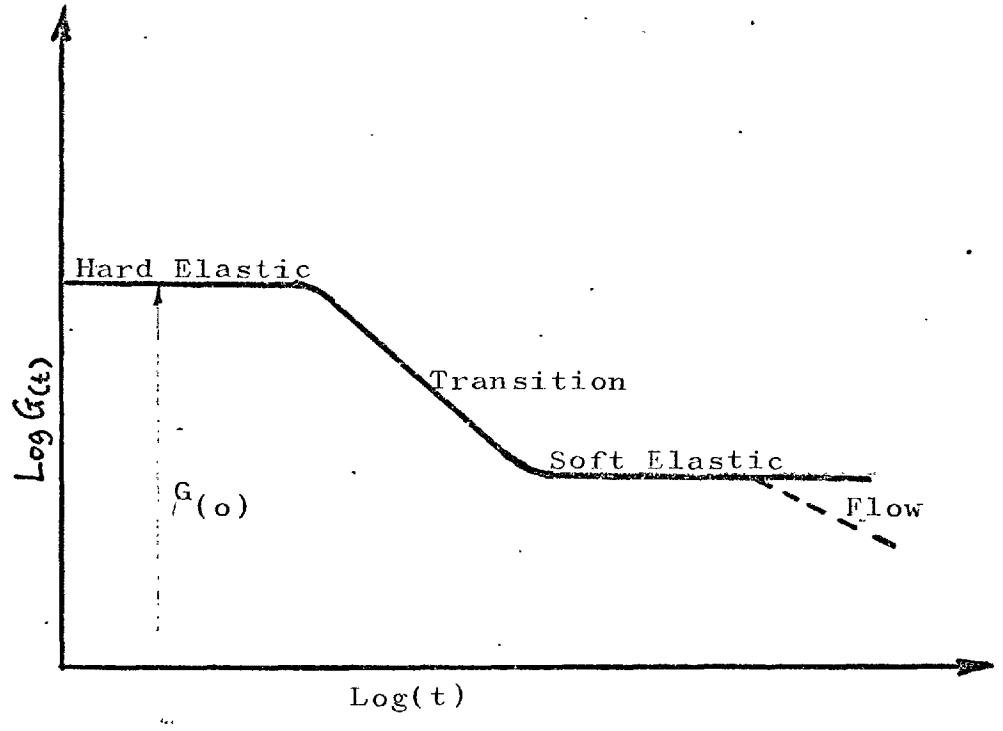

FIG.5.1b: TYPICAL STRESS RELAXATION CURVE OF A POLYMER

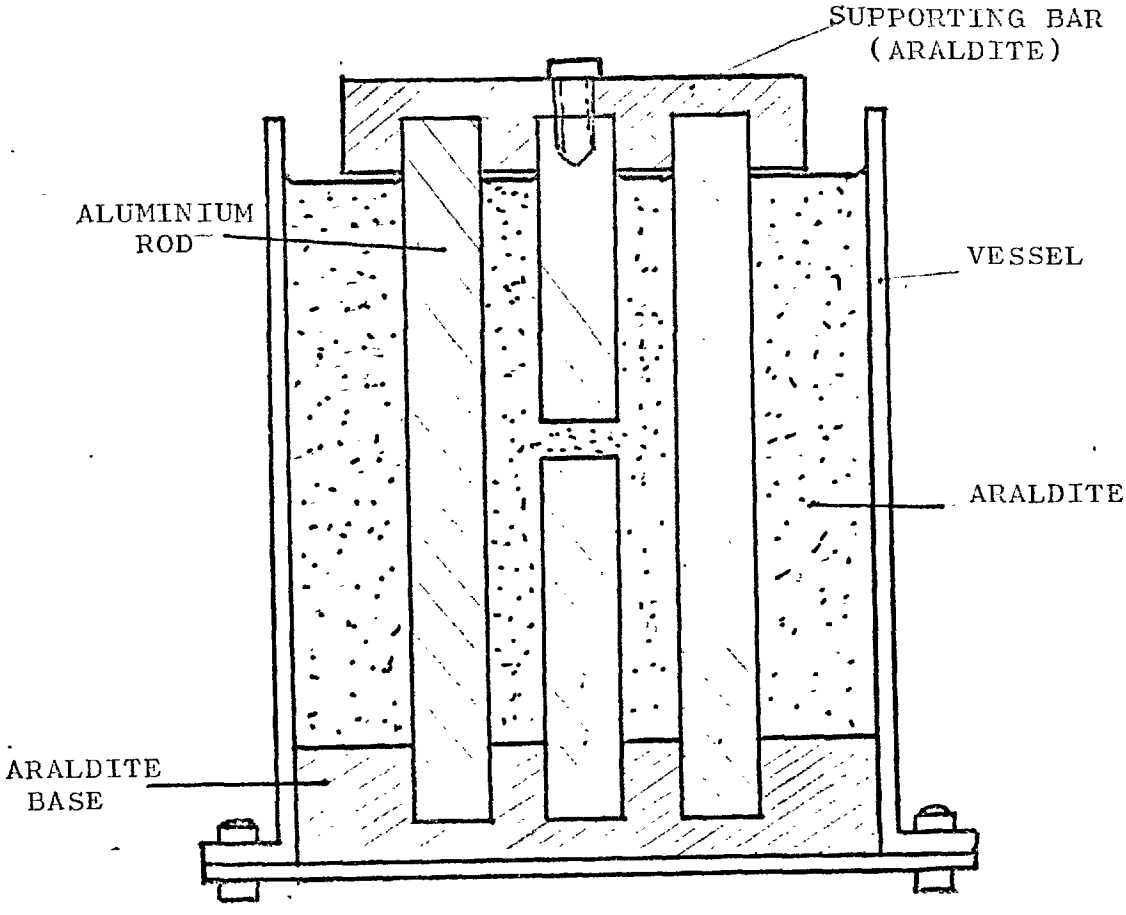

FIG.6.1: SECTION THROUGH MOULD

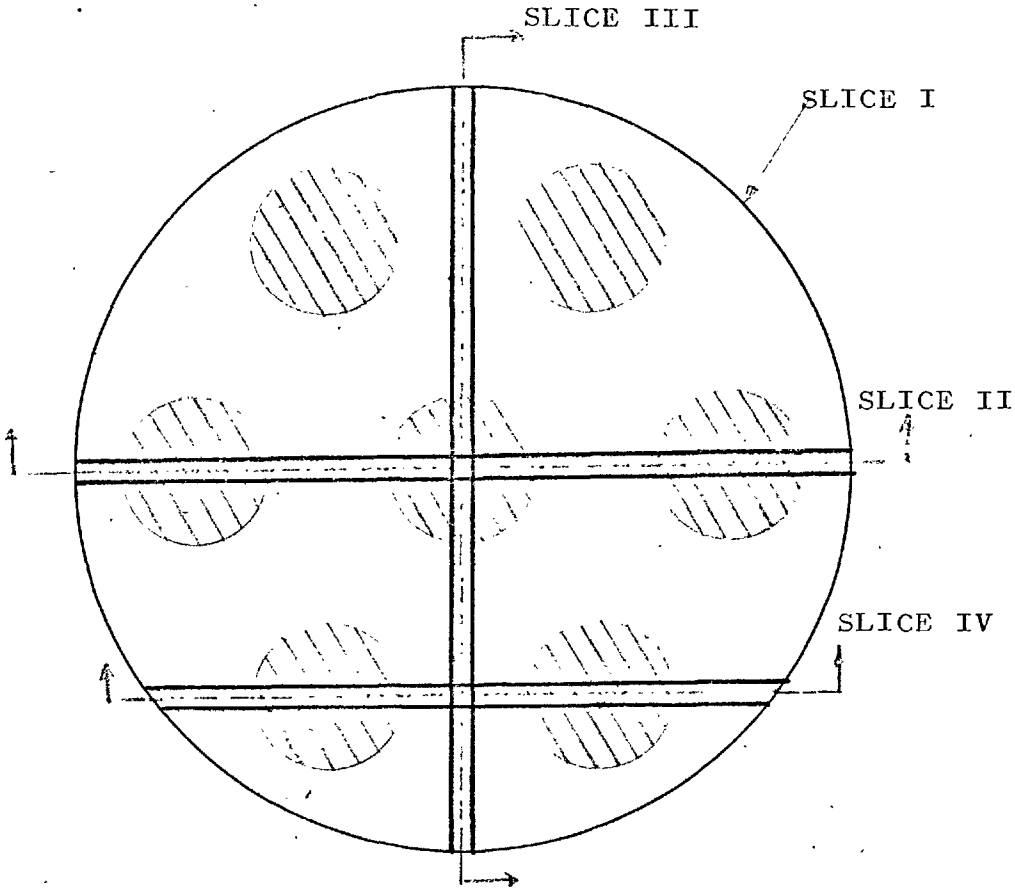

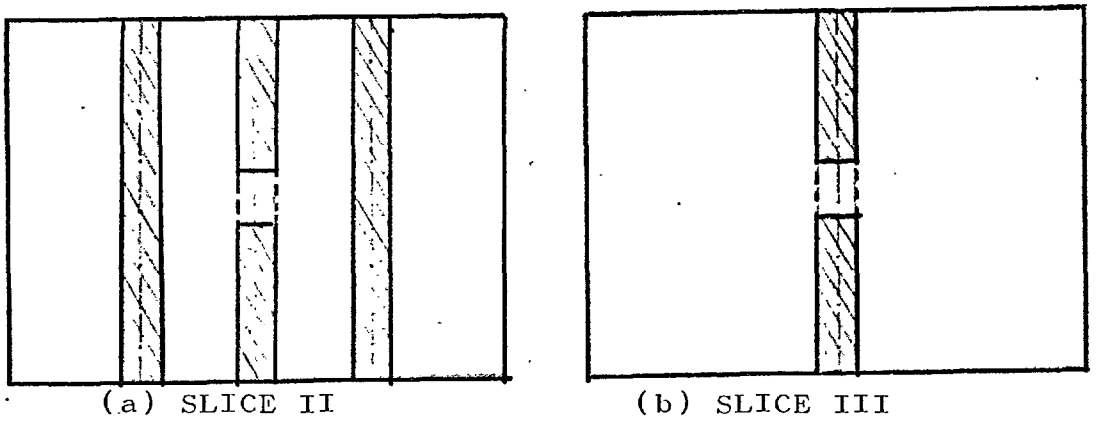

(a) SLICE II

(b) SLICE III

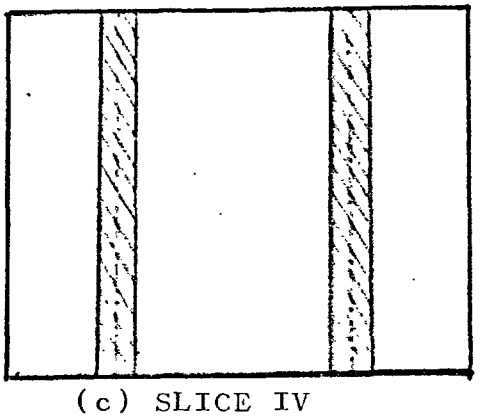

(c) SLICE IV

FIG.6.2: LOCATION OF PLANES FOR PHOTOELASTIC SLICES

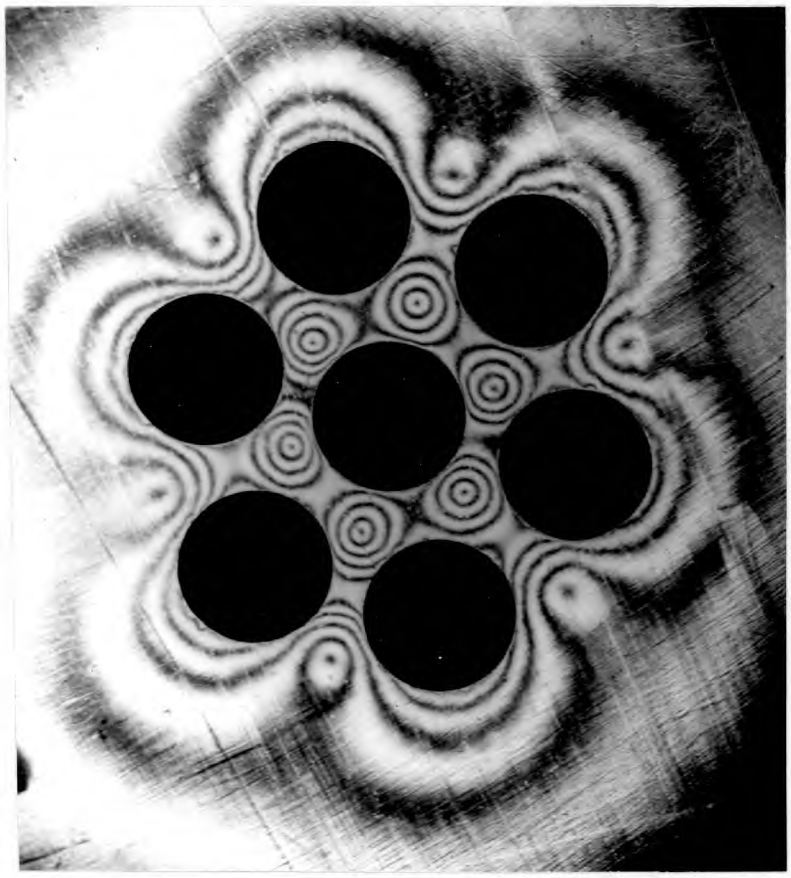

FIG.6.3a: TYPICAL ISOCHROMATICS FROM SLICE I ($m=2.5$, $\delta=0$)

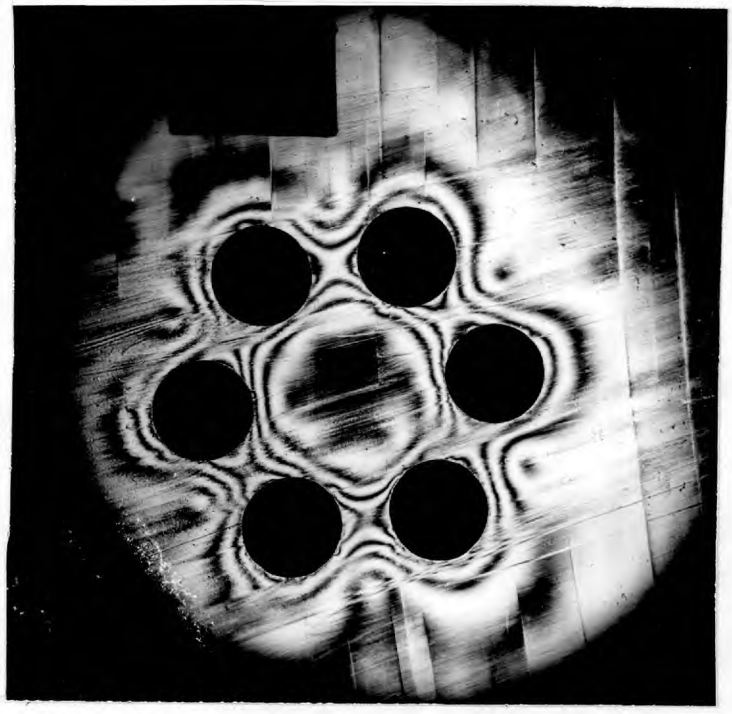

FIG.6.3b: TYPICAL ISOCHROMATICS FROM SLICE I ($m=3$, $\delta=\frac{1}{2}$). CENTRAL DARK REGION IS ISOTROPIC.

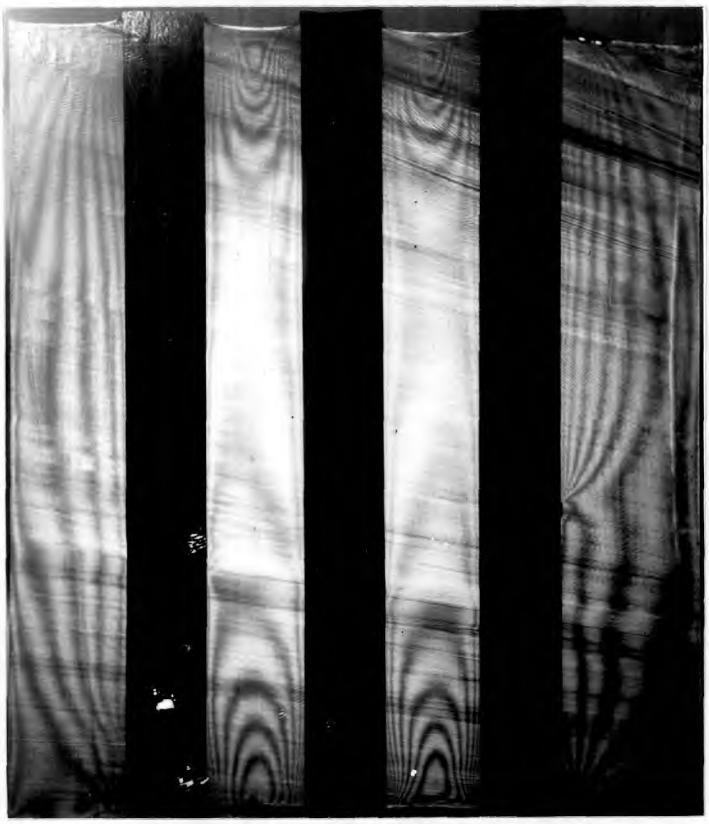

FIG6.3c: TYPICAL ISOCHROMATICS FROM SLICE II FOR CONTINUOUS RODS ($m=4.5$, $\S=0$).

FIG.6.3d: POLISHED SLICE FROM FIG.6.3c. ABOVE.

FIG.6.3e: TYPICAL ISOCHROMATICS FROM SLICE II FOR DICCNTINUOUS ROD ($m=4.5$, $\delta=\frac{1}{2}$), NOTE POSITION OF ISOTROPIC FOINTS.

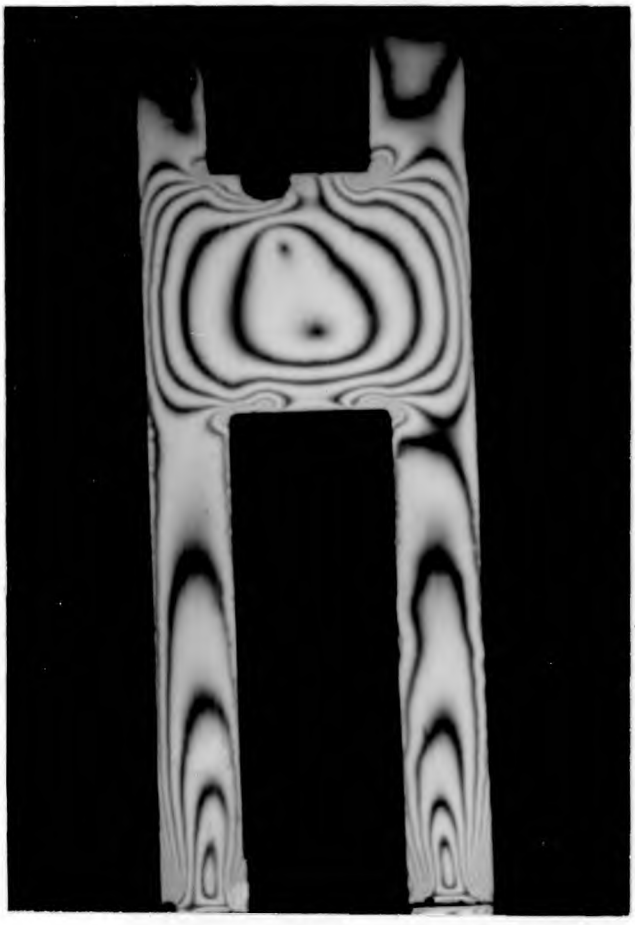

FIG.6.3f: ISOCHROMATICS FROM SLICE II FOR DISCONTINUOUS ROD ($m=3$, $\delta=\frac{3}{4}$). NOTE POSITION OF ISOTROPIC POINTS.

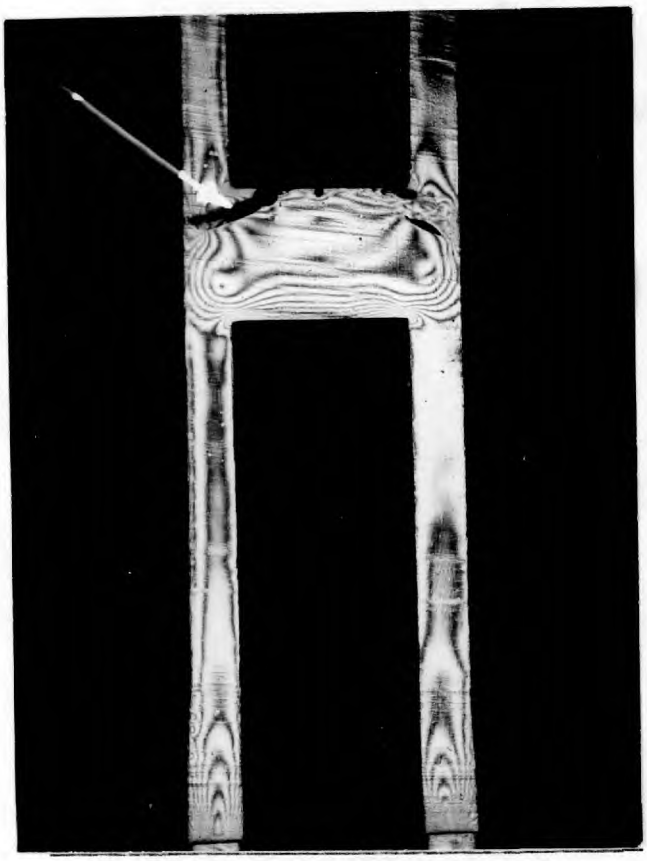

FIG.6.3g: ISOCHROMATICS FROM SLICE II FOR DISCONTINUOUS ROD (m=2.5, $\delta=\frac{1}{2}$). ARROW SHOWS CRACK.

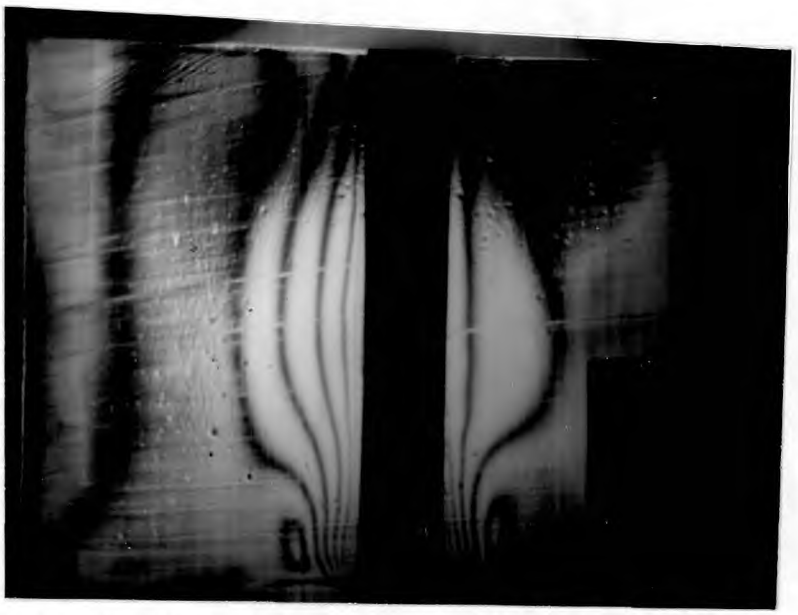

FIG.6.3h: TYPICAL ISOCHROMATICS FROM SLICE III FOR CONTINUOUS RODS ($m=3, \delta=0$).

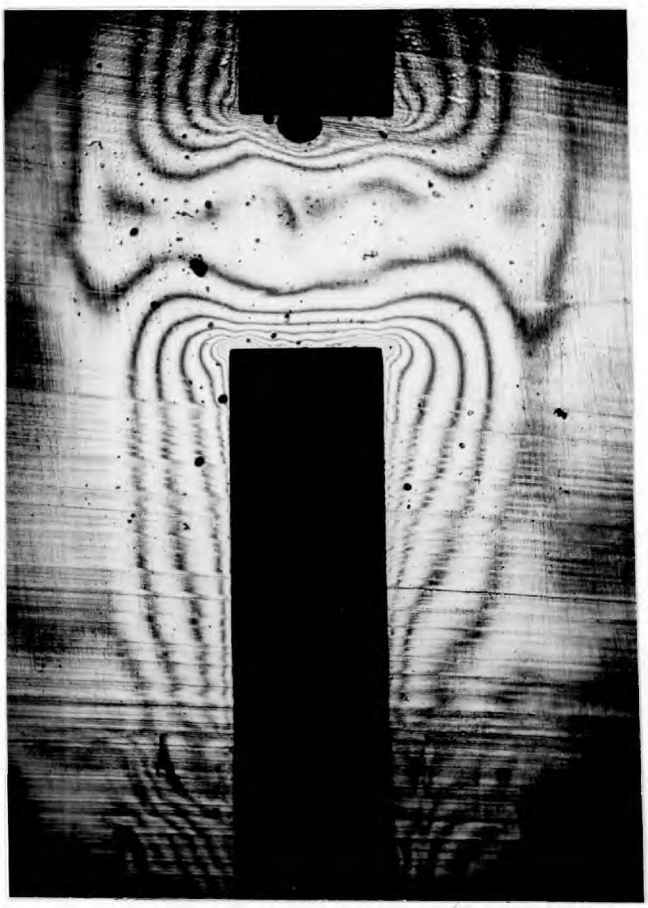

FIG.6.3i: TYPICAL ISOCHROMATICS FROM SLICE III FOR DISCONTINUOUS ROD ($m=3, \delta=\frac{3}{4}$).

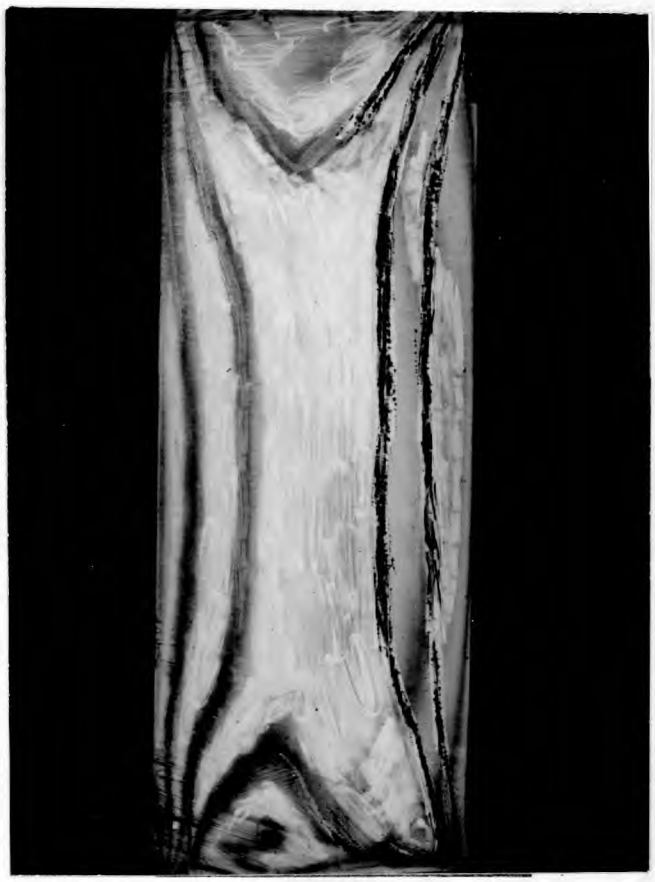

FIG.6.3j: TYPICAL ISOCHROMATICS FROM SLICE IV.

N.B. PICTURE HAD TO BE TOUCHED UP TO BRING OUT DARK FRINGES.

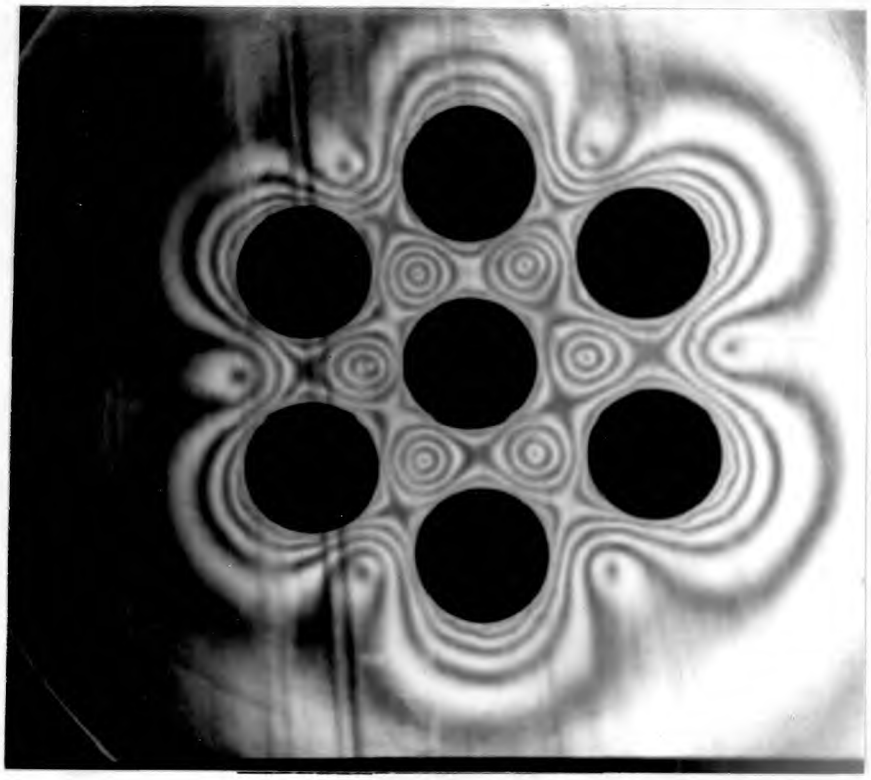

(a) SEVEN RODS

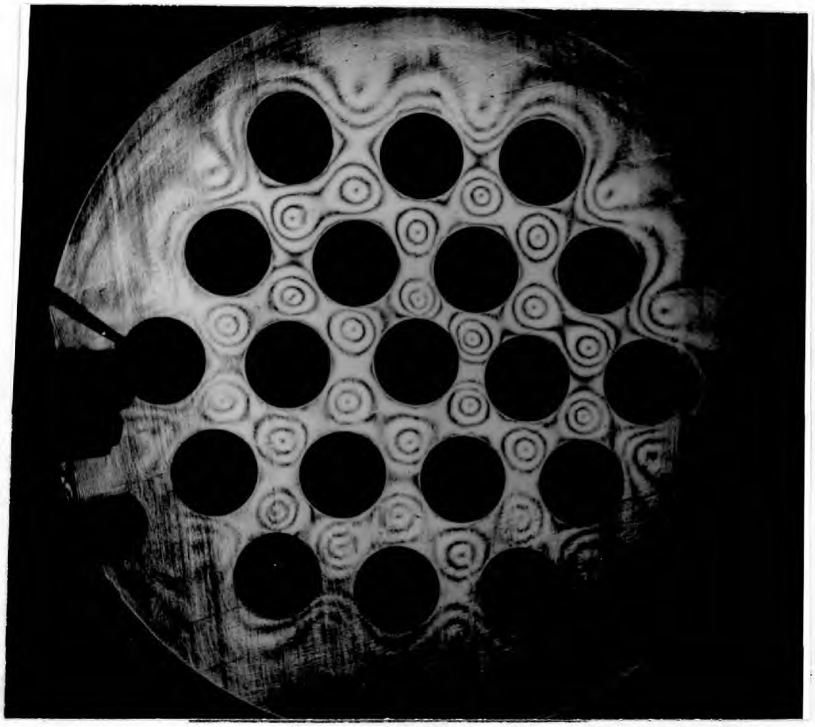

(b) NINETEEN RODS

FIG.6.4: COMPARISON OF FRINGES FOR 7-ROD AND 19-ROD ARRANGEMENTS, (m=3, δ=0).

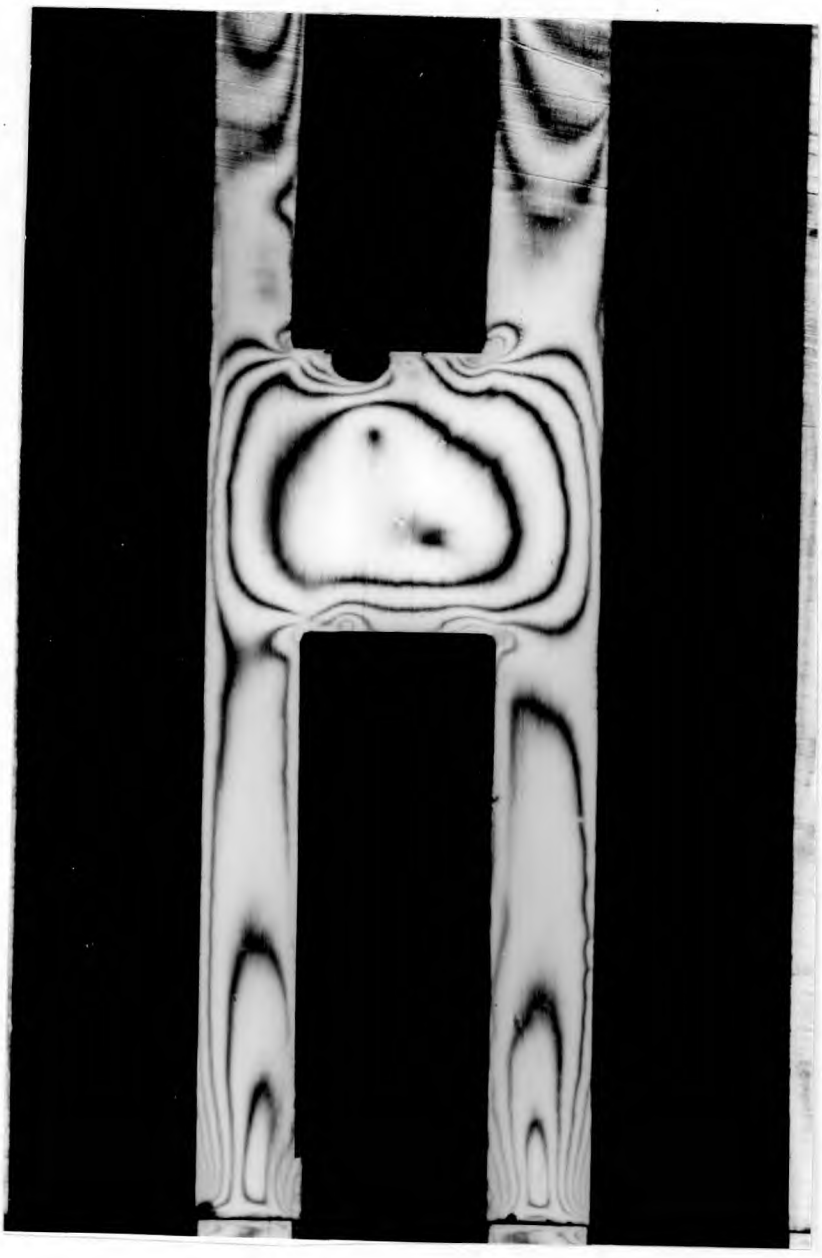

FIG.6.5: ISOCHROMATICS FROM SLICE II ($m=3, \delta=\frac{3}{4}$) AFTER SIX MONTHS STORAGE SHOWING LOSS OF FRINGES (cf FIG.6.3f)

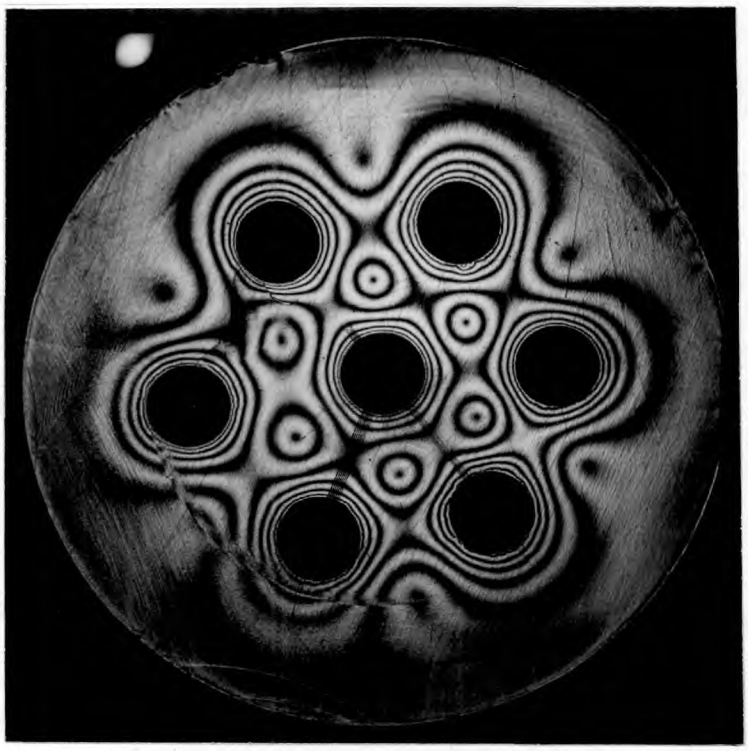

FIG.6.6a: TOTAL FRINGES IN SLICE II ($m=4.5, \delta=0$)

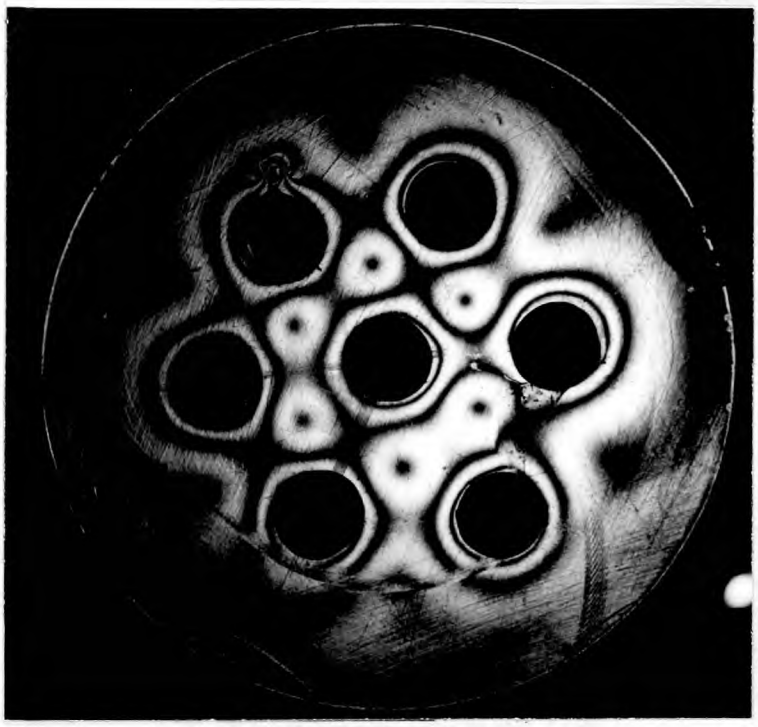

FIG.6.6b: RESIDUAL FRIGES AFTER REMOVING DISCS FROM SLICE I ($m=4.5, \delta=0$)

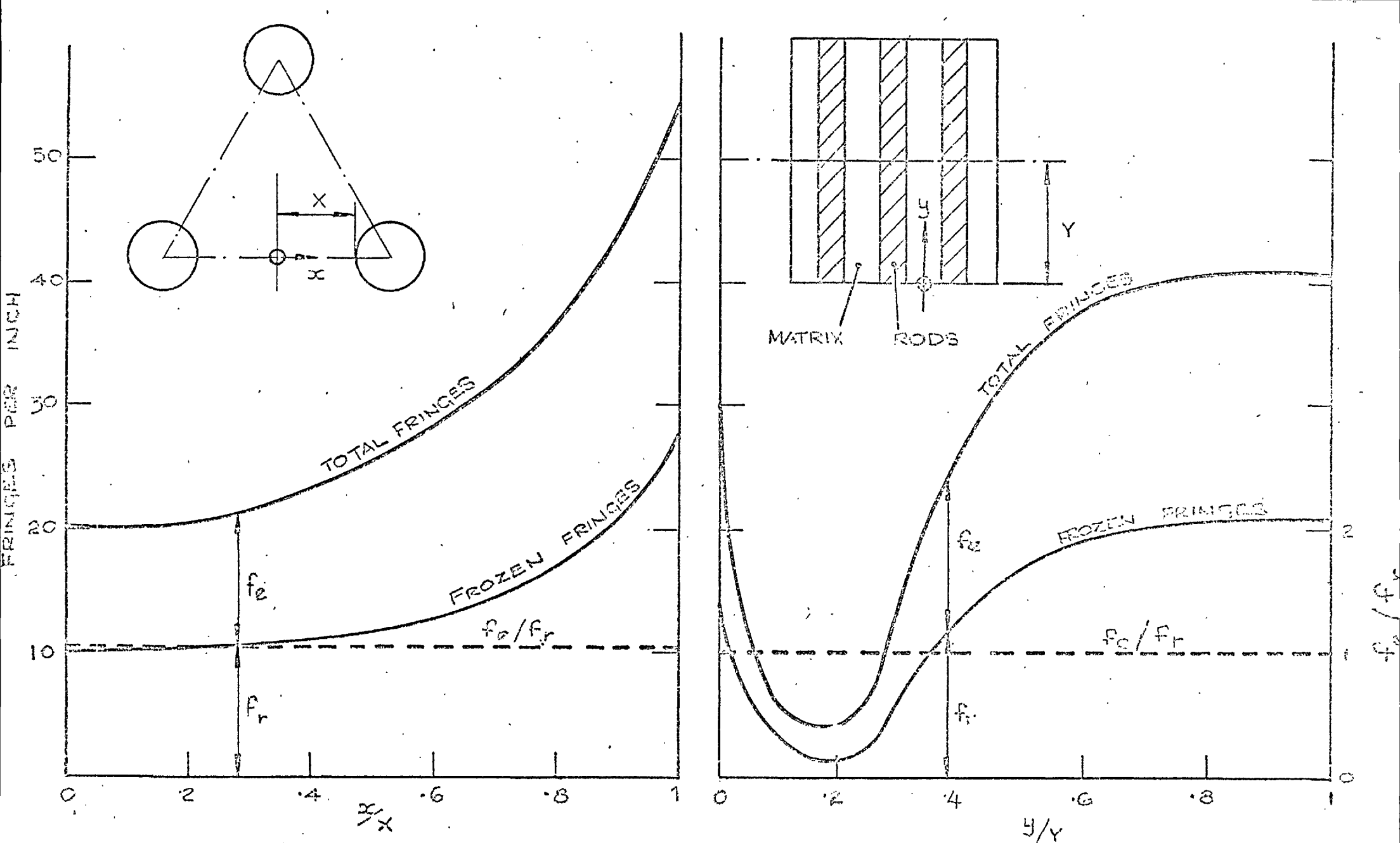

(a) TRANSVERSE SLICE I

(b) MERIDIONAL SLICE. II

FIG 6·7 DISTRIBUTION OF FRINGES IN TRANSVERSE AND MERIDIONAL SLICES, BEFORE AND AFTER REMOVING

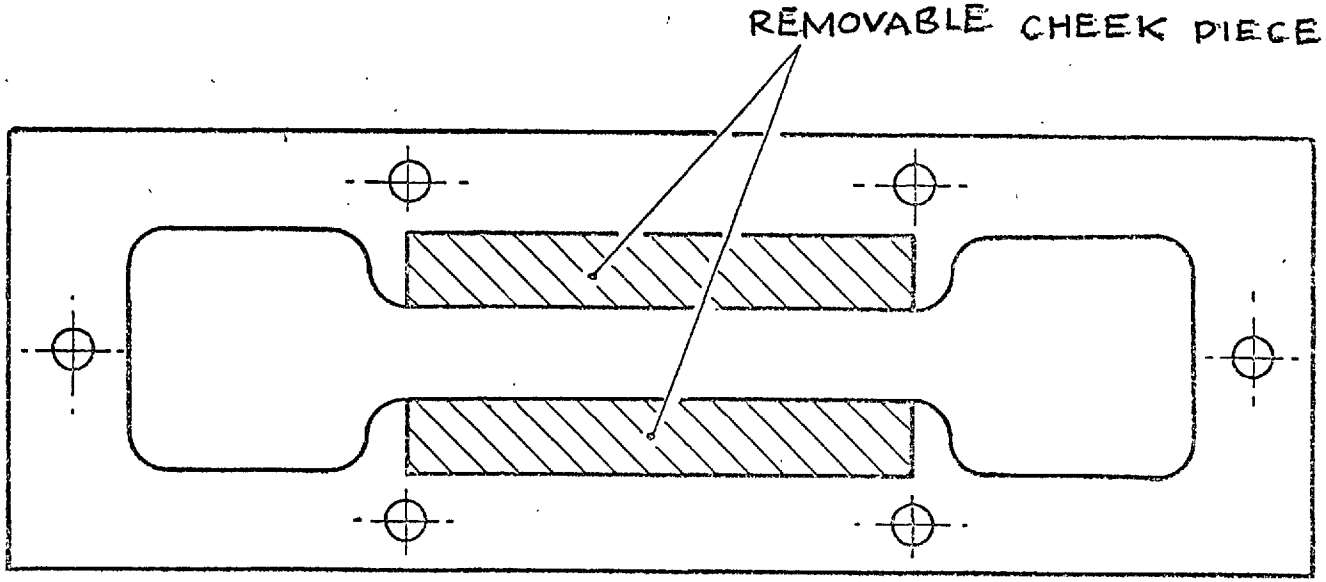

FIG 6·8 CALIBRATION MOULD.

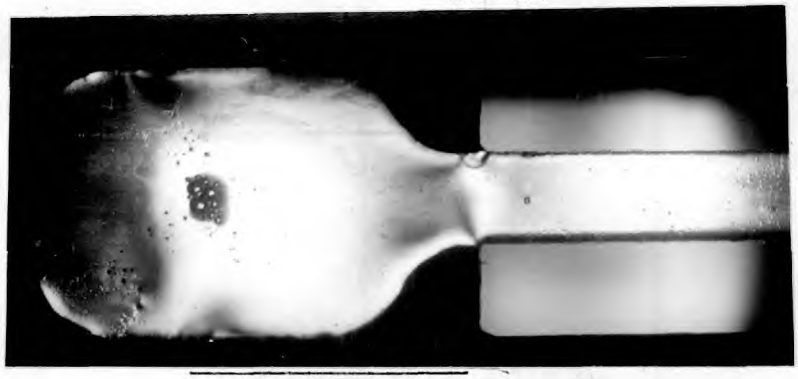

(a) 110°C

(b) 90°C

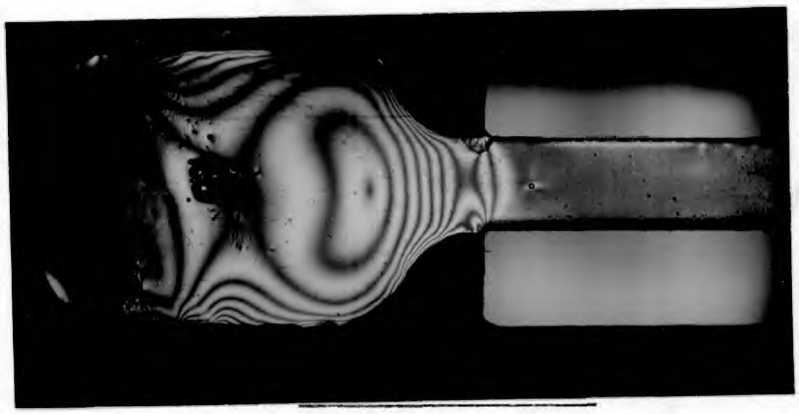

(c) 80°C

(d) 70°C

FIG.6.9: ISOCHROMATICS IN CALIBRATION MOULD DURING COOLING.

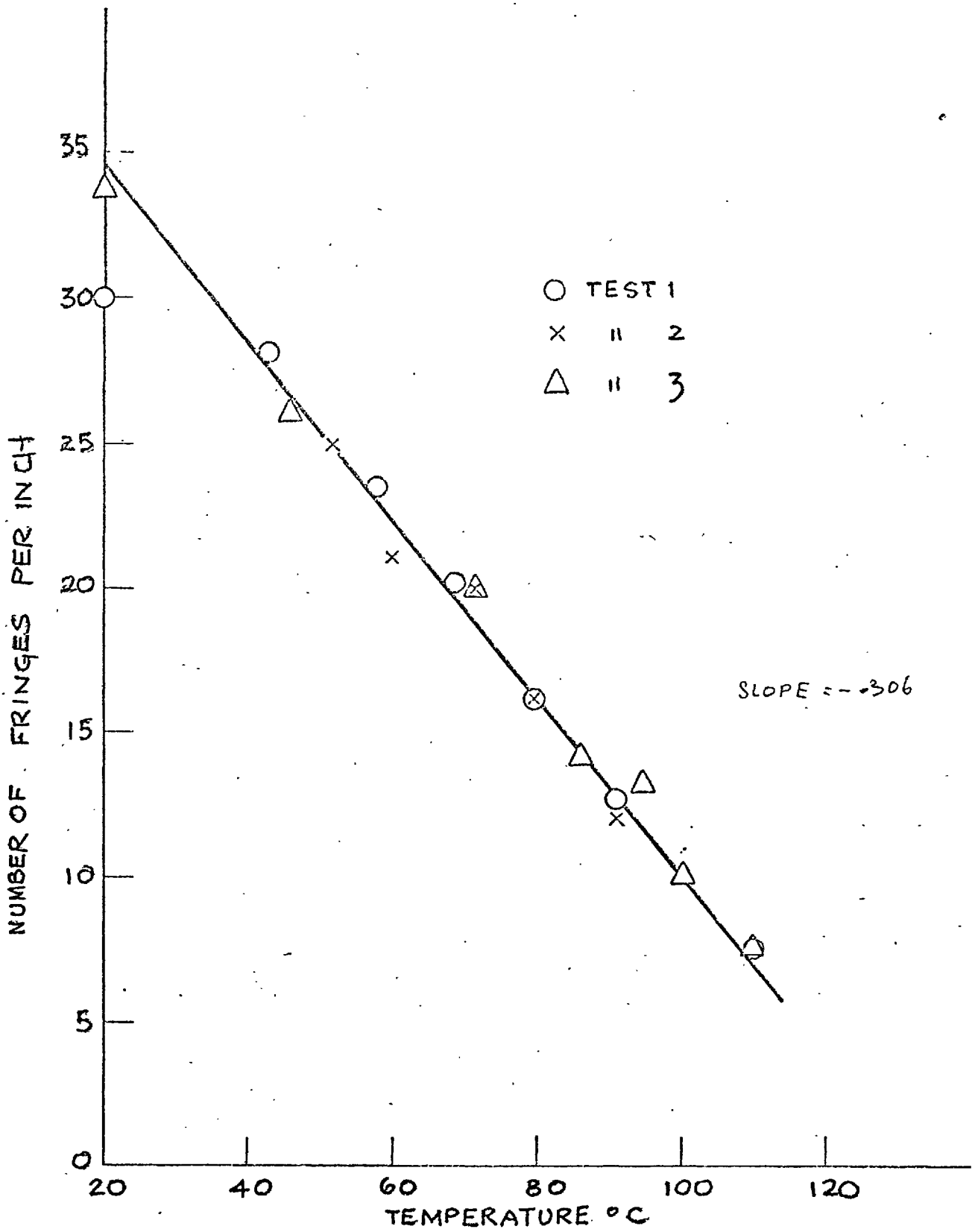

FIG 6·10 VARIATION OF FRINGE ORDER IN SHANK OF CALIBRATION SPECIMEN WITH TEMPERATURE.

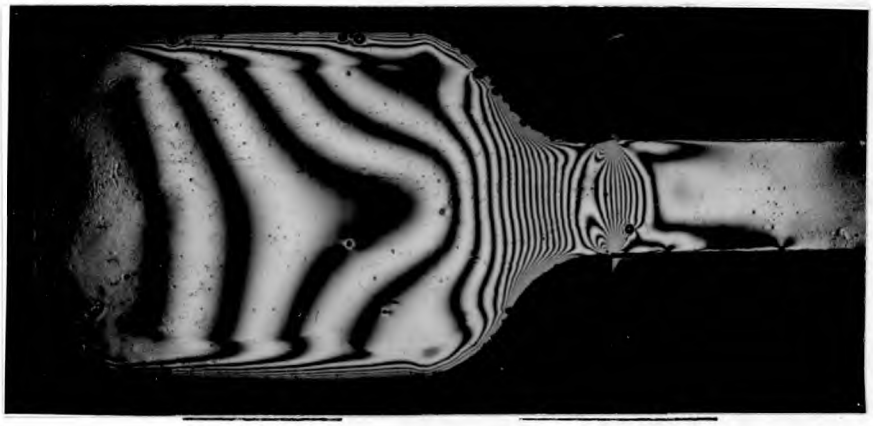

FIG.6.11a: ISOCHROMATICS IN CALIBRATION SPECIMEN AT ROOM TEMPERATURE (20°C) STILL BONDED TO MOULD.

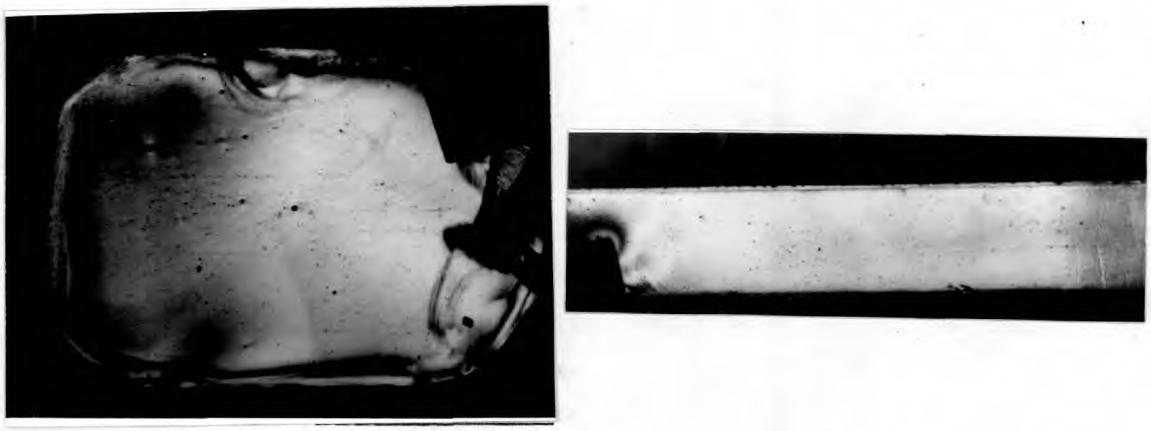

FIG.6.11b: ISOCHROMATICS IN CALIBRATION SPECIMEN AFTER BREAKING BOND.

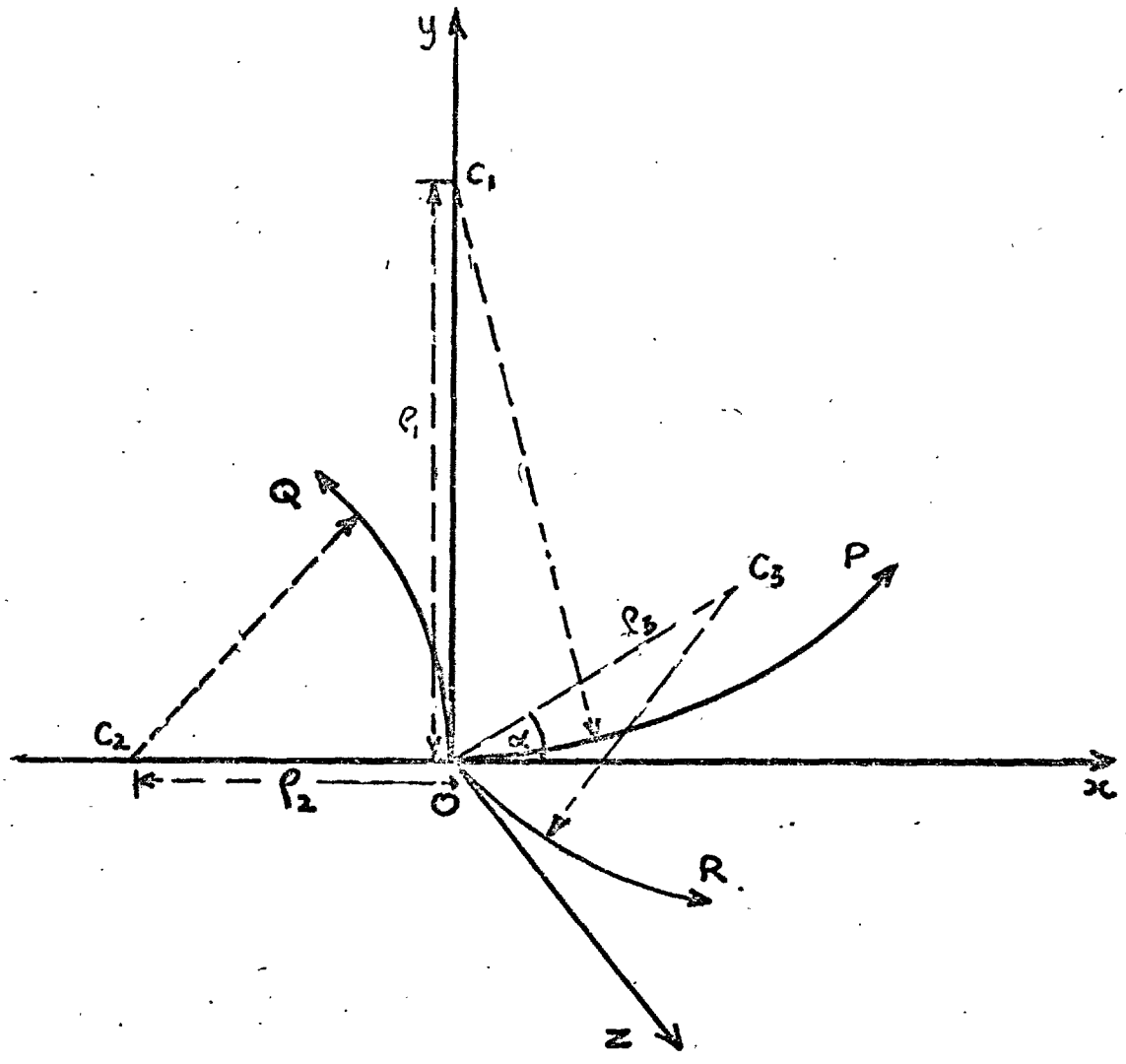

FIG.7.1: STRESS TRAJECTORIES IN 3-DIMENSIONS THROUGH POINT O. C_1, C_2, C_3 ARE CENTRES OF CURVATURE AND ρ_1, ρ_2, ρ_3 THE CORRESPONDING RADII OF CURVATURE.

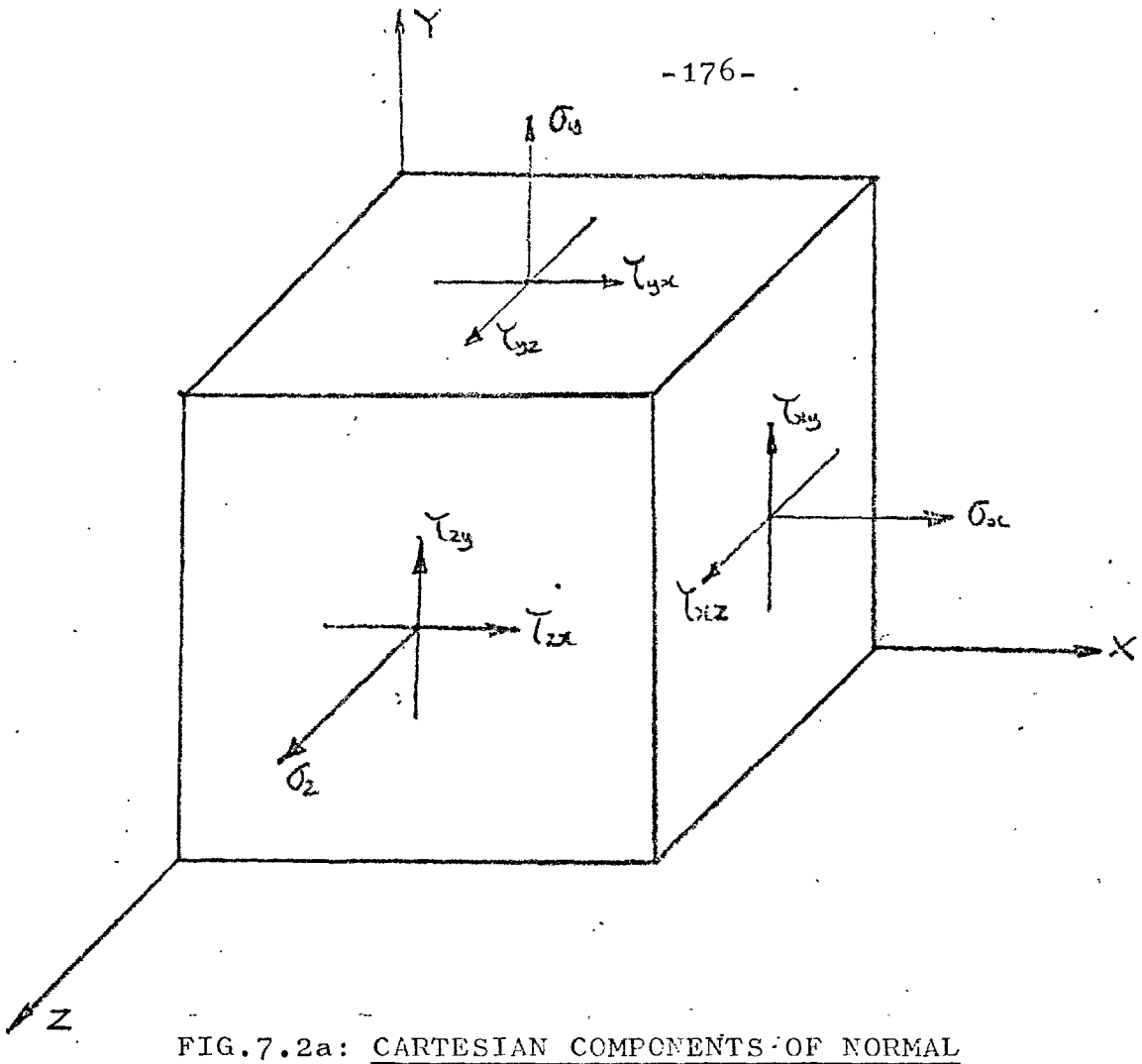

FIG.7.2a: CARTESIAN COMPONENTS OF NORMAL AND SHEAR STRESSES.

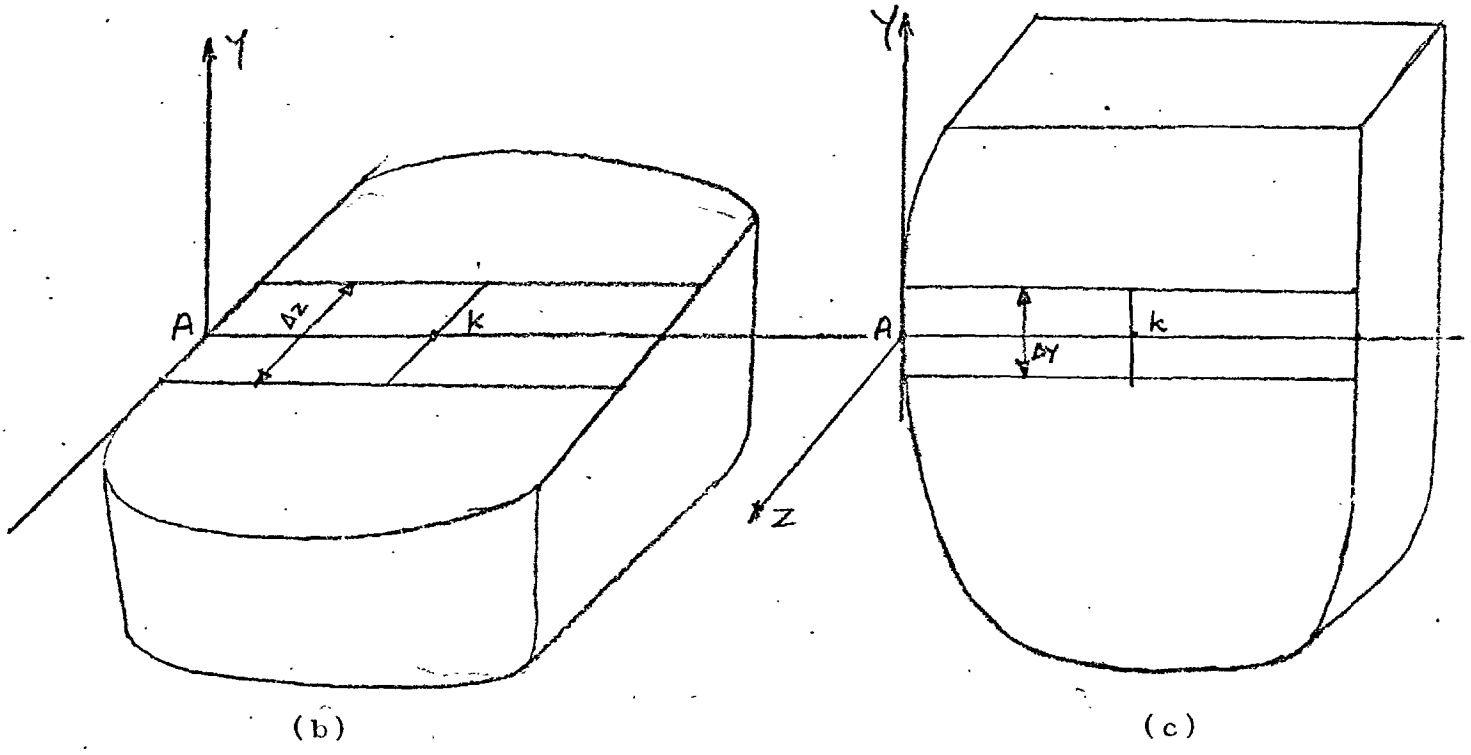

FIG.7.2b-2c: AUXILLIARY LINES IN XY AND XZ PLANES FOR SHEAR DIFFERENCE METHOD.

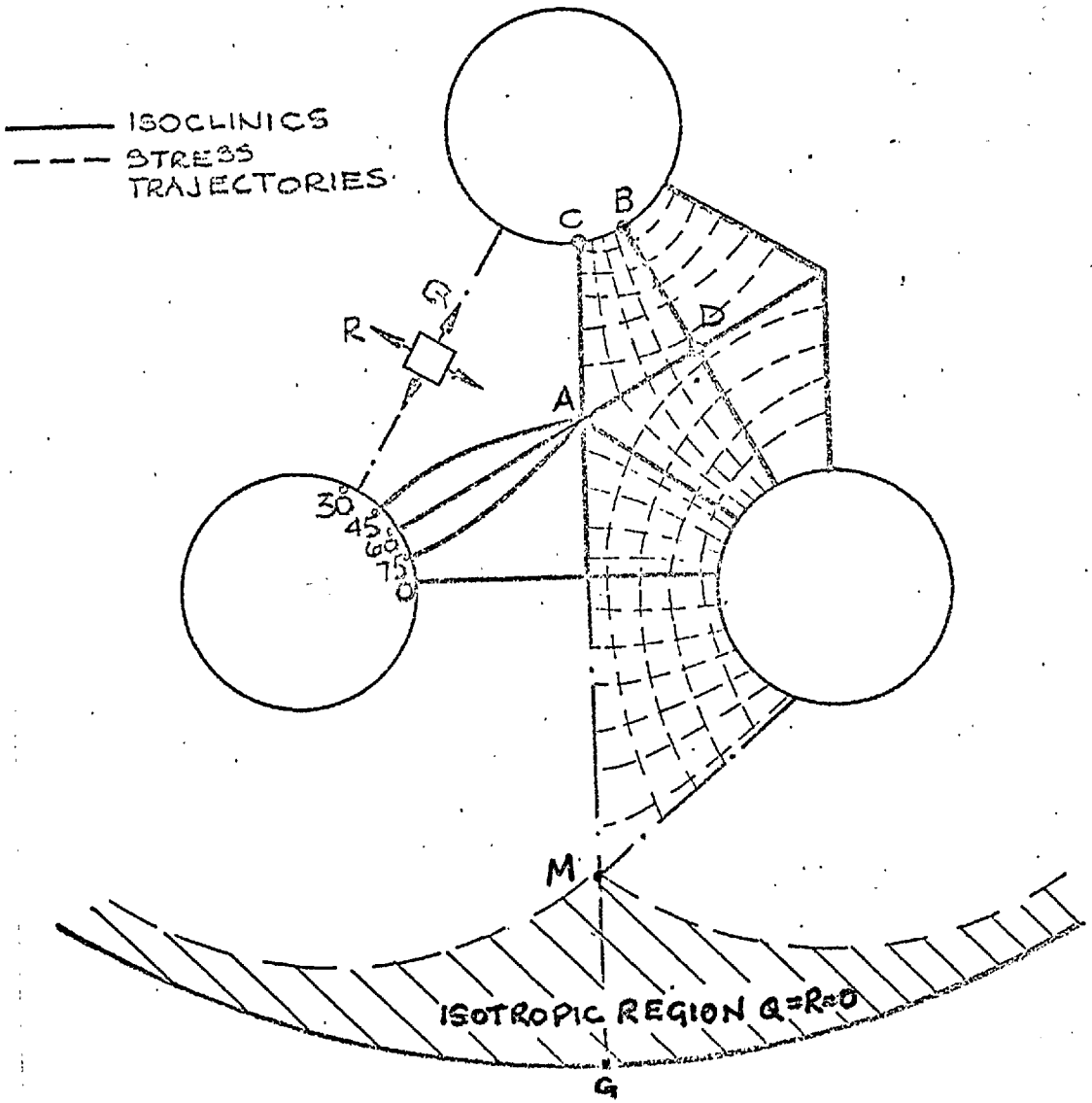

(a)

FIG. 7·3a: ISOCLINICS AND STRESS TRAJECTORIES FOR TRANSVERSE SLICE T.

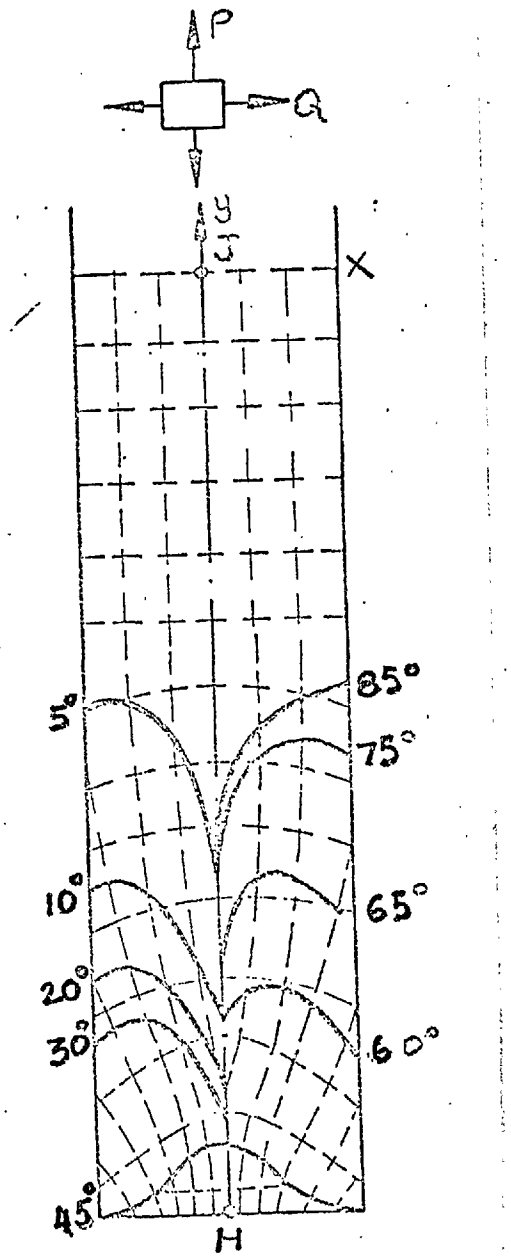

(b)

FIG. 7·3b: ISOCLINICS AND STRESS TRAJECTORIES FOR MERIDIONAL SLICE M

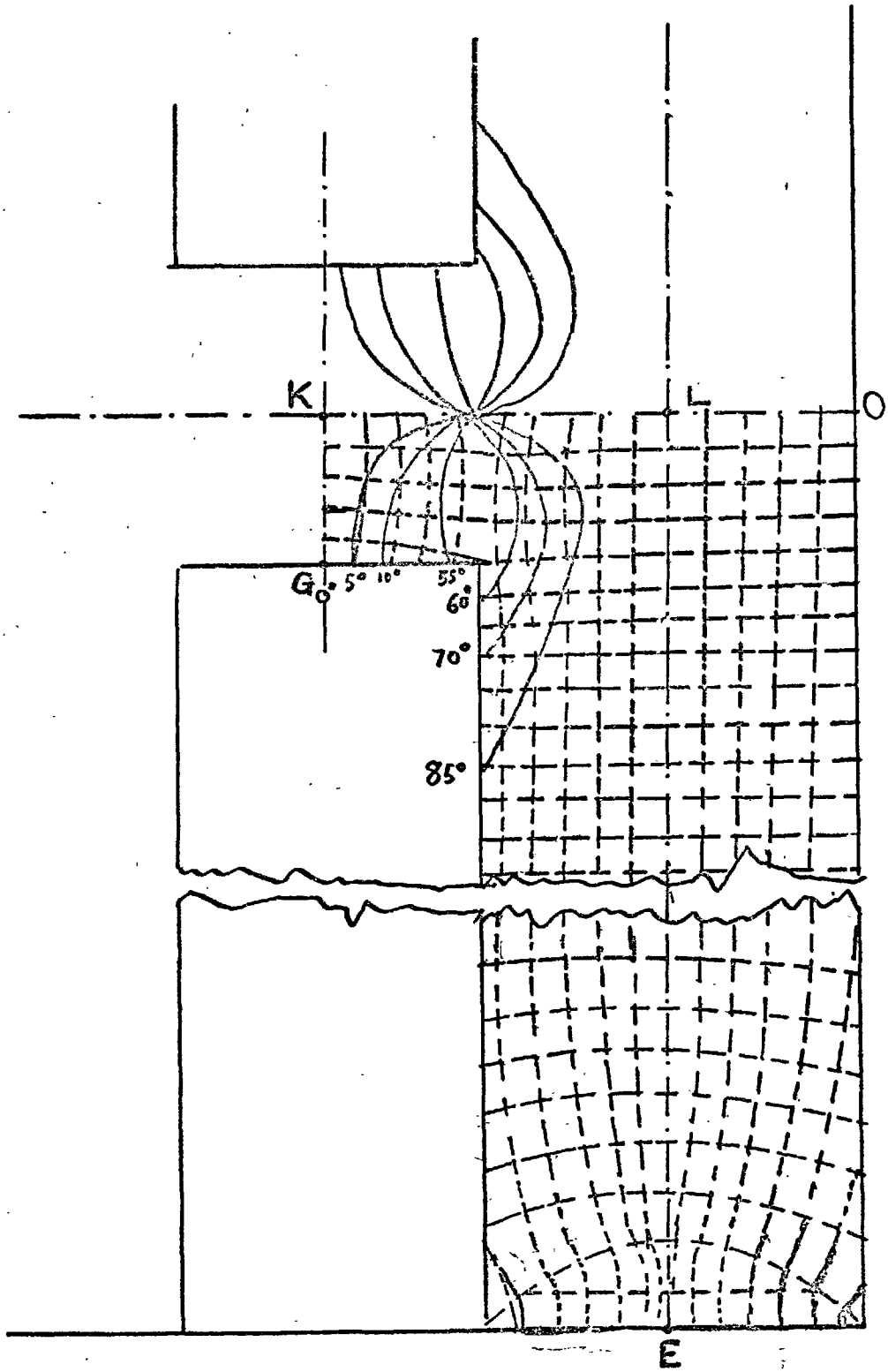

FIG.7.3c: TYPICAL ISOCLINICS AND STRESS TRAJECTORIES FOR A MERIDIONAL SLICE II FOR DISCONTINUOUS ROD ALSO SHOWING LINES OF INTEGRATION. ($m=4.5, \delta=\frac{1}{2}$)

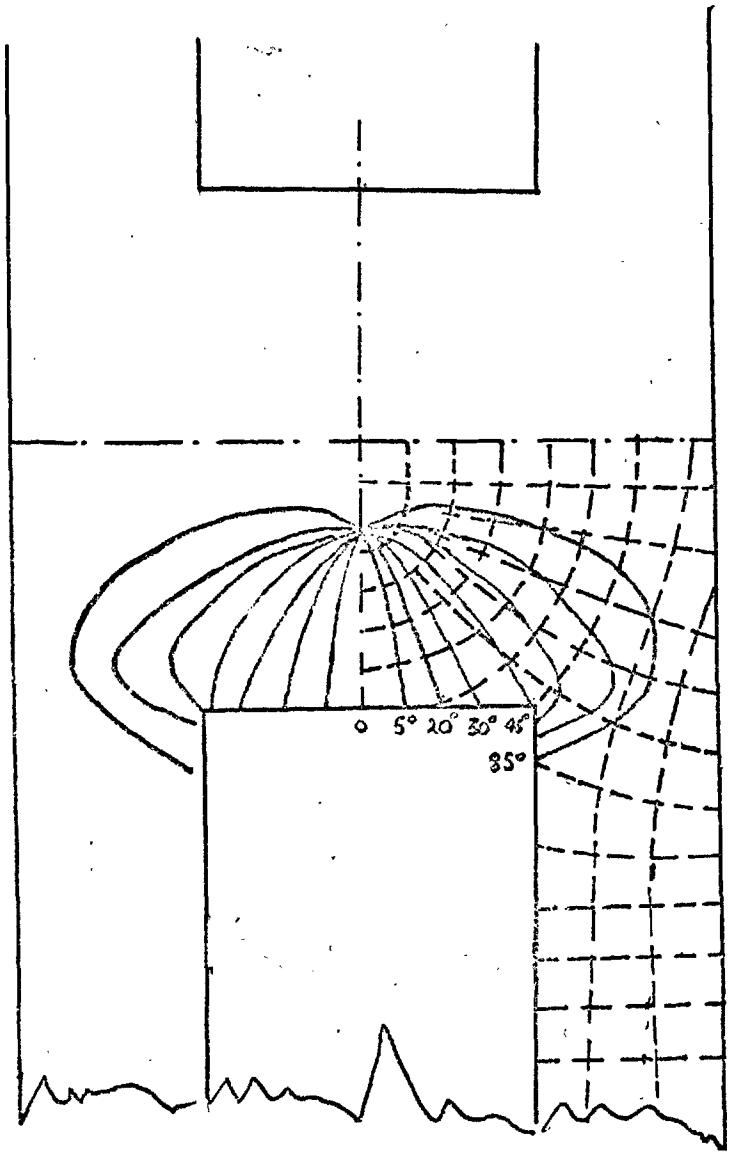

FIG. 7·3d: ISOCLINICS AND STRESS TRAJECTORIES FOR A MERIDIONAL SLICE II FOR DISCONTINUOUS ROD FOR m=3, δ=¾". (cf FIG 7.3c).

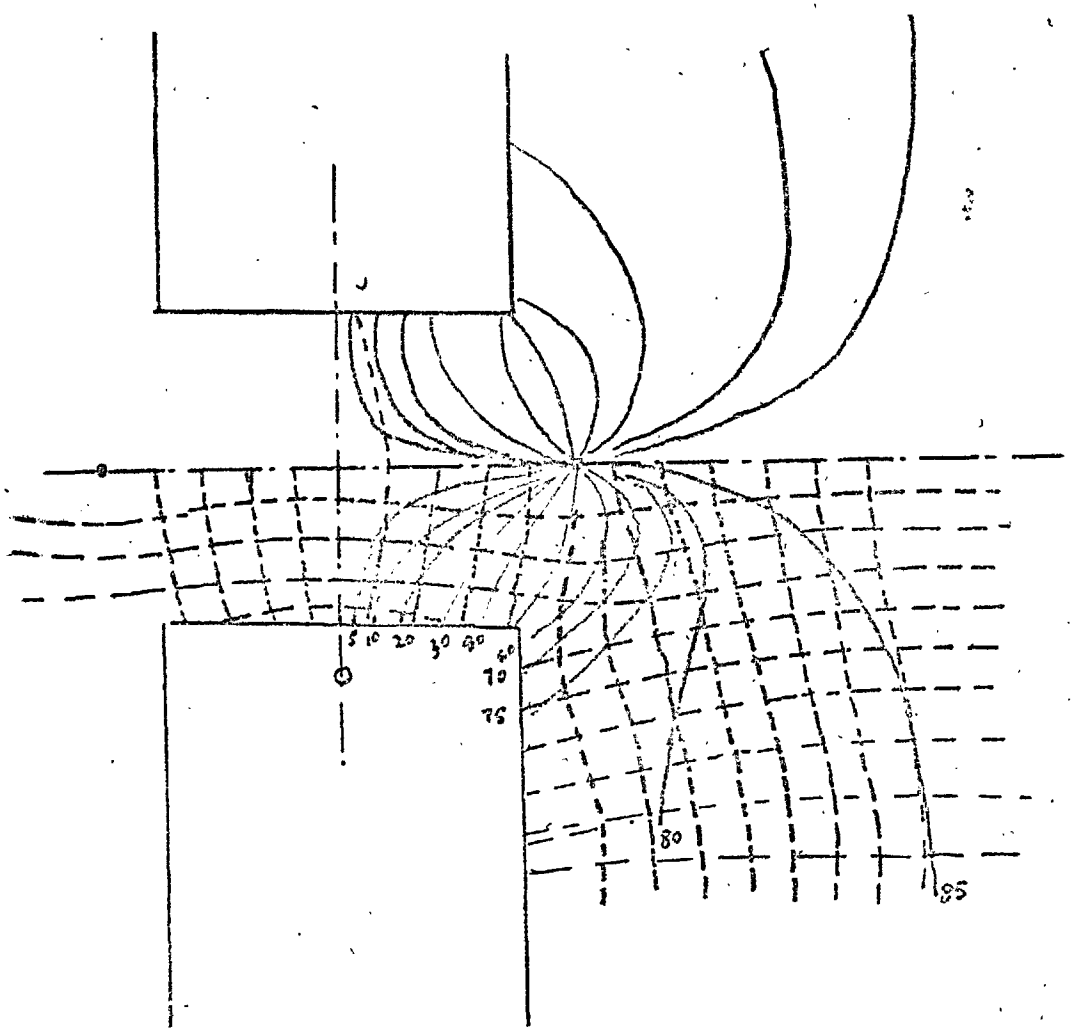

FIG. 7·3e: TYPICAL ISOCLINICS AND STRESS TRAJECTORIES FOR A MERIDIONAL SLICE III FOR DISCONTINUOUS ROD (m=3, δ=½").

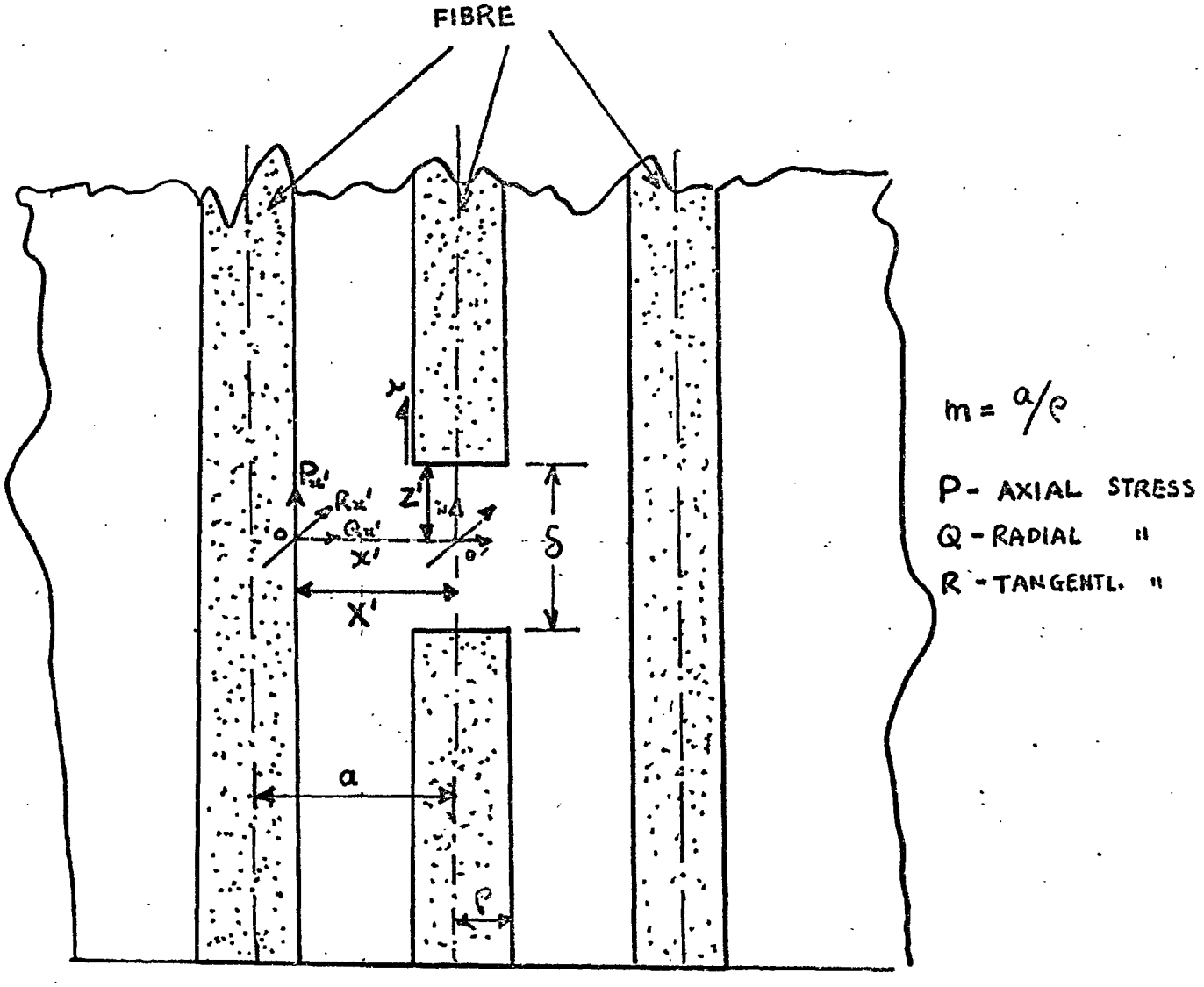

FIG. 7.4: SCHEME OF ANALYSIS FOR DISCONTINUOUS FIBRE.

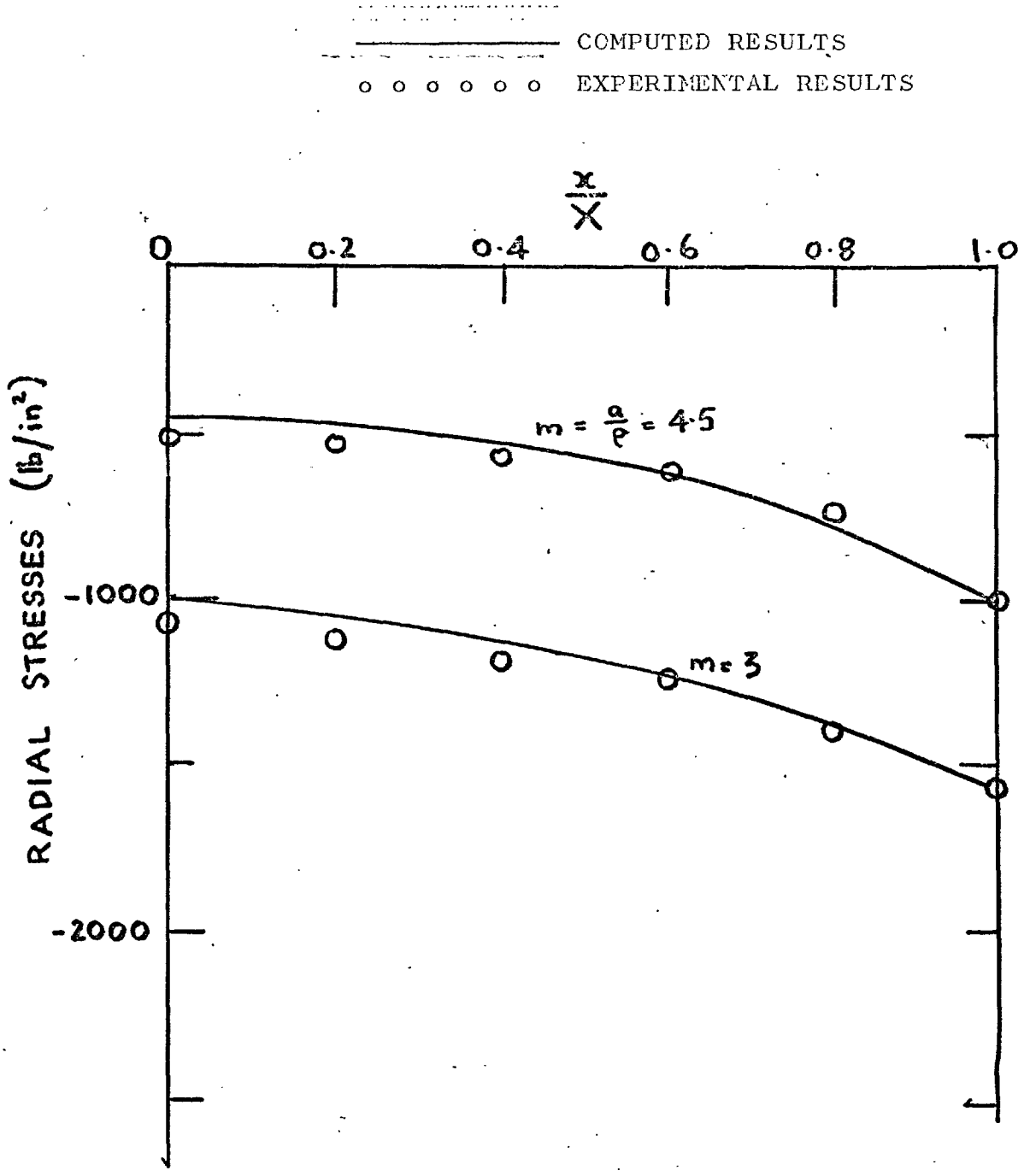

FIG.7.5: VARIATION OF RADIAL STRESS ON ox: A COMPARISON BETWEEN COMPUTED AND EXPERIMENTAL RESULTS.

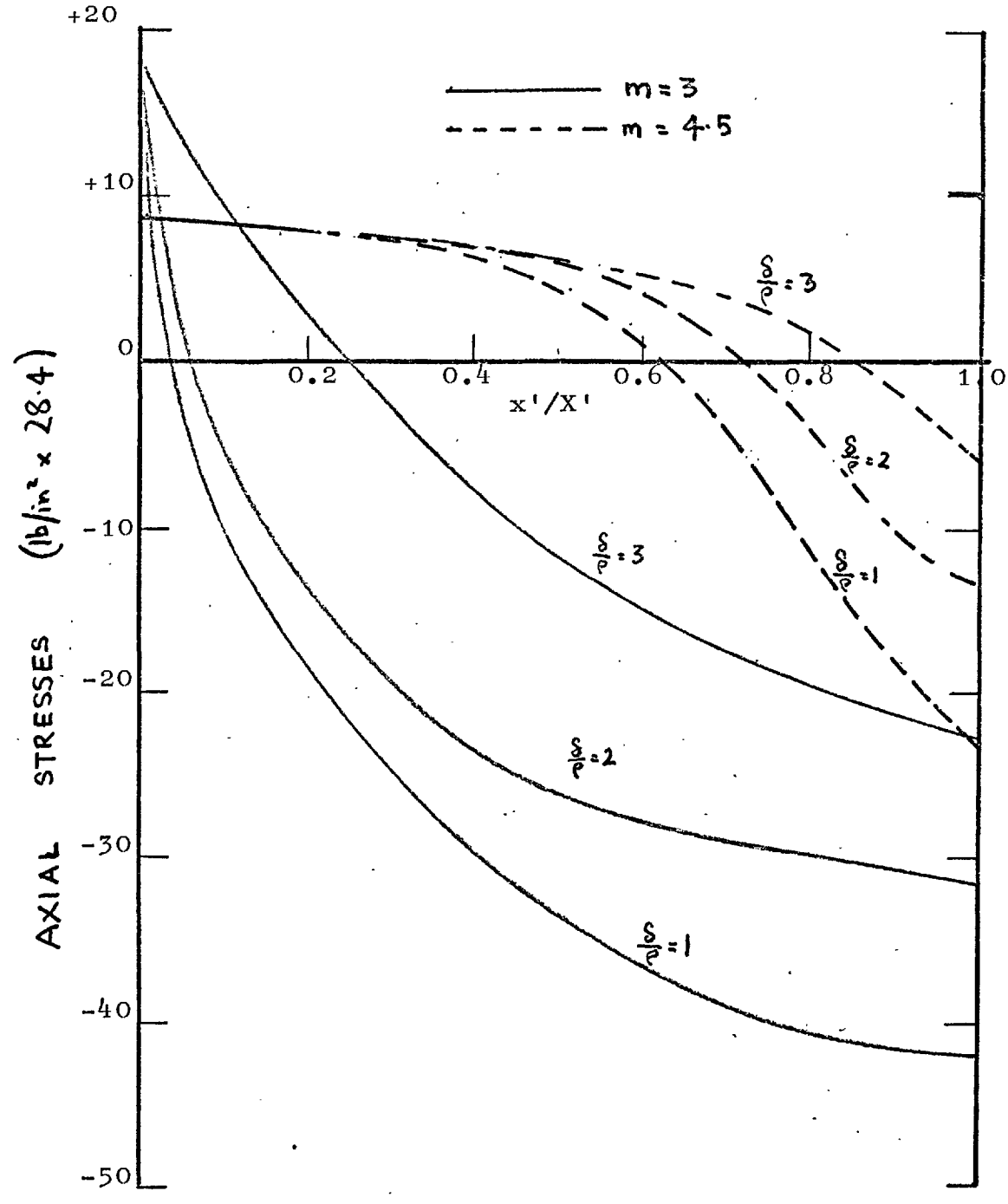

FIG.7.6a.: VARIATION OF AXIAL STRESS ON ox' FOR m=3 and m=4.5.

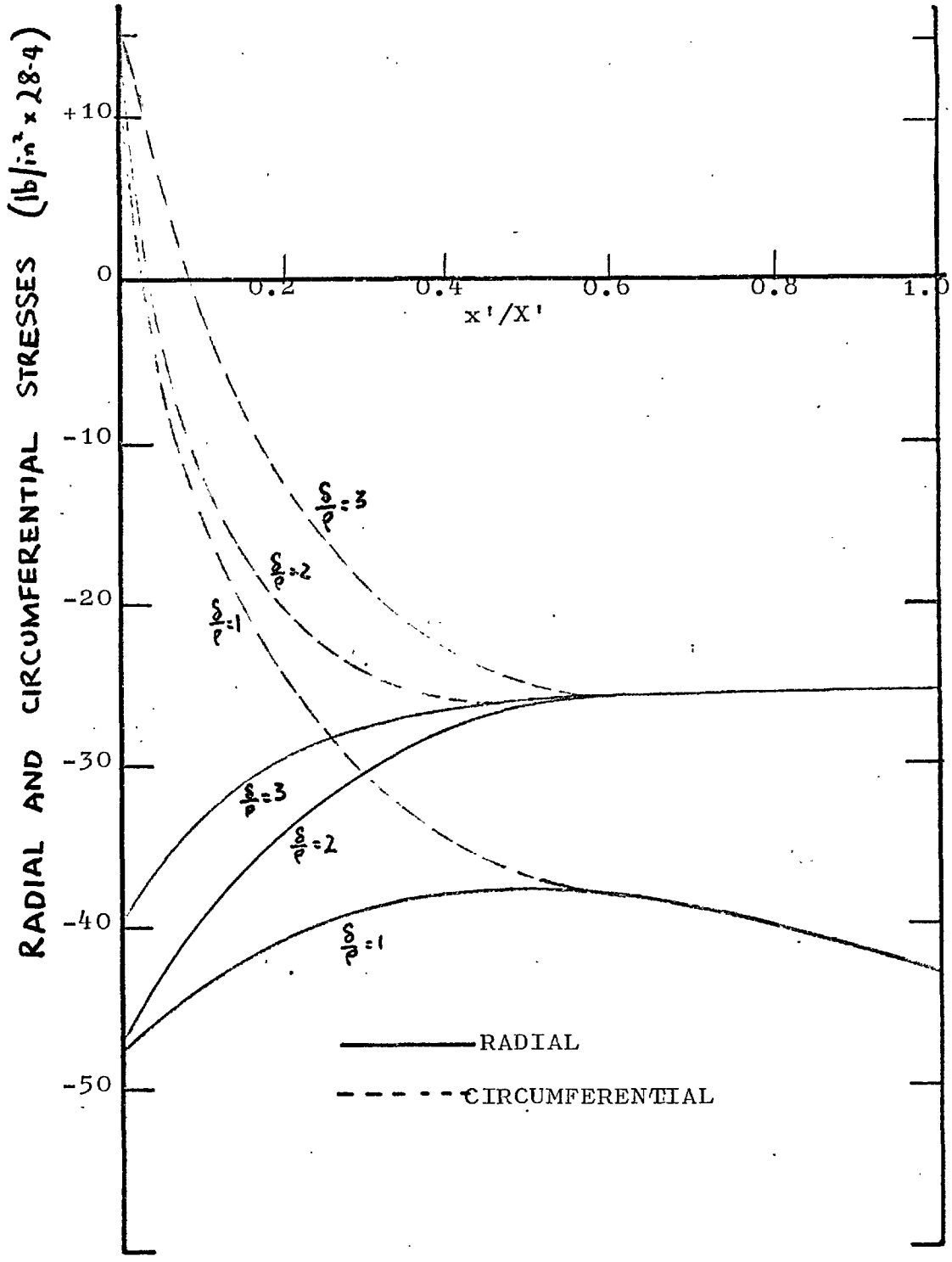

FIG. 7.6b : VARIATION OF RADIAL AND CIRCUMFERENTIAL STRESSES ON σx' FOR m=3.

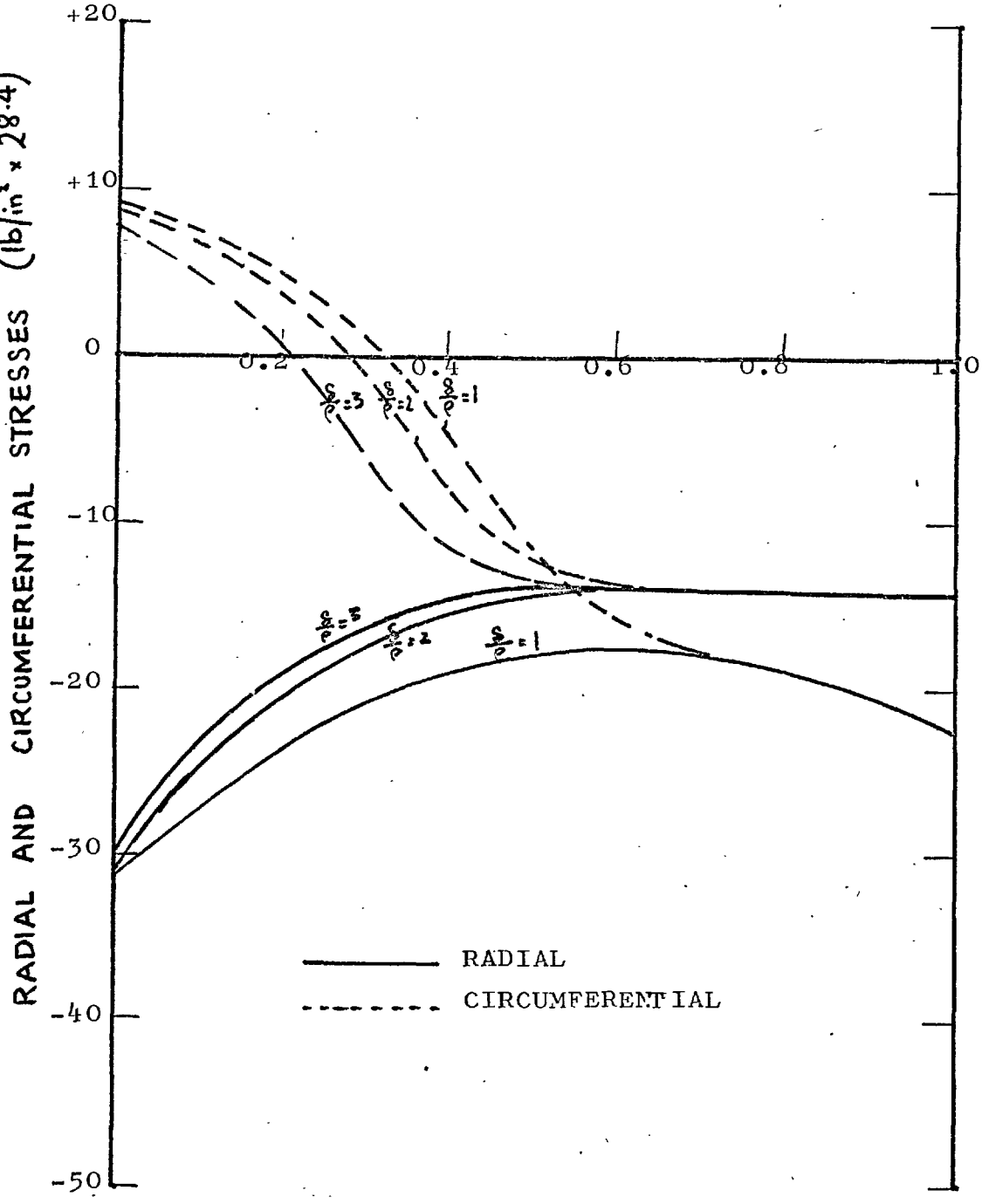

FIG. 7.6c : VARIATION OF RADIAL AND CIRCUMFERENTIAL STRESSES ON ox' FOR m=4.5.

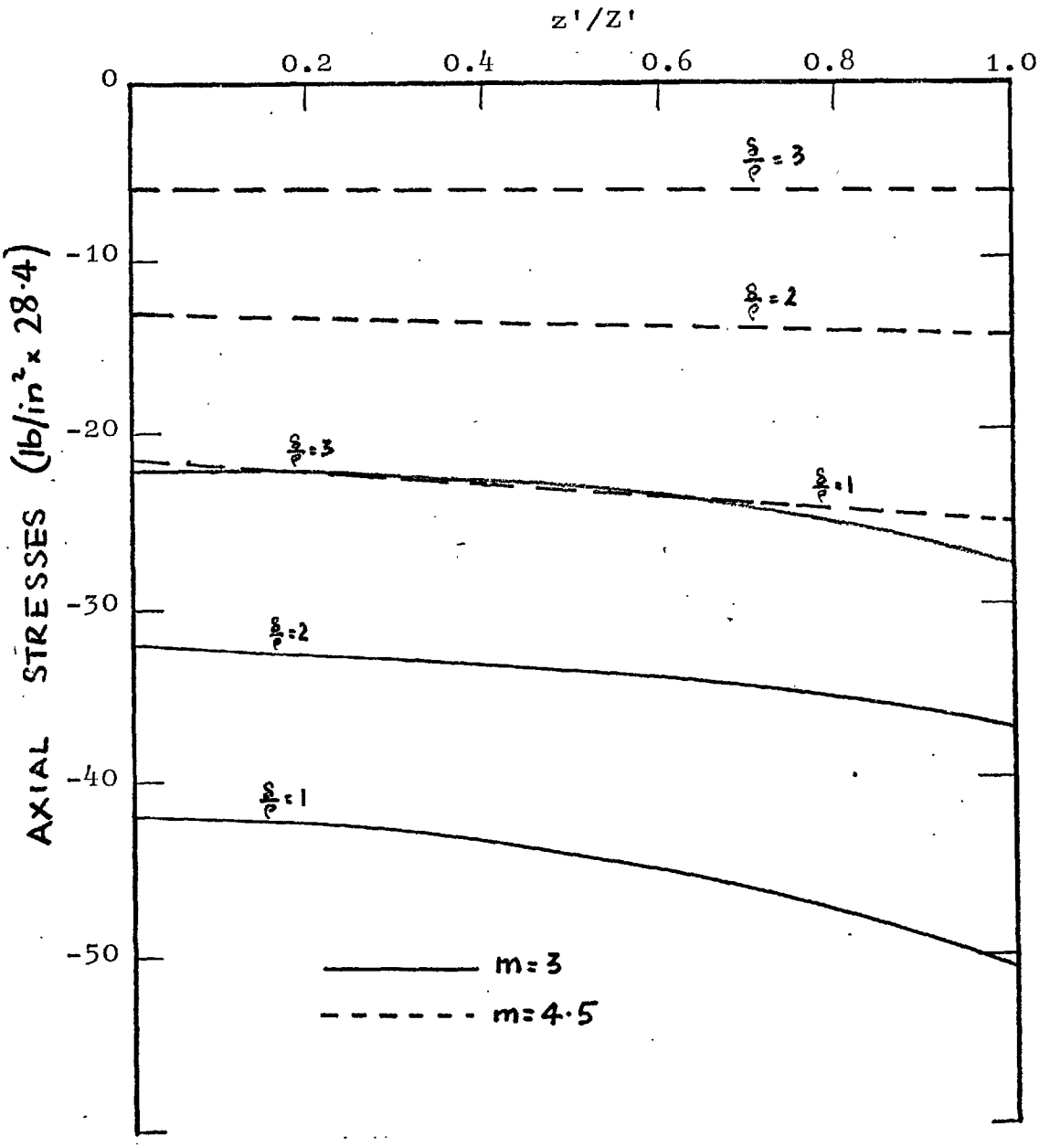

FIG. 7.7a :VARIATION OF AXIAL STRESS ON $\sigma'_{z'}$ FOR m=3 AND m=4.5.

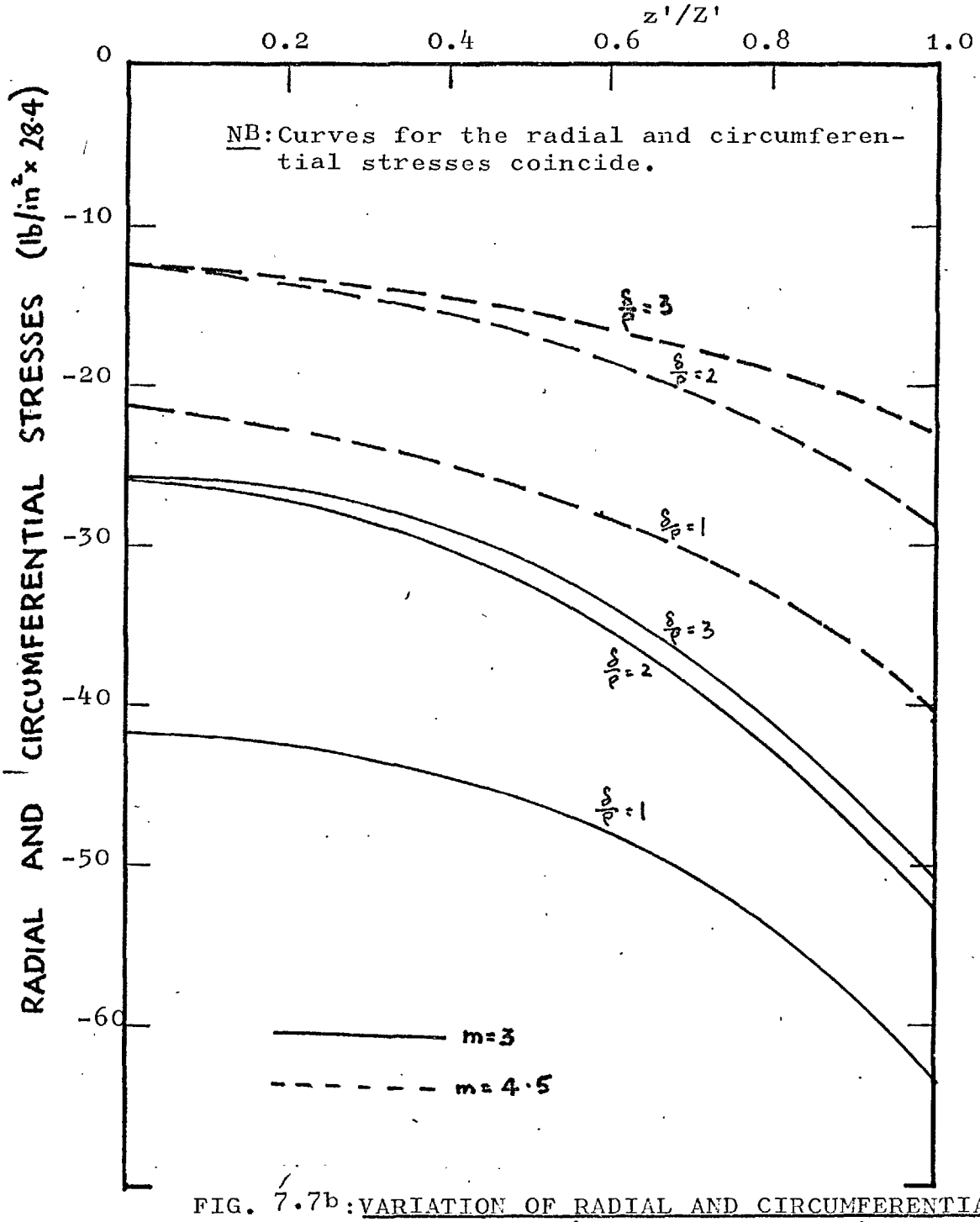

FIG. 7.7b: VARIATION OF RADIAL AND CIRCUMFERENTIAL STRESSES ON σ_z' FOR m=3 AND m=4.5.

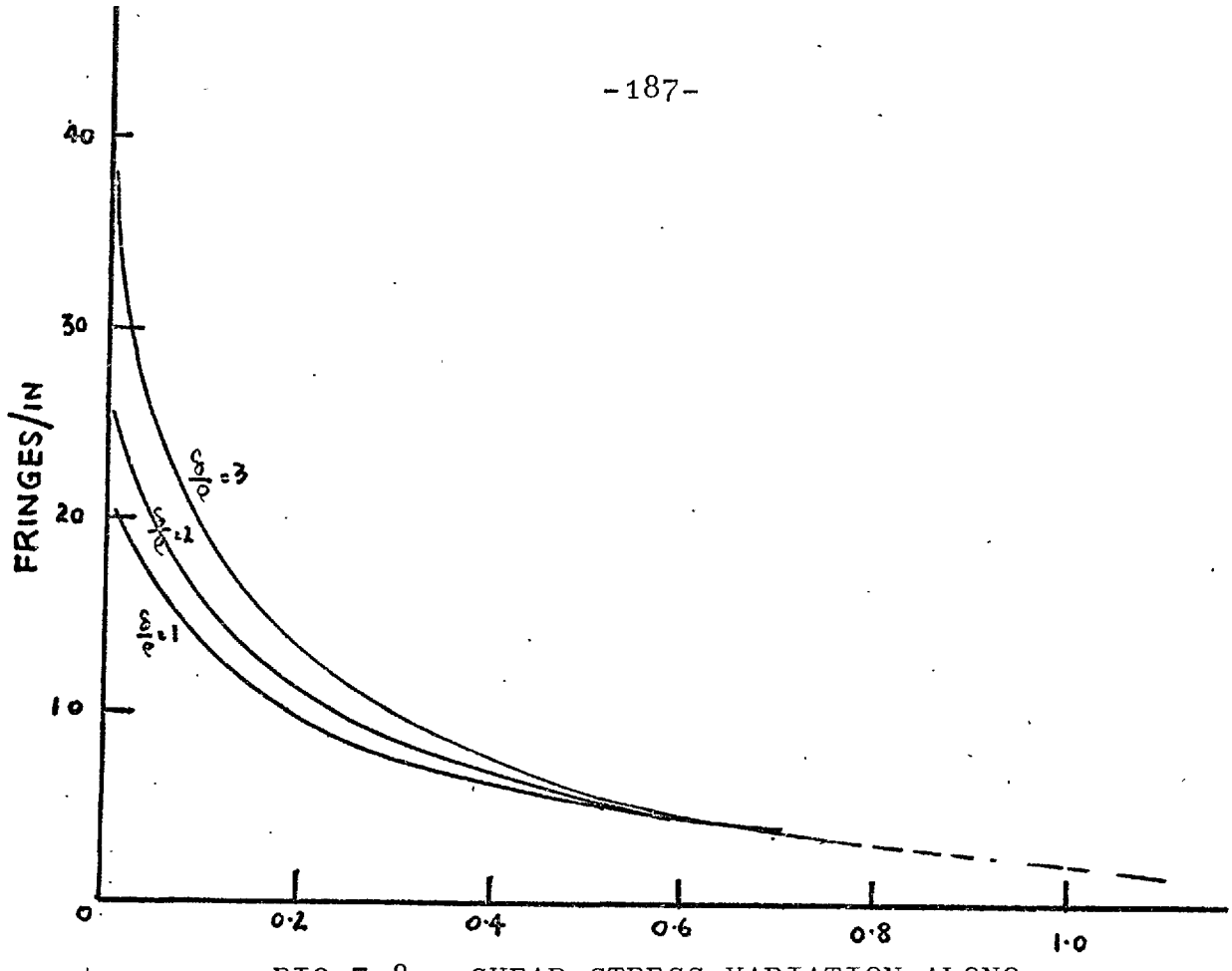

FIG.7.8a: SHEAR STRESS VARIATION ALONG DISCONTINUOUS FIBRE FOR m=4.5.

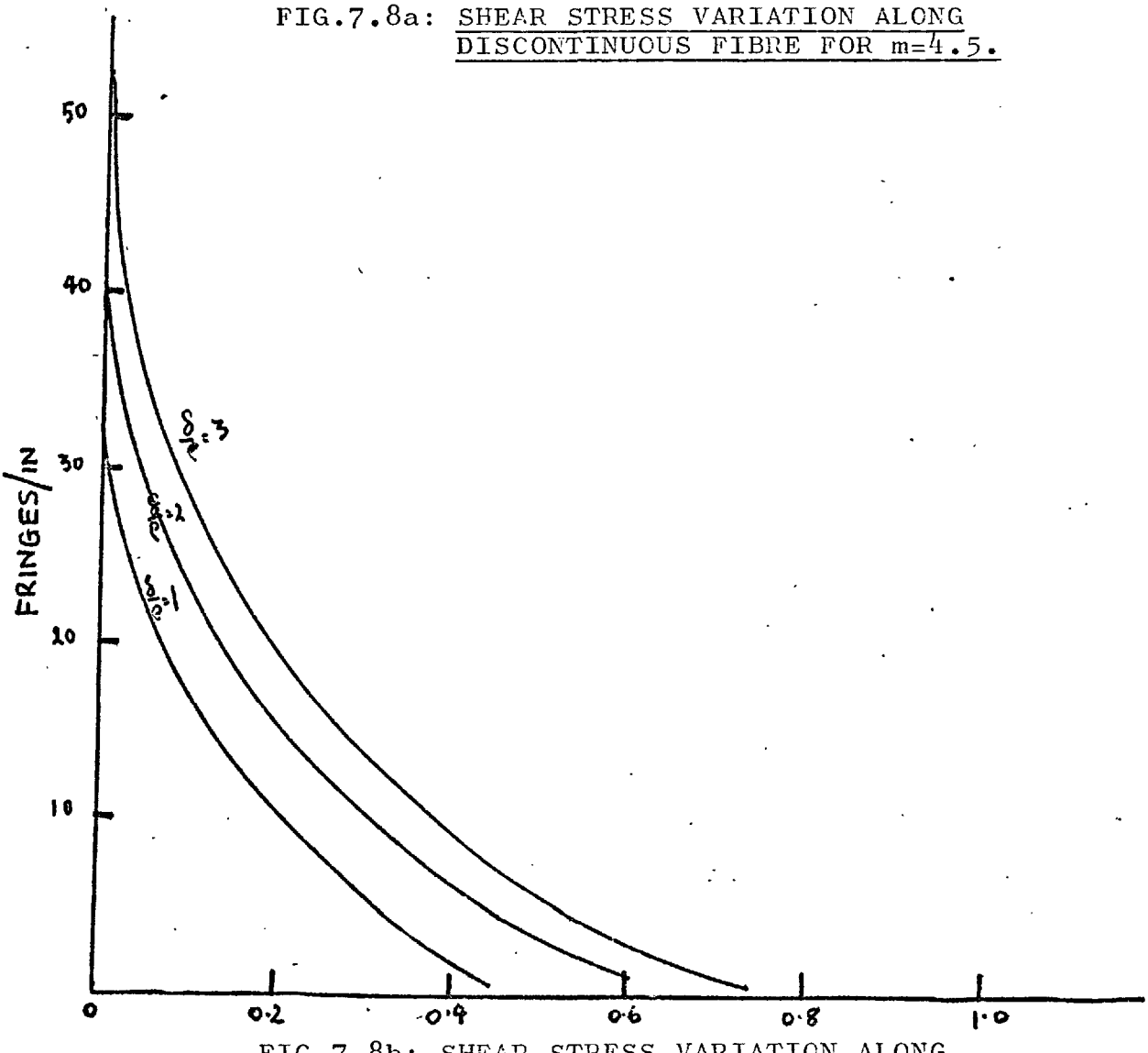

FIG.7.8b: SHEAR STRESS VARIATION ALONG DISCONTINUOUS FIBRE FOR m=3.

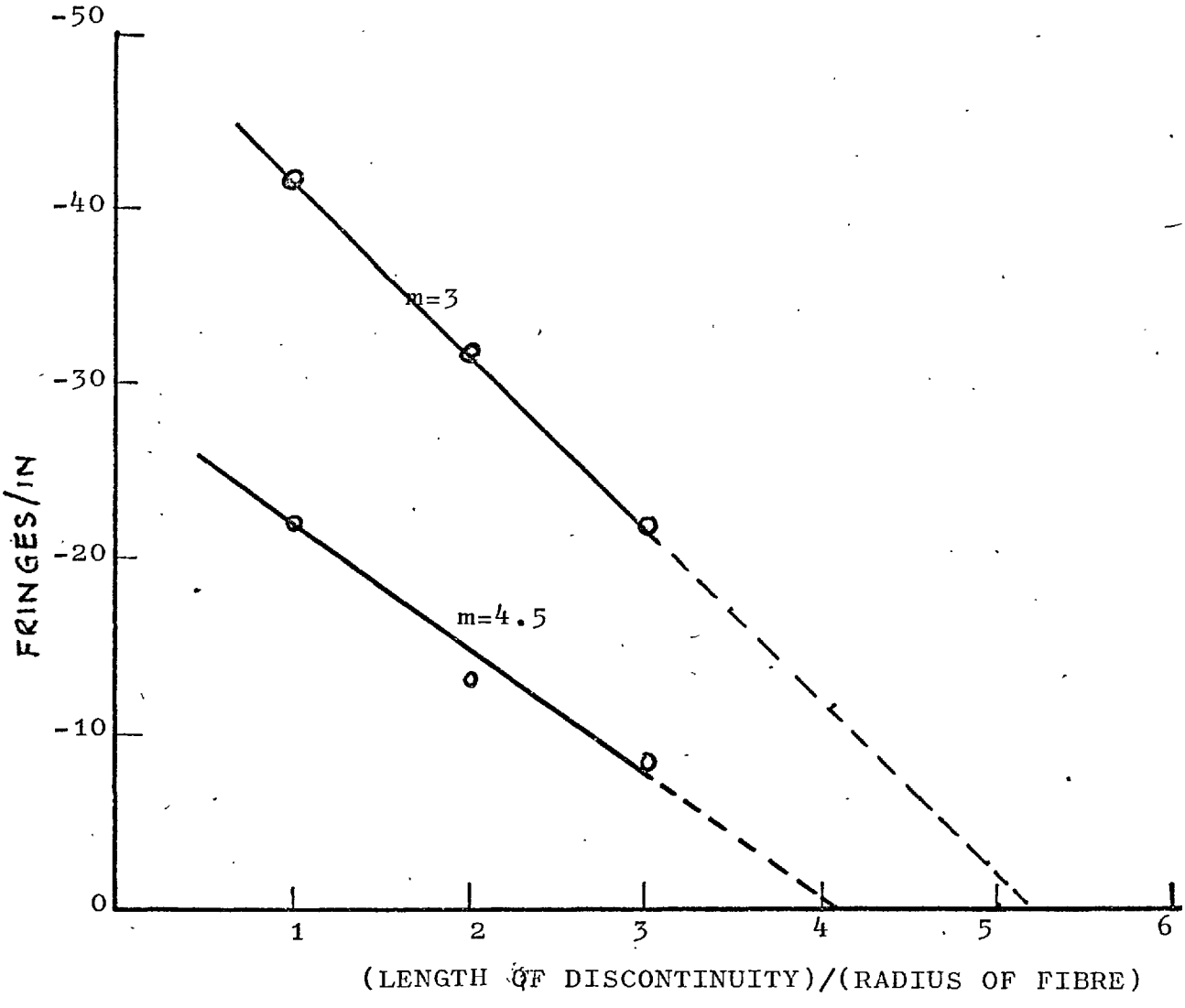

FIG.D.1:VARIATION OF AXIAL STRESS AT CENTRE OF DISCONTINUITY WITH LENGTH OF DISCONTINUITY.

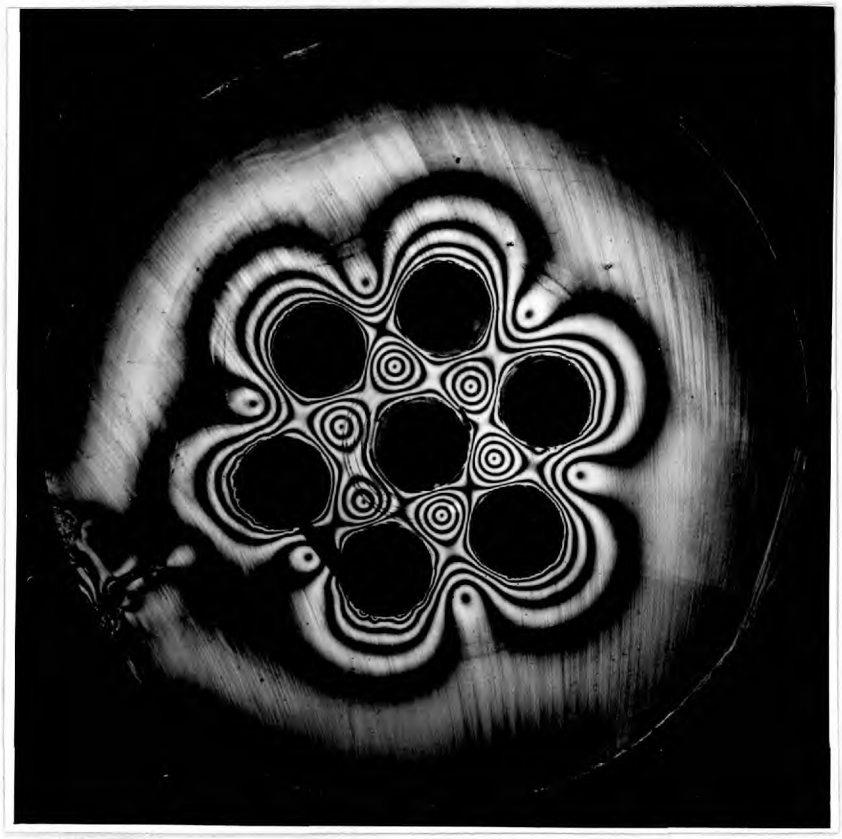

FIG.D.2: ISOCHROMATICS FROM A TRANSVERSE SLICE I FROM A GLASS/ARALDITE MODEL SHOWING UNIFORM FRINGE IN THE GLASS DISCS.

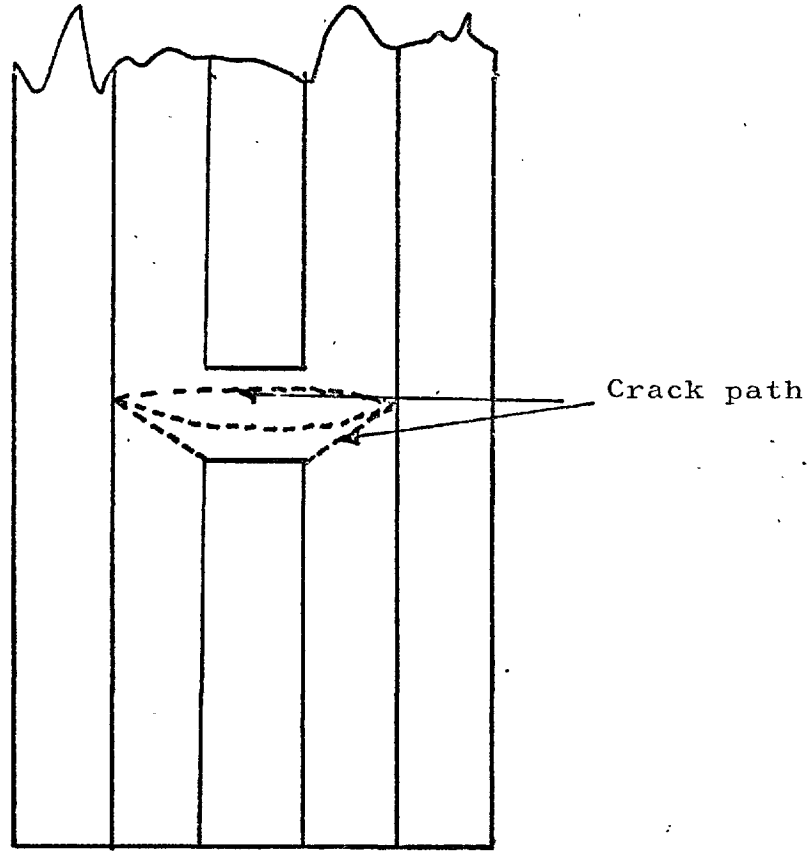

FIG.D. 3: CRACK FORMATION IN CLOSELY PACKED FIBRES.

A P P E N D I X I

DERIVATION OF ELEMENT STIFFNESS BY STATIONARY POTENTIAL ENERGY

The potential energy (V) of a system is the sum of the work done by external forces $\{F\}$ over displacement $\{\delta\}$ and the elastic energy stored in the system. Since, in the finite element method, the stress σ and strain ϵ are assumed constant in an element,

$$V = -\{F\}\{\delta\} + \frac{\{\sigma\}^T\{\epsilon\}}{2} \times (\text{volume})$$

For equilibrium $\frac{\partial V}{\partial \{\delta\}} = 0$

For a unit thickness of material if Δ is the area of the element, then,

$$0 = -\{F\}^T + [\{\sigma\}^T \frac{\partial\{\epsilon\}}{\partial\{\delta\}} + \{\epsilon\}^T \frac{\partial\{\sigma\}}{\partial\{\delta\}}] \frac{\Delta}{2}$$

Now if $\{\epsilon\} = [B]\{\delta\}$

and $\{\sigma\} = [D]\{\epsilon\} = [D][B]\{\delta\}$,

$$0 = -\{F\}^T + [([D][B]\{\delta\})^T[B] + ([B]\{\delta\}^T[D][B]] \frac{\Delta}{2}$$

[D] is the 'elasticity' matrix which for an isotropic material is symmetric i.e. $[D]^T \equiv [D]$

$$\therefore\ 0 = -\{F\}^T + 2(\{\delta\}^T[B]^T[D][B])\frac{\Delta}{2}$$

$$\text{i.e}[k]^e = \frac{\{F\}^T}{\{\delta\}^T} = \Delta[B]^T[D][B]$$

A P P E N D I X I I

FINITE ELEMENT FORMULATION FOR A TRIANGULAR ELEMENT

In Chapter 2, the theory of the finite element method was presented and the element characteristics derived. A Fortran programming for elastic analysis has been developed by Wilson (36). The most important element characteristic is its stiffness and we shall show how this can be obtained.

Figure A.1 shows a typical triangular element with nodes i, j, k, in a cartesian system. u, v, are the displacements in the x-, y-directions respectively; the dimensions of the triangle are also shown.

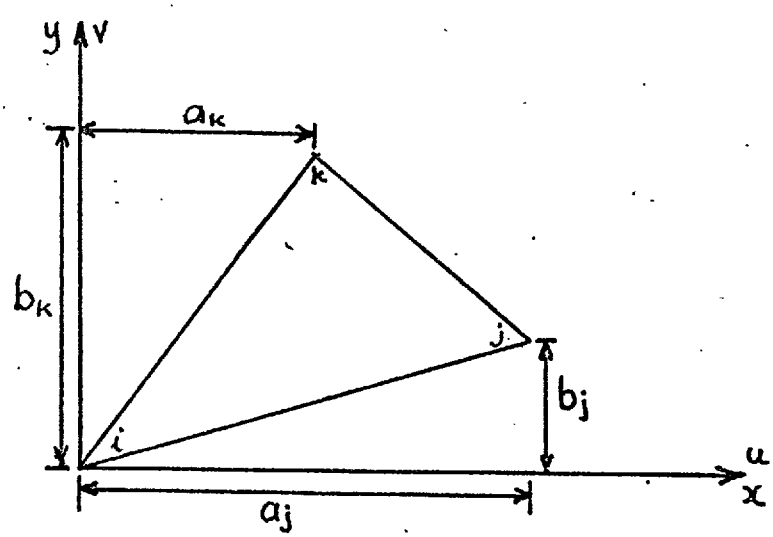

Fig. A.1 Triangular element dimensions

1. Displacement Functions

Starting with linear displacement functions:

$$\left.\begin{aligned} u_{(x,y)} &= u_i + c_1 x_i + c_2 y_i \\ v_{(x,y)} &= v_i + c_3 x_i + c_4 y_i \end{aligned}\right\} \quad \ldots\ldots\ldots\ldots \quad (A.2(i)$$

and expressing c_1, c_2 ..... in terms of the nodal displacements and geometry of the element, we obtain:

$$\begin{bmatrix} c_1 \\ c_2 \\ c_3 \\ c_4 \end{bmatrix} = \frac{1}{2\Delta} \begin{bmatrix} b_j-b_k & 0 & b_k & 0 & -b_j & 0 \\ a_k-a_j & 0 & -a_k & 0 & -a_j & 0 \\ 0 & b_j-b_k & 0 & b_k & 0 & -b_j \\ 0 & a_k-a_j & 0 & -a_k & 0 & a_j \end{bmatrix} \begin{bmatrix} u_i \\ v_i \\ u_j \\ v_j \\ u_k \\ v_k \end{bmatrix} \quad \cdots\cdots\cdots \text{(A.2(ii)}$$

where 2Δ = 2 x area of triangle = $(a_j b_k - a_k b_j)$

2. Strains (ϵ), [B] matrix

$$\{\epsilon\} = \begin{Bmatrix} \epsilon_x \\ \epsilon_y \\ \gamma_{xy} \end{Bmatrix} = \begin{Bmatrix} \frac{\partial u}{\partial x} \\ \frac{\partial v}{\partial y} \\ \frac{\partial u}{\partial y} + \frac{\partial v}{\partial x} \end{Bmatrix}$$

From equations (A.2(i)) and (A.2(ii)),

$$\{\epsilon\} = \frac{1}{2\Delta} \begin{bmatrix} b_j-b_k & 0 & b_k & 0 & -b_j & 0 \\ 0 & a_k-a_j & 0 & -a_k & 0 & a_j \\ a_k-a_j & b_j-b_k & -a_k & b_k & a_j & -b_j \end{bmatrix} \begin{bmatrix} u_i \\ v_i \\ u_j \\ v_j \\ u_k \\ v_k \end{bmatrix} \quad \cdots\cdots \text{(A.2(iii}$$

Comparing eq. (A.2(iii)) with eq. (2.4), the [B] matrix is easily identified.

3. Stress-Strain Relationship - [D] matrix

For the case of isotropic thermal expansion of an isotrpic material under plane strain conditions, using Hooke's law, we

obtain the relationships:

$$\epsilon_x = \frac{\sigma_x}{E} - \frac{\nu\sigma_y}{E} - \frac{\nu\sigma_z}{E} + \alpha\theta^e$$

$$\epsilon_y = \frac{-\nu\sigma_x}{E} + \frac{\sigma_y}{E} - \frac{\nu\sigma_z}{E} + \alpha\theta^e \qquad \text{(A.2(iv)}$$

$$\epsilon_z = \frac{-\nu\sigma_x}{E} - \frac{\nu\sigma_y}{E} + \frac{\sigma_z}{E} + \alpha\theta^e = 0$$

where θ is the temperature change in an element and α the coefficient of thermal expansion.

Eliminating σ_z and rearranging equation A.2(iv), the stress σ can be expressed in matrix form as:

$$\{\sigma\} = [D][\epsilon - \epsilon_o] \qquad \text{(cf equation 2.5)}$$

where ϵ_o are the initial strains.

The [D] matrix is obtained as:

$$[D] = \frac{E}{(1+\nu)(1-2\nu)} \begin{bmatrix} 1-\nu & \nu & 0 \\ \nu & 1-\nu & 0 \\ 0 & 0 & \frac{1-2\nu}{2} \end{bmatrix} \qquad \text{(A.2(v)}$$

4. Element stiffness $[k]^e$

From equation (2.7a):

$$[k]^e = \int [B]^T [D][B]\, t\,dx\,dy$$

where t is the thickness of the element and the integration is taken over the area of triangle. For unit thickness this becomes:

$$[k]^e = [B]^T[D][B]\Delta$$

and the actual matrix multiplication may be left to the computer.

5. Nodal Forces due to Initial Strains: $\{F\}^e_{\epsilon_o}$

From equation 2.7c:

$$\{F\}^e_{\epsilon_o} = -[B]^T[D][\epsilon_o]\Delta$$

this, after substitution, becomes:

$$\{F\}^e_{\epsilon_o} = \begin{bmatrix} F^i_x \\ F^i_y \\ F^j_x \\ F^j_y \\ F^k_x \\ F^k_y \end{bmatrix} = -\frac{E\alpha\Delta T}{2(1+\ )(1-2\ )} \begin{bmatrix} b_k - b_j \\ a_j - a_k \\ -b_k \\ a_k \\ b_j \\ -a_j \end{bmatrix} \quad \ldots\ldots \text{A.2(vi)}$$

6. Total Assemblage Stiffness [K]

For a typical element e, the equilibrium equation 2.8 may be written as:

$$\begin{bmatrix} F_i \\ F_j \\ F_k \end{bmatrix}^e = \begin{bmatrix} k_{ii} & k_{ij} & k_{ik} \\ k_{ji} & k_{jj} & k_{jk} \\ k_{ki} & k_{kj} & k_{kk} \end{bmatrix}_e \begin{bmatrix} \delta_i \\ \delta_j \\ \delta_k \end{bmatrix} \quad \ldots\ldots\ldots \quad (A.2(vii))$$

where in terms of arbitrary nodal points p, q :

$$[F_p]_x^e = \begin{bmatrix} F_x \\ F_y \end{bmatrix}_p^e$$

$$[\delta_q]^e = \begin{bmatrix} \delta_x \\ \delta_y \end{bmatrix}_q^e$$

and the stiffness coefficient k is of the form:

$$[k_{pq}]^e = \begin{bmatrix} k_{xx} & k_{xy} \\ k_{xy} & k_{yy} \end{bmatrix}_{pq}^e$$

which represents the forces developed on element e at nodal point p due to unit displacements at nodal point q.

$$\therefore K_{pq} = \sum_e [k_{pq}]^e$$

APPENDIX III

THE GAUSS-SEIDEL ITERATION

The Gauss-Seidel iteration for the solution of equation 2.8 involves the repeated calculation of new displacements from the equation:

$$\delta_n^{(s+1)} = K_{nn}^{-1}[F_n - \sum_{i=1}^{n-1} k_{ni}\delta_i^{(s+1)} - \sum_{i=n+1}^{N} k_{ni}\delta^{(s)}] \qquad \text{(A.3(i))}$$

where n is the number of nodal point and s is the cycle of iteration. The change in displacement $\Delta\delta_n^{(s)}$ between two successive cycles of iteration is given by:

$$\Delta\delta_n^{(s)} = \delta_n^{(s+1)} - \delta_n^{(s)}$$

and from equation (A.3(i)):

$$\Delta\delta_n^{(s)} = K_{nn}^{-1}\,[F_n - \sum_{i=1}^{n-1} k_{ni}\delta_i^{(3+1)} - \sum_{i=n}^{N} k_{ni}\delta_i^{(s)}]$$

By using an over-relaxation factor β, the new displacement $\delta_n^{(s+1)}$ of nodal point n is then determined from:

$$\delta_n^{(s+1)} = \delta_n^{(s)} + \beta\Delta\delta_n^{(s)}$$

This greatly speeds up the convergence.

THE COMPUTER PROGRAMME

THE Finite Element Method has been described in Chapter 2 and Appendices I-III. For completeness a listing of the programme for the plane stain analysis of continuous fibres presented in Chapter 3 is given here.

Data for the mesh include the nodal point coordinates, element nodes, elastic properties of the elements and the temperature change. Initial loads and displacements, if any, are also generally included in the data.

For each nodal point, the thermal load contributions from all the elements which meet at that node are summed up using the appropriate relationships, see Appendix II.

The B and D matrices are then set out from which the Stiffness matrix is obtained by the appropriate matrix multiplication. The stiffnesses are inverted to obtain the flexibilities which are then modified for the boundary nodal points according to the type of constraint imposed on them.

Next, the Gauss-Siedel iteration procedure is performed to obtain the correct nodal point displacements from which the strains and stresses are calculated.

```
C       DIMENSION AND COMMON STATEMENTS
        DIMENSION ARRAY(7)
        DIMENSION COF(5),EX(350),EY(350),EXY(350),EPLAS(350)
        DIMENSION NPNUM(201),XORD(201),YORD(201),DSX(201),DSY(201),
     1  1XLOAD(201),YLOAD(201),NP(201,10),SXX(201,9),SXY(201,9),SYX(201,9),
     1  2SYY(201,9),NAP(201)
        DIMENSION NUME(350),NPI(350),NPJ(350),NPK(350),ET(350),XU(350),
       1RO(350),COED(350),DT(350),THERM(350),AJ(350),BJ(350),AK(350),
       2BK(350),SIGXX(350),SIGYY(350),SIGXY(350),SLOPE(100)
        DIMENSION NPB(100),NFIX(100),LM(3),A(6,6),B(6,6),S(6,6)
        DIMENSION NSLOPE(201)
        INTEGER T1
        JEL=1
        INC=1
C       READ AND PRINT OF DATA
        NCYCLE=0
  150   READ(5,100) ARRAY
        WRITE(6,99)
        WRITE (6,100) ARRAY
  100   FORMAT(7A10)
        READ(5,1)NUMEL,NUMNP,NUMBC,NCPIN,NOPIN,NCYCM,TOLER,XFAC,T1
C     NUMBER OF ELEMENT, NUMBER OF NODAL POINT, NUMBER OF BOUNDARY CONDITIO
C     UNBALANCE CONDITION, PRINT-OUT INTERVAL, FULL OUTPUT PRINT-OUT
C     INTERVAL, MAXIMUM NUMBER OF CYCLES, TOLERANCE AND OVER-RELAXATION FAC
C     IF T1 IS NON-ZERO DATA PRINT-OUT IS SUPPRESSED
        WRITE(6,101)NUMEL
        WRITE(6,102)NUMNP
        WRITE(6,103)NUMBC
        WRITE(6,104)NCPIN
        WRITE(6,105)NOPIN
        WRITE(6,106)NCYCM
        WRITE(6,107)TOLER
        WRITE(6,108)XFAC
        READ(5,2)(NUME(N),NPI(N),NPJ(N),NPK(N),N=1,NUMEL)
C     ELEMENT NUMBER, ELEMENT NODAL POINTS
        READ(5,3)(NPNUM(M),XORD(M),YORD(M),XLOAD(M),YLOAD(M),
       1DSX(M),DSY(M),M=1,NUMNP)
C     NODAL POINT COORDINATES (X-Y), X-Y LOADS, INITIAL DISPLACEMENTS (X-Y)
  155   WRITE(6,110)
        WRITE(6,8)(NUME(N),NPI(N),NPJ(N),NPK(N),N=1,NUMEL)
        WRITE(6,111)
        WRITE(6,109)(NPNUM(M),XORD(M),YORD(M),XLOAD(M),YLOAD(M),
       1DSX(M),DSY(M),M=1,NUMNP)
        WRITE(6,112)
        DO 909 L=1,NUMBC
        READ(5,4)NPB(L),NFIX(L),SLOPE(L)
  909   WRITE(6,4)NPB(L),NFIX(L),SLOPE(L)
C     NFIX=0 NODAL POINT IS FIXED
C     NFIX=1 NODAL POINT CAN MOVE IN Y-DIRECTION ONLY
C     NFIX=2 NODAL POINT CAN MOVE IN X-DIRECTION ONLY
C     NFIX=3 NODAL POINT MOVES ALONG SLOPE
  151   CONTINUE
        READ(5,140)TET,TRO,TXU,TCOED,TDT
C     DATA CARD FOR MATRIX
C     TET IS YOUNG'S MODULUS
C     TRO-DENSITY, TXU-POISSON'S RATIO, TCOED-EXPSN COEFF, TDT-TEM CANGE
        WRITE(6,142)
        WRITE(6,143)TET,TRO,TXU,TCOED,TDT
        DO 178 I=1,144
```

```
      ET(I)=TET
      RO(I)=TRO
      XU(I)=TXU
      COED(I)=TCOED
      DT(I)=TDT
  178 CONTINUE
      READ(5,140)TET,TRO,TXU,TCOED,TDT
C     DATA CARD FOR FIBRE
      WRITE(6,144)
      WRITE(6,143)TET,TRO,TXU,TCOED,TDT
      DO 160 I=145,NUMEL
      ET(I)=TET
      RO(I)=TRO
      XU(I)=TXU
      COED(I)=TCOED
      DT(I)=TDT
  160 CONTINUE


C     CHECK FOR CORRECT MESH DIMENSIONS
        TAREA=0.
        DO 16 N=1,NUMEL
      I=NPI(N)
      J=NPJ(N)
      K=NPK(N)
      AJ(N)=XORD(J)-XORD(I)
      AK(N)=XORD(K)-XORD(I)
      BJ(N)=YORD(J)-YORD(I)
      BK(N)=YORD(K)-YORD(I)
  176 AREA=(AJ(N)*BK(N)-BJ(N)*AK(N))/2.
      IF(AREA.GT.0.) GO TO 177
  701 WRITE(6,711)N
  711 FORMAT (32H0ZERO OR NEGATIVE AREA, EL. NO.=1I4)
        TAREA=1.
        GO TO 16
```

```
C       MODIFICATION OF LOADS AND ELEMENT DIMENSIONS
C     THERMAL LOADS WORKED OUT AND ADDED TO ANY SPECIFIED LOADS
  177 THERM(N)=ET(N)*COED(N)*DT(N)/(XU(N)-1.)
      DL=AREA*RO(N)/3.
      XLOAD(I)=THERM(N)*(BK(N)-BJ(N))/2.+XLOAD(I)
      XLOAD(J)=-THERM(N)*BK(N)/2.+XLOAD(J)
      XLOAD(K)=THERM(N)*BJ(N)/2.+XLOAD(K)
      YLOAD(I)=THERM(N)*(AJ(N)-AK(N))/2.+YLOAD(I)-DL
      YLOAD(J)=THERM(N)*AK(N)/2.0+YLOAD(J)-DL
  180 YLOAD(K)=-THERM(N)*AJ(N)/2.+YLOAD(K)-DL
   16 CONTINUE
       IF(TAREA.NE.0.) STOP
C      INITIALIZATION
      NCYCLE=0
      NUMPT=NCPIN
      NUMOPT=NOPIN
      DO 175 L=1,NUMNP
      DO 170 M=1,9
      SXX(L,M)=0.0
      SYX(L,M)=0.0
      SXY(L,M)=0.0
      SYY(L,M)=0.0
  170 NP(L,M)=0
      NP(L,10)=0
  175 NP(L,1)=L
```

```
C       FORMATION OF STIFFNESS ARRAY
C     THE 'B' AND 'D' MATRICES ARE SET OUT AND STIFFNESS 'K' WORKED OUT
C     BY APPROPRIATE MATRIX MULTIPLICATION
        DO 200 N=1,NUMEL
        AREA=(AJ(N)*BK(N)-AK(N)*BJ(N))*0.5
        COMM=0.25*ET(N)/((1.0-XU(N)**2)*AREA)
        A(1,1)=BJ(N)-BK(N)
        A(1,2)=0.0
        A(1,3)=BK(N)
        A(1,4)=0.0
        A(1,5)=-BJ(N)
        A(2,2)=AK(N)-AJ(N)
        A(2,1)=0.0
        A(1,6)=0.0
        A(2,3)=0.0
        A(2,4)=-AK(N)
        A(2,5)=0.0
        A(2,6)=AJ(N)
        A(3,1)=AK(N)-AJ(N)
        A(3,2)=BJ(N)-BK(N)
        A(3,3)=-AK(N)
        A(3,4)=BK(N)
        A(3,5)=AJ(N)
        A(3,6)=-BJ(N)
        B(1,1)=COMM
        B(1,2)=COMM*XU(N)
        B(1,3)=0.0
        B(2,1)=COMM*XU(N)
        B(2,2)=COMM
        B(2,3)=0.0
        B(3,1)=0.0
        B(3,2)=0.0
        B(3,3)=COMM*(1.0-XU(N))*0.5
        DO 182 J=1,6
        DO 182 I=1,3
        S(I,J)=0.0
        DO 182 K=1,3
  182   S(I,J)=S(I,J)+B(I,K)*A(K,J)
        DO 183 J=1,6
        DO 183 I=1,3
  183   B(J,I)=S(I,J)
        DO 184 J=1,6
        DO 184 I=1,6
        S(I,J)=0.0
        DO 184 K=1,3
  184   S(I,J)=S(I,J)+B(I,K)*A(K,J)
```

```
C       COUNT OF ADJACENT NODAL POINTS
C
        LM(1)=NPI(N)
        LM(2)=NPJ(N)
        LM(3)=NPK(N)
        DO 200 L=1,3
        DO 200 M=1,3
        LX=LM(L)
        MX=0
  185   MX=MX+1
        IF(NP(LX,MX)-LM(M)) 190,195,190
  190   IF(NP(LX,MX)) 185,195,185
  195   NP(LX,MX)=LM(M)
        IF (MX-10) 196,702,702
  196   SXX(LX,MX)=SXX(LX,MX)+S(2*L-1,2*M-1)
        SXY(LX,MX)=SXY(LX,MX)+S(2*L-1,2*M)
        SYX(LX,MX)=SYX(LX,MX)+S(2*L,2*M-1)
  200   SYY(LX,MX)=SYY(LX,MX)+S(2*L,2*M)
        DO 206 M=1,NUMNP
        NSLOPE(M)=0.
        MX =1
  205   MX=MX+1
        IF (NP(M,MX)) 206,206,205
  206   NAP(M)=MX-1


C       INVERSION OF NODAL POINT STIFFNESS
C
        DO 210 M=1,NUMNP
        COMM=SXX(M,1)*SYY(M,1)-SXY(M,1)*SYX(M,1)
        TEMP=SYY(M,1)/COMM
        SYY(M,1)=SXX(M,1)/COMM
        SXX(M,1)=TEMP
        SXY(M,1)=-SXY(M,1)/COMM
  210   SYX(M,1)=-SYX(M,1)/COMM
```

```
C      MODIFICATION OF BOUNDARY FLEXIBILITIES
C    BOUNDARY FLEXIBILITIES MODIFIED ACCORDING TO TYPE OF RESTRAINT
       DO 240 L=1,NUMBC
       M=NPB(L)
       NSLOPE(M)=NFIX(L)
       NP(M,1)=0
       IF(NFIX(L)-1)225,220,357
  357  IF(NFIX(L).EQ.3) GO TO 240
       C=(SXX(M,1)*SLOPE(L) SXY(M,1))/(SYX(M,1)*SLOPE(L)-SYY(M,1))
       R=1.0-C*SLOPE(L)
       SXX(M,1)=(SXX(M,1)-C*SYX(M,1))/R
       SXY(M,1)=(SXY(M,1)-C*SYY(M,1))/R
       SYX(M,1)=SXX(M,1)*SLOPE(L)
       SYY(M,1)=SXY(M,1)*SLOPE(L)
       CC TO 240
  220  SYY(M,1)=SYY(M,1)-SYX(M,1)*SXY(M,1)/SXX(M,1)
       GO TO 230
  225  SYY(M,1)=0.0
  230  SXX(M,1)=0.0
  235  SXY(M,1)=0.0
       SYX(M,1)=0.0
  240  CONTINUE
C


C      ITERATION ON NODAL POINT DISPLACEMENTS
C    SOLUTION OF EQUILIBRIUM EQUATIONS-THE GAUSS-SIEDEL ITERATION
C
  243  WRITE(6,119)
  244  SUM=0.0
       SUMD=0.
       DO 290 M=1,NUMNP
       NUM=NAP(M)
       IF (SXX(M,1)+SYY(M,1)) 275,290,275
  275  FRX=XLOAD(M)
       FRY=YLOAD(M)
       DO 280 L=2,NUM
       N=NP(M,L)
       DSX(155)=DSX(13)
       FRX=FRX-SXX(M,L)*DSX(N)-SXY(M,L)*DSY(N)
  280  FRY=FRY-SYX(M,L)*DSX(N)-SYY(M,L)*DSY(N)
  281  DX=SXX(M,1)*FRX+SXY(M,1)*FRY DSX(M)
       DY=SYX(M,1)*FRX+SYY(M,1)*FRY DSY(M)
        IF(M.EQ.13) DXNOD=DX
       IF(NSLOPE(M).EQ.3) DX=DXNOD
       GO TO 297
  297  DSX(M)=DSX(M)+DX
       DSY(M)=DSY(M)+DY
       SUMD=SUMD+ABS(DSX(M))+ABS(DSY(M))
       IF(NP(M,1))285,290,285
  285  SUM=SUM+ABS(DX)+ABS(DY)
  290  CONTINUE
       SUM=SUM/SUMD
C
```

```
C       CYCLE COUNT AND PRINT CHECK
C
        NCYCLE=NCYCLE +1
        IF (NCYCLE-NUMPT) 305,300,300
  300   NUMPT=NUMPT NCPIN
        WRITE(6,120) NCYCLE,SUM,SUMD
  305   IF(SUM-TOLER) 400,400,310
  310   IF(NCYCM-NCYCLE)400,400,315
  315   IF (NCYCLE-NUMOPT) 244,320,320
  320   NUMOPT=NUMOPT+NOPIN
C
C       PRINT OF DISPLACEMENTS AND STRESSES
C
  400   WRITE(6,99)
        WRITE(6,121)
        WRITE(6,122)(NPNUM(M),DSX(M),DSY(M),M=1,NUMNP)
        WRITE(6,126)
        DO 420 N=1,NUMEL
        I=NPI(N)
        J=NPJ(N)
        K=NPK(N)
        EPX=(BJ(N)-BK(N))*DSX(I)+BK(N)*DSX(J)-BJ(N)*DSX(K)
        EPY=(AK(N)-AJ(N))*DSY(I)-AK(N)*DSY(J)+AJ(N)*DSY(K)
        GAM= (AK(N) AJ(N))*DSX(I)-AK(N)*DSX(J) AJ(N)*DSX(K)
       1     (BJ(N)-BK(N))*DSY(I)+BK(N)*DSY(J)-BJ(N)*DSY(K)
        COMM=ET(N)/((1.0-XU(N)**2)*(AJ(N)*BK(N)-AK(N)*BJ(N)))
        X=COMM*(EPX XU(N)*EPY)+THERM(N)
        Y=COMM*(EPY XU(N)*EPX)+THERM(N)
        XY=COMM*GAM*(1.-XU(N))*.5
        SIGXX(N)=X
        SIGYY(N)=Y
        SIGXY(N)=XY
        C=(X+Y)/2.0
        R=SQRT(((Y-X)/2.0)**2+XY**2)
        XMAX=C+R
        XMIN=C-R
```

```
C    RESOLUTION OF STRESSES INTO RADIAL AND TANGENTIAL COMPONENTS
       XMEAN=(XORD(I)+XORD(J)+XORD(K))/3.
       YMEAN=(YORD(I)+YORD(J)+YORD(K))/3.
       CRX=57.7-XMEAN
       CRY=100.-YMEAN
       CZ=CRX**2+CRY**2
       COSASQ=(CRX**2)/CZ
       SINASQ=(CRY**2)/CZ
       SIN2A=2.0*CRX*CRY/CZ
       SIGRAD=X*COSASQ+Y*SINASQ+XY*SIN2A
       SIGTAN=X+Y-SIGRAD
       RADSHR=XY*(COSASQ-SINASQ)+(Y X)*0.5*SIN2A
       THETA=ATAN(CRY/CRX)
       ALPHA=57.3*THETA
       PA=0.5*57.29578*ATAN(2.*XY/(Y-X))
       IF (2.*X-XMAX-XMIN) 405,420,420
  405  IF (PA) 410,420,415
  410  PA=PA+90.0
       GO TO 420
  415  PA=PA-90.0
  420  WRITE(6,125)NUME(N),X,Y,XY,XMAX,XMIN,PA,SIGRAD,SIGTAN,RADSHR,ALPHA
C
       IF (SUM-TOLER) 440,440,430
  430  IF (NCYCM-NCYCLE) 440,440,243
C
  440  GO TO 150
C
C      PRINT OF ERRORS IN INPUT DATA
C
  702  WRITE(6,712)LX
       GO TO 440
C
```

```
C      FORMAT STATEMENTS
C
    1 FORMAT(6I4,2E12.5,1I1)
    8 FORMAT(4I4)
    3 FORMAT(1I4,4F8.5,2F12.8)
    4 FORMAT(2I4,F12.8)
    5 FORMAT (3E15.8)
   99 FORMAT (1H1)
    2 FORMAT(4I4)
  140 FORMAT(4E15.8,F10.2)
  142 FORMAT(////110H  MATRIX     YOUNG'S MODULUS     DENSITY      POISSONS
     1 RATIO        EXPANSION COEFFICIENT        TEMPERATURE CHANGE)
  143 FORMAT(5X,2E20.8,E15.8,E20.8,12X,F20.10)
  144 FORMAT(////110H  FIBRE      YOUNG'S MODULUS     DENSITY      POISSONS
     1 RATIO        EXPANSION COEFFICIENT        TEMPERATURE CHANGE)
  125 FORMAT(1I5,10F12.3)
  126 FORMAT(120H1ELEMENT    X-STRESS     Y-STRESS       XY-STRESS    MAX-ST
     1RESS    MIN-STRESS  DIRECTION   RADIAL  TANGENTIAL  SHEAR     ALPHA)
  101 FORMAT(29H0NUMBER OF ELEMENTS           =,I4/)
  102 FORMAT(29H NUMBER OF NODAL POINTS       =,I4/)
  103 FORMAT(29H NUMBER OF BOUNDARY POINTS    =,I4/)
  104 FORMAT(29H CYCLE PRINT INTERVAL         =,I4/)
  105 FORMAT(29H OUTPUT INTERVAL OF RESULTS   =,I4/)
  106 FORMAT(29H CYCLE LIMIT                  =,I4/)
  107 FORMAT(29H TOLERANCE LIMIT              =,E12.4/)
  108 FORMAT(29H OVER RELAXATION FACTOR       =1F6.3)
  109 FORMAT (1I8,4F12.8,2F12.8)
  110 FORMAT(94H1EL.    I    J    K    YOUNGS MODULUS      DENSITY    POISSONS
     1   RATIO          ALPHA          DELTA T)
  111 FORMAT (80H1      NP        X-ORD        Y-ORD       X-LOAD       Y-LOA
     1D       X-DISP       Y DISP)
  112 FORMAT (20H BOUNDARY CONDITIONS)
  119 FORMAT(34H0          CYCLE      FORCE UNBALANCE)
  120 FORMAT(I11,2E20.6)
  121 FORMAT (42H0NODAL POINT X-DISPLACEMENT Y-DISPLACEMENT)
  122 FORMAT(I11,2E15.8)
  712 FORMAT (33H0OVER 8 N.P. ADJACENT TO N.P. NO.114)
  823 FORMAT(120H1  N-POINT              X-STRESS              Y-STRESS
     1       XY-STRESS           MAX STRESS     MIN-STRESS        DIRECTION)
C
      END
```

```
C      FORMAT STATEMENTS
C
     1 FORMAT(6I4,2E12.5,111)
     8 FORMAT(4I4)
     3 FORMAT(1I4,4F8.5,2F12.8)
     4 FORMAT(2I4,F12.8)
     5 FORMAT (3E15.8)
    99 FORMAT (1H1)
     2 FORMAT(4I4)
   140 FORMAT(4E15.8,F10.2)
   142 FORMAT(////110H  MATRIX     YOUNG'S MODULUS     DENSITY      POISSONS
     1 RATIO        EXPANSION COEFFICIENT        TEMPERATURE CHANGE)
   143 FORMAT(5X,2E20.8,E15.8,E20.8,12X,F20.10)
   144 FORMAT(////110H  FIBRE      YOUNG'S MODULUS     DENSITY      POISSONS
     1 RATIO        EXPANSION COEFFICIENT        TEMPERATURE CHANGE)
   125 FORMAT(115,10F12.3)
   126 FORMAT(120H1ELEMENT    X-STRESS     Y-STRESS       XY-STRESS    MAX-ST
     1RESS    MIN-STRESS  DIRECTION    RADIAL  TANGENTIAL  SHEAR     ALPHA)
   101 FORMAT(29H0NUMBER OF ELEMENTS           =,I4/)
   102 FORMAT(29H NUMBER OF NODAL POINTS       =,I4/)
   103 FORMAT(29H NUMBER OF BOUNDARY POINTS    =,I4/)
   104 FORMAT(29H CYCLE PRINT INTERVAL         =,I4/)
   105 FORMAT(29H OUTPUT INTERVAL OF RESULTS   =,I4/)
   106 FORMAT(29H CYCLE LIMIT                  =,I4/)
   107 FORMAT(29H TOLERANCE LIMIT              =,E12.4/)
   108 FORMAT(29H OVER RELAXATION FACTOR       =1F6.3)
   109 FORMAT (1I8,4F12.8,2F12.8)
   110 FORMAT(94H1EL.    I    J    K    YOUNGS MODULUS      DENSITY    POISSONS
     1   RATIO           ALPHA          DELTA T)
   111 FORMAT (80H1      NP         X-ORD        Y-ORD       X-LOAD       Y-LOA
     1D       X-DISP       Y DISP)
   112 FORMAT (20H BOUNDARY CONDITIONS)
   119 FORMAT(34H0          CYCLE      FORCE UNBALANCE)
   120 FORMAT(111,2E20.6)
   121 FORMAT (42H0NODAL POINT X-DISPLACEMENT Y-DISPLACEMENT)
   122 FORMAT(111,2E15.8)
   712 FORMAT (33H0OVER 8 N.P. ADJACENT TO N.P. NO.114)
   823 FORMAT(120H1  N-POINT              X-STRESS              Y-STRESS
     1       XY-STRESS           MAX STRESS     MIN-STRESS        DIRECTION)
C
      END
```